

GRAIN REFINEMENT IN DUAL PHASE STEELS

by

KRISHNENDU MUKHERJEE

B. Eng., Bengal Engineering College, Howrah, India, 2000
M. Tech., Indian Institute of Technology, Kanpur, India, 2002

A THESIS SUBMITTED IN PARTIAL FULFILLMENT OF
THE REQUIREMENTS FOR THE DEGREE OF

DOCTOR OF PHILOSOPHY

in

THE FACULTY OF GRADUATE STUDIES

(Materials Engineering)

THE UNIVERSITY OF BRITISH COLUMBIA

(Vancouver)

April 2009

© Krishnendu Mukherjee, 2009

Abstract

In this work, a potential production route of ultra fine grained dual phase (DP) steels was studied. Deformation induced ferrite transformation (DIFT) was applied in laboratory tests employing a Gleeble 3500 thermo-mechanical simulator to produce fine grained dual phase steels in two chemistries: a conventional DP 600 chemistry with 0.06 wt% C-1.9 wt% Mn-0.16 wt% Mo and the C-Mn base chemistry of 0.06 wt% C-1.8 wt% Mn with no Mo addition. This thermo-mechanical treatment consisted of cooling the steel from the austenitization temperature at a rate of 40°C/s to a deformation temperature, which was 25 to 50°C above the austenite to ferrite transformation start temperature (A_{r3}) specific for the given austenitization and cooling conditions. Then the steel was immediately deformed to a true strain of up to 0.7 followed by rapid quenching. The effects of prior austenite grain size, amount of strain and deformation temperature on DIFT microstructures were studied to identify the most suitable thermo-mechanical path to obtain an ultra fine grained dual phase structure. Microstructures were characterized by scanning electron microscopy (SEM) including electron back scatter diffraction (EBSD) mapping. For the investigated steels the highest amount of deformation with a true strain of 0.6 or above resulted in optimized microstructures consisting of 70-80% polygonal ferrite with a mean grain size of 1-2 μm . Simulation of DIFT hot rolling schedules were conducted with hot torsion tests to investigate the viability of the proposed approach. A two-dimensional phase field model was developed to describe the austenite to ferrite transformation during DIFT. Several nucleation schemes were examined in terms of time and position of forming ferrite nuclei in the austenite domain to replicate the

experimentally observed ferrite grain size spread. The austenite-ferrite interface mobility was used as the adjustable parameter to match the experimentally observed ferrite fraction.

Table of contents

Abstract.....	ii
Table of contents.....	iv
List of tables.....	viii
List of figures.....	x
List of symbols.....	xvi
Acknowledgements.....	xxi
1. Introduction.....	1
2. Literature review.....	5
2.1 The advantage of fine grained dual phase steel.....	5
2.2 Grain refining techniques.....	10
2.2.1 Asymmetric rolling.....	10
2.2.2 Deformation and annealing of martensite.....	11
2.2.3 Equal channel angular pressing (ECAP).....	12
2.2.4 Dynamic recrystallization of ferrite.....	13
2.2.5 Deformation induced ferrite transformation (DIFT).....	13
2.2.6 Advantages of Deformation Induced Ferrite Transformation.....	17
2.3 Processing parameters for DIFT.....	18
2.4 Mechanisms of DIFT.....	29
2.4.1 Ferrite nucleation sites in deformed austenite.....	29
2.4.2 Growth of DIFT ferrite.....	34
2.4.3 Dynamic recrystallization of austenite vs. DIFT.....	35
2.4.4 Effect of microalloying elements on DIFT.....	37

2.5 Modelling the austenite to ferrite transformation.....	38
2.5.1 Macroscopic length scale approach	39
2.5.2 Mesoscopic length scale approach.....	45
2.5.3 Summary	51
3. Objectives	54
4. Materials and experimental procedure	55
4.1 Steels investigated.....	55
4.2 Experimental equipment	57
4.3 Experimental methodology	58
4.3.1 Prior austenite grain sizes	58
4.3.2 Detection of A_{r3}	59
4.3.3 Static isothermal ferrite transformation tests	60
4.3.4 DIFT tests.....	60
4.4. Microstructural investigation for tests	65
4.5 Identification of microstructural constituents	67
4.6 Mechanical properties	69
4.7 Novelty of experimental studies	70
5. Results.....	71
5.1 Determination of d_{γ} and A_{r3}	71
5.2 Effect of different processing parameters on DIFT	76
5.2.1 Overview of DIFT tests performed	76
5.2.2 Effect of amount of strain on DIFT.....	78
5.2.3 Effect of prior austenite grain size on DIFT	82

5.2.4	Effect of deformation temperature on DIFT	84
5.3	Predominantly ultrafine ferrite microstructure.....	88
5.3.1	Conditions to obtain predominantly ultrafine ferrite microstructure	88
5.3.2	Grain size distribution	90
5.3.3	EBSD micrographs	91
5.3.4	Mechanical properties	96
5.4	Post deformation treatments.....	97
5.4.1	Role of post deformation cooling rate.....	97
5.4.2	Role of post deformation isothermal hold.....	98
5.5	Ferrite grain refinement by DIFT.....	99
5.6	Torsion simulation of DIFT	104
5.6.1	Replication of Gleeble tests	104
5.6.2	Effect of strain on DIFT.....	106
5.6.3	Effect of deformation temperature on DIFT	107
5.6.4	Simulation of DIFT for hot strip mill processing.....	108
5.7	Discussion	112
6.	Modelling of DIFT	120
6.1	Introduction.....	120
6.2	Model approach.....	121
6.2.1	Experimental condition selected for modelling	121
6.2.2	Domain selection.....	123
6.2.3	Growth model formulation and assumptions	127
6.2.4	Numerical details	135

6.3 Results.....	140
6.3.1 Determination of nominal mobility.....	140
6.3.2 Time and spatial distribution of ferrite nuclei.....	142
6.3.3 “Distributed nucleations” and adjusted mobilities.....	152
6.4 Discussion.....	155
7. Conclusions.....	160
Novelty of the work	162
Future work.....	162
References.....	164
Appendix 1.....	177
Appendix 2.....	178
Analysis of EBSD maps.....	178
Appendix 3.....	184
Estimation of ΔS	184
Appendix 4.....	187
Convergence analysis: Node size, time stepping, and interface thickness	187

List of tables

Table 2.1: Microstructural and tensile characteristics of dual phase steels [15]	9
Table 2.2: A_{r3} temperatures (cooling rate from reheating temperature is 2°C/s and austenite grain sizes are indicated in brackets) [38].....	23
Table 4.1: Chemical composition (in wt%) and A_{e3} temperature of the steels studied ...	55
Table 4.2: Chemical composition (in wt%) and A_{e3} temperature of the steels initially studied by Hazra.....	57
Table 4.3: Parameters describing the critical cooling rates for remaining austenite-to-martensite transformation after ferrite formation [96]	68
Table 5.1: Transformation data for Mo and Nb chemistries [9, 97].....	71
Table 5.2: Transformation data for Plain C chemistry	74
Table 5.3: DIFT test matrix for Mo steel	77
Table 5.4: DIFT test matrix for plain C steel (the reheating temperature is 950°C)	78
Table 5.5 Summary of effect of d_{γ} on DIFT for Mo steel	84
Table 5.6 Effect of deformation temperature on DIFT for Mo steel.....	86
Table 5.7: Test conditions where a predominantly ferrite microstructure has been obtained for Mo steel	89
Table 5.8: Test conditions where a predominantly ferrite microstructure has been obtained for plain C steel	89
Table 5.9: Test conditions where a predominantly ferrite microstructure has been obtained for Nb and Mo-Nb steels [97]	90
Table 5.10: Mean ferrite grain sizes obtained from EBSD and conventional SEM for optimized cases	95
Table 5.11: Summary of hardness measurements	96
Table 5.12: Summary of post-deformation isothermal holding tests	101
Table 5.13: Summary of static isothermal holding tests (holding time is 95% of transformation time).....	104

Table 5.14: Replication of Gleeble tests in torsion mode	105
Table 5.15: Summary of effect of strain on torsion replication of optimized (in terms of final microstructure) DIFT Gleeble tests, chemistry: plain C steel	106
Table 5.16: Simulated rolling schedule for DIFT	109
Table 5.17: Ferrite fraction and grain size after hot rolling simulation of DIFT	111
Table 6.1: Summary of physical parameters	134
Table 6.2: Ferrite fractions obtained from experiments and modelling	141
Table 6.3: Summary of results of “nominal nucleation” and “distributed nucleations” ($\mu_{\alpha\gamma}$ =nominal mobility)	150
Table 6.4: Summary of results of “distributed nucleations 1-5” with adjusted mobilities	152
Table 6.5: Results of adjusted mobility values with nucleation parameters	156

List of figures

Figure 2.1: Stress-strain curve showing the absence of work hardening in ultra fine ferrite steel [16].	7
Figure 2.2: Engineering stress-strain curves for coarse and ultrafine grained (CG and UFG, respectively) dual phase steels [15].	8
Figure 2.3: Schematic diagram of an Equal Channel Angular Pressing die [25].	12
Figure 2.4: Schematic diagram showing the procedure for Deformation Induced Ferrite Transformation (DIFT).	14
Figure 2.5: Schematic representation of the variation of the transformation start curve as a function of strain [36].	19
Figure 2.6: The critical amount of reduction $\epsilon_{C,UFF}$ with degree of undercooling (ΔT^*) for a low carbon steel (0.14C-1.5Mn-0.79Si, in wt%) [4].	20
Figure 2.7: Volume fraction of ferrite formed by DIFT as a function of strain for austenitization and deformation temperatures of 1200 and 775°C, respectively for a C-Mn-V steel [35].	21
Figure 2.8: The variation of ferrite volume fraction with degree of undercooling (ΔT^*) for different amounts of reduction in a low carbon steel (0.14C-1.5Mn-0.79Si, in wt%) [4].	25
Figure 2.9: The effect of post deformation isothermal holding time on ferrite fraction and grain size for a V-Nb microalloyed steel [39].	27
Figure 2.10: High angle grain boundaries ($>15^\circ$) in compressively deformed Ni-30% Fe alloy (deformation temperature 700°C, initial austenite grain size 20 μm), (inset for $\epsilon=2.1$ shows an optical micrograph) [45].	31
Figure 2.11: High angle misorientation boundary spacing in austenite for a Ni-30% Fe alloy and ferrite grain size for a low C steel, as a function of compressive strain in austenite [45-47], GDR: Geometric dynamic recrystallization.	32
Figure 2.12: Change of critical strain for DIFT (or dynamic recrystallization of austenite) with deformation temperature. Results of microstructural investigation are indicated as open marks (dynamic recrystallization of austenite), solid marks (DIFT), and half solid marks (DIFT after ferrite transformation start) [36].	36
Figure 4.1: Specimen geometry for DIFT tests.	61

Figure 4.2: The experimental procedure for DIFT tests	64
Figure 4.3: Specimen geometry for hollow tensile samples prepared from tested torsion specimen	69
Figure 5.1: Austenite microstructure after reheating to 1200°C, with a holding time of 2 min and water quenching for the plain C steel.....	73
Figure 5.2: Continuous cooling transformation behaviors for plain C steel austenitized at 950°C and 1200°C and then cooled with a cooling rate of 40°C/s.	73
Figure 5.3: Microstructure after continuous cooling test for plain C steel austenitized at 1200°C and cooled with a cooling rate of 40°C/s.....	74
Figure 5.4: Microstructure after continuous cooling test for plain C steel austenitized at 950°C and cooled with a cooling rate of 40°C/s.....	75
Figure 5.5: Effect of strain on DIFT for Mo steel, for initial austenite grain size $d_\gamma=20\ \mu\text{m}$, deformation temperature=700°C, (a) Strain=0.14, (b) Strain=0.33, (c) Strain=0.55, (d) Strain=0.63.....	80
Figure 5.6: Effect of strain on DIFT for plain C steel, for austenitization temperature=950°C, deformation temperature=675°C, (a) Strain=0.23, (b) Strain=0.47, (c) Strain=0.67.	81
Figure 5.7: Effect of prior austenite grain size on DIFT for Mo steel for $\Delta T=50^\circ\text{C}$ (a) Deformation temperature= $A_{r3}+\Delta T =670^\circ\text{C}+50^\circ\text{C}=720^\circ\text{C}$, Strain=0.61, initial austenite grain size $d_\gamma=13\ \mu\text{m}$, (b) Deformation temperature= $A_{r3}+\Delta T =655^\circ\text{C}+50^\circ\text{C}=705^\circ\text{C}$, Strain=0.63, initial austenite grain size $d_\gamma=20\ \mu\text{m}$, (c) Deformation temperature= $A_{r3}+\Delta T =650^\circ\text{C}+50^\circ\text{C}=700^\circ\text{C}$, Strain=0.6, initial austenite grain size $d_\gamma=27\ \mu\text{m}$	83
Figure 5.8: Effect of deformation temperature on DIFT for Mo steel, for initial austenite grain size $d_\gamma=13\ \mu\text{m}$ (a) Strain=0.67, deformation temperature= $670^\circ\text{C}+25^\circ\text{C}=695^\circ\text{C}$, (b) Strain=0.61, deformation temperature= $670^\circ\text{C}+50^\circ\text{C}=720^\circ\text{C}$	85
Figure 5.9: Effect of deformation temperature on DIFT for Mo steel, for initial austenite grain size $d_\gamma=20\ \mu\text{m}$ (a) Strain=0.57, deformation temperature= $655^\circ\text{C}+30^\circ\text{C}=685^\circ\text{C}$, (b) Strain=0.55, deformation temperature= $655^\circ\text{C}+45^\circ\text{C}=700^\circ\text{C}$	85
Figure 5.10: Effect of deformation temperature on DIFT for plain C steel, for austenitization temperature=950°C, (a) Strain=0.67, deformation temperature= $650^\circ\text{C}+25^\circ\text{C}=675^\circ\text{C}$, (b) Strain=0.64, deformation temperature= $650^\circ\text{C}+50^\circ\text{C}=700^\circ\text{C}$	87

Figure 5.11: Grain size distribution for Mo steel as measured ($d_{\gamma}=13 \mu\text{m}$, $T_{def}=695^{\circ}\text{C}$, $\epsilon=0.65$) and as-fitted log-normal distribution (solid line).....	91
Figure 5.12: EBSD maps for optimized conditions for all steels (a) Mo steel, (b) Nb steel, (c) Plain C steel, (d) Mo-Nb steel.....	94
Figure 5.13: Distribution of grain boundary misorientation angle for all four chemistries for optimized conditions.	95
Figure 5.14: DIFT microstructure obtained for the Mo steel after reheating at 950°C , deforming 25°C above A_{r3} and subsequently water quenching.....	97
Figure 5.15: Micrograph resulting from DIFT test employing a strain of 0.72 and post deformation isothermal holding of 5 s at 675°C for the plain C steel reheated at 950°C	98
Figure 5.16: Fraction transformed-time graph for Mo steel (isothermally held at 695°C)	100
Figure 5.17: Micrograph after DIFT test with $d_{\gamma}=13 \mu\text{m}$ employing a strain of 0.78 and post deformation isothermal holding of 6 min 8 s at 695°C for the Mo steel.....	101
Figure 5.18: Micrograph after DIFT test employing a strain of 0.74 and post deformation isothermal holding of 3 min 17 s at 675°C for the plain C steel reheated at 950°C	102
Figure 5.19: Microstructure after isothermal holding at 695°C for 6 min 8 s and subsequent He quenching for Mo steel with austenite grain size of $13 \mu\text{m}$	103
Figure 5.20: Microstructure after isothermal holding at 675°C for 3 min 17 s and subsequent He quenching for plain C steel with austenitization temperature of 950°C	103
Figure 5.21: Microstructure obtained from torsion replication of the optimized (in terms of final microstructure) Gleeble DIFT test, deformation temperature 675°C , (a) strain=0.6, (b) strain=1.5, (c) strain=3.0.....	107
Figure 5.22: Microstructure obtained from torsion replication of Gleeble DIFT test, deformation temperature 700°C , strain=1.5.....	108
Figure 5.23: Stress-strain curve of DIFT passes during hot strip rolling simulation of plain C steel.....	110
Figure 5.24: Simulated hot strip rolling microstructure of plain C steel with final DIFT pass at (a) 675°C , (b) 650°C	110
Figure 5.25: Tensile curve for simulated hot strip rolling microstructure of plain C steel with final DIFT pass at 650°C	111

Figure 5.26: Volumetric grain size distribution of ferrite grains for plain C steel after DIFT with different strains.	113
Figure 5.27: Effect of strain on microstructure for Nb steel reheated at 950°C and deformed at $\Delta T = 25^\circ\text{C}$: (a) Strain =0.2, (b) Strain =0.4, (c) Strain =0.6 [97].	114
Figure 5.28: Effect of strain on microstructure for Mo steel reheated at 1050°C and deformed at $\Delta T = 30^\circ\text{C}$: (a) Strain = 0.15, (b) Strain = 0.35, (c) Strain = 0.55.....	115
Figure 5.29: Effect of strain on microstructure for Mo-Nb steel reheated at 950°C and deformed at $\Delta T = 25^\circ\text{C}$: (a) Strain =0.2, (b) Strain =0.6 [97].	116
Figure 6.1: Temperature vs. transformation time for Mo steel He and water quenched after DIFT.	123
Figure 6.2: Shape and size change of austenite grain by reduction p . [106].....	124
Figure 6.3: Schematic diagram of the selection of representation domain and actual calculation domain for modeling.	126
Figure 6.4: Three types of interfaces.....	130
Figure 6.5: Paraequilibrium phase diagram for the Mo steel as calculated by THERMOCALC.....	132
Figure 6.6: An example of selection of actual calculation domain.....	135
Figure 6.7: Boundary conditions and ghost nodes.	136
Figure 6.8: Introduction of ferrite nuclei in austenite matrix.....	138
Figure 6.9: Phase field parameters ϕ_1 , and ϕ_4 at the line AA (as shown in Figure 6.8) at two times.	138
Figure 6.10: Ferrite fraction vs. transformation time for He and water quenched samples after DIFT, obtained from phase field simulations (nominal nucleation).....	141
Figure 6.11: Nominal ferrite grain from “nominal nucleation” with $\mu_{\alpha\gamma} =$ nominal mobility and He quenching.....	142
Figure 6.12: Simulated microstructure for “distributed nucleation 1” ($\mu_{\alpha\gamma}$ =nominal mobility).....	143
Figure 6.13: Simulated microstructure for “distributed nucleation 2” ($\mu_{\alpha\gamma}$ =nominal mobility).....	145

Figure 6.14: Simulated microstructure for “distributed nucleation 3” ($\mu_{\alpha\gamma}$ =nominal mobility, the arrows indicate the maximum area of austenite that has no ferrite nucleus).	147
Figure 6.15: Simulated microstructure for “distributed nucleation 4” ($\mu_{\alpha\gamma}$ =nominal mobility).	148
Figure 6.16: Simulated microstructure for “distributed nucleation 5” ($\mu_{\alpha\gamma}$ =nominal mobility).	149
Figure 6.17: Simulated microstructure for “distributed nucleation 4” ($\mu_{\alpha\gamma}$ =5×nominal mobility).	154
Figure 6.18: Simulated microstructure for “distributed nucleation 3” at 0.55 s, $\mu_{\alpha\gamma}$ =3.5×nominal mobility.	158
Figure 6.19: Carbon profile along the line shown in Figure 6.18	159
Figure A1.1: Schematic CCT diagram for low/medium carbon steel.	177
Figure A2.1: Original EBSD map for Mo steel.	178
Figure A2.2: Map obtained after cleaning of map shown in Figure A1.1	179
Figure A2.3: Object determined based on critical misorientation of 2° for map shown in Figure A2.2	179
Figure A2.4: Band contrast distribution with $BC_{critical}$ for the EBSD map of Mo steel.	180
Figure A2.5: Mean band contrast map for the Mo steel.	181
Figure A2.6: Grain size distribution obtained from the EBSD map for Mo steel (critical misorientation angle is 2° and $BC_{critical}$ is 85) and as-fitted log-normal distribution with similar width and ignoring the noise.	182
Figure A2.7: Adjusted grain size distribution and re-fitted log-normal distribution by ignoring the noise.	183
Figure A3.1: <i>Driving pressure</i> vs. C_γ for Mo steel at 968 K.	184
Figure A3.2: Driving pressure vs. ΔT^*	186
Figure A4.1: Ferrite transformation kinetics for two node sizes at 968K (nominal nucleation).	189

Figure A4.2: Ferrite transformation kinetics for two node sizes at cooling path from 968 K to 873 K (nominal nucleation). 190

Figure A4.3: Ferrite transformation kinetics for three time steppings (nominal nucleation)..... 191

Figure A4.4: Ferrite transformation kinetics for two interfacial thickness (nominal nucleation)..... 192

List of symbols

a : node size

a^* : Parameter for calculating critical cooling rate to obtain martensite

A_s : The maximum serration amplitude of the austenite grain boundary

b : JMAK equation parameter

b_I : Modified JMAK equation parameter

b^* : Parameter for calculating critical cooling rate to obtain martensite

\vec{b} : Burgers vector

BC_{critical} : Critical mean band contrast for EBSD map

Ae_3 : Equilibrium austenite to ferrite transformation temperature

Ar_3 : Austenite to ferrite transformation temperature for continuous cooling

C : Carbon concentration

C_0 : Average carbon concentration of steel

C_α : Carbon concentration in ferrite

C_α^{eq} : Equilibrium carbon concentration in ferrite

C_γ : Carbon concentration in austenite

C_γ^{eq} : Equilibrium carbon concentration in austenite

$d_a(T)$: The extrapolated dilation from the austenite region

$d_m(T)$: Measured dilation

$d_p(T)$: The extrapolated dilation from the product region

d_α : Ferrite grain size

d_γ : Initial austenite grain size

D_S : Solute diffusivity

$D(x,y)$: Distance of the point (x,y) from the centre of the ferrite nucleus

D_α^C : Diffusivity of carbon in ferrite

D_γ^C : Diffusivity of carbon in austenite

E_{def} : Stored energy in deformed austenite

f_α : Ferrite fraction

f_v : Volumetric grain size distribution of ferrite grains

$f(x)$: Frequency of ferrite grains with diameter x

$f_{ij}^{bulk\ energy}$: Bulk energy of two grains i, j in multi phase field formulation

$f_{ij}^{gradient\ energy}$: Gradient energy between two grains i, j in multi phase field formulation

$f_{ij}^{interfacial\ energy}$: Interfacial energy between two grains i, j in multi phase field formulation

F : The total free energy of the system

ΔG : Gibbs free energy change during phase transformation

ΔG_V : Gibbs free energy difference between the austenite and the ferrite phases (per unit volume)

ΔG_{ij} : Gibbs free energy difference between two grains i, j that provides driving pressure for phase transformation

ΔG_{SD} : Energy dissipated by solute drag

H_V : Vicker's hardness number in kg/mm^2

ΔH : Change in enthalpy

I_a : Constant for determining the extrapolated dilation from the austenite region

I_p : Constant for determining the extrapolated dilation from the product region

I_s : Ferrite nucleation rate

k : Partition co-efficient of carbon between ferrite and austenite

k^* : Boltzmann constant

k_1 : Workhardening parameter in Kocks-Mecking equation

k_2 : Recovery-softening parameter in Kocks-Mecking equation

K_1 : A constant related to the nucleation site density to determine ferrite nucleation rate

K_2 : A constant related to the ferrite-austenite interface energy to determine ferrite nucleation rate

K_{H-p} : Hall-Petch constant

m : Modified JMAK equation parameter

n : JMAK equation parameter

p : Amount of reduction

Q : Activation energy of the mobility of the ferrite-austenite interface

R : Radius of ferrite nucleus in phase field model

R_f : Radius of ferrite grain

S_a : Thermal expansion coefficient for austenite

S_p : Thermal expansion coefficient for product phase

ΔS : Proportionality factor to determine driving pressure from undercooling/
transformation entropy

Δt : Time step for phase field model and carbon diffusion model

T : Absolute temperature

T_{eq} : Equilibrium temperature

T_{γ} : Austenitization (or reheating) temperature

$T_{\alpha}^{eq}(C_{\alpha})$: $\alpha/\alpha+\gamma$ phase boundary temperature when carbon concentration is C_{α}

$T_{\gamma}^{eq}(C_{\gamma})$: $\gamma/\alpha+\gamma$ phase boundary temperature when carbon concentration is C_{γ}

ΔT : Superheat above A_{r3}

ΔT^* : Undercooling below A_{e3}

ΔT_{α}^* : Undercooling below $T_{\alpha}^{eq}(C_{\alpha})$

ΔT_{γ}^* : Undercooling below $T_{\gamma}^{eq}(C_{\gamma})$

v : Ferrite-austenite interface velocity

W : Probability of transition in Monte Carlo method

x_p : Median ferrite grain size for log-normal distribution

X : Fraction transformed

α : Constant to determine E_{def}

ε : Strain

$\varepsilon_{C, DIFT}$: Critical strain to initiate DIFT

$\varepsilon_{C, UFF}$: Critical strain to obtain a predominantly ultra fine ferrite microstructure

ε_{VM} : Von Mises equivalent strain

ϕ_i : Phase field parameter

ϕ_C : Critical cooling rate to obtain martensite

η : Interface width

η_{ij} : Interface width between two grains i, j in multi phase field formulation

μ : Interface mobility

μ_{ij} : Interface mobility between two grains i, j

$\mu_{\alpha\alpha}$: Ferrite-ferrite interface mobility

$\mu_{\alpha\gamma}^0$: Pre-exponential factor for ferrite-austenite interface mobility

$\mu_{\alpha\gamma}$: Ferrite-austenite interface mobility

μ^* : Shear modulus

ρ : Dislocation density

σ : Standard deviation of log-normal ferrite grain size distribution

σ_i : Interfacial energy

σ_0 : Lattice friction stress

σ_{ij} : Interfacial energy between two grains i, j

$\sigma_{Y.S.}$: Yield strength

$\sigma_{T.S.}$: Tensile strength

$\sigma_{\alpha\alpha}$: Ferrite-ferrite interfacial energy

$\sigma_{\alpha\gamma}$: Austenite-ferrite interfacial energy

$\sigma_{0.08}$: Flow stress at 8% strain

Acknowledgements

I would like to express sincere gratitude to my supervisor, Prof. Matthias Militzer for his keen insight, wise guidance and encouragement throughout the course of this work. I wish to thank Prof. W. J. Poole and Dr. C. W. Sinclair, respectively, for making me conversant with the Thermomechanical Laboratory and the EBSD technique.

I am grateful to the Department of Materials Engineering, at UBC for providing an excellent research environment. I want to specially thank the people of Stores (Mr. Glenn Smith), Machine Shop (Mr. Ross McLeod, Mr. Carl Ng, and Mr. David Torok), Gleeble Laboratory (Mr. Steven Lechuk, Dr. James Huang, and Dr. Dongsheng Liu), Electron Microscopy Lab (Mrs. Mary Fletcher), and the “Microstructure Engineering” group (Dr. Fateh Fazeli, Mr. Plamen Petkov, Mr. Sujoy Hazra, Mr. Jerome Cordonier, Mr. Morten Ro Helsem, Mr. Hamid Azizi-Alizamini, Mr. Sephr Gerami, Dr. Sujay Sarkar, Dr. Kumkum Banerjee, Mr. Morteza Toloui, and Mr. Sina Shahandeh).

The financial support received from the National Centre of Excellence (NCE) AUTO21 and the Natural Sciences and Engineering Research Council of Canada is acknowledged with gratitude. The Mo steel has been supplied by Stelco Inc. and the laboratory steels by CANMET. I wish to thank Prof. Peter Hodgson and Mr. Andrew Sullivan from Deakin University for carrying out the EBSD mappings.

I also want to acknowledge the support of my family members and friends during the course of my research. In particular I want to thank my wife whose inspiration and help is highly appreciated. I specially acknowledge my parents for their constant encouragement.

1. Introduction

The major applications of steel are in automotive parts, household appliances, reinforcement in civil construction, and in oil and gas pipelines. The reason for this wide range of applications is that steel is an abundant and cost efficient material and the fabrication of steel products can be manipulated to obtain a wide range of mechanical properties. This versatility of steel is inherently linked to the solid-solid phase transformation of iron from the high-temperature FCC structure to the low-temperature BCC structure. Tailoring processing conditions and steel chemistries permits to exploit this phase transformation to produce a multiplicity of microstructures that lead to a variety of properties. For example, important high-strength steel classes include High Strength Low Alloy (HSLA), Dual Phase (DP), and Transformation Induced Plasticity (TRIP) steels.

Solid state transformation in steel can be divided into two groups: (i) diffusional transformations, and (ii) displacive transformations. The different phases and/or transformation products involved in these transformations are: austenite, ferrite, pearlite, bainite and martensite. Austenite is the phase that is stable at higher temperatures and it has a FCC crystal structure. In a number of steels (e.g. TRIP steels) some austenite may be retained in the final microstructure. Ferrite is an equilibrium phase with a BCC crystal structure. Pearlite is a lamellar structure consisting of ferrite and cementite (Fe_3C). Cementite (Fe_3C) is a stoichiometric phase with an orthorhombic crystal structure. The formation of ferrite and pearlite from austenite is a diffusional transformation. Bainite

can be considered as degenerated pearlite, i.e. a highly defective mixture of BCC ferrite and carbides. However, in some steels (e.g. TRIP steels) a carbide-free bainite may form. Further, there is a long standing debate regarding the nature of the bainite transformation, i.e. whether or not it is a diffusional or a displacive transformation. Martensite is a non-equilibrium phase with a BCT crystal structure. Martensite forms by a displacive mechanism.

To summarize this complexity of the phase transformation into a useful tool for the user in the steel industry, the austenite decomposition in a particular steel during continuous cooling is represented by Continuous Cooling Transformation (CCT) diagrams. A typical CCT diagram is shown in **Figure A1.1**. This diagram indicates that increasing the cooling rate decreases transformation temperatures thereby gradual shifting the transformation products from ferrite/pearlite to bainite and finally martensite.

The most important and most demanding application of steel is in the automotive industry. Here, steels are desired that combine high strength with excellent formability. Through enhancing the strength of steel a weight reduction in the vehicles can be achieved via gauge reduction. Ferrite grain refinement in steel can improve the yield strength to a large extent. If the ferrite grain size is approximately 1 μm , it is called ultrafine ferrite (UFF). Recently ferrite grain refinement has been investigated worldwide, especially in Australia, Europe, Japan (Super metal project), Korea (HIPERS 21-Development of high performance structural steels for 21st century), and China with an emphasis on plain carbon steels for structural applications. Among different routes

studied deformation induced ferrite transformation (DIFT) and asymmetric rolling are most suitable for sheet production [1-5]. However, grain refinement deteriorates the ductility and a major problem with ultra fine grained ferritic steels is the absence of significant work hardening after yielding [3].

A combination of high strength, excellent elongation and superior crashworthiness is achieved by dual phase and multi phase steels. Typically, the dual phase microstructure consists of martensite that is dispersed as second phase in a ferrite matrix. This microstructure leads to a number of advantageous mechanical properties that makes these steels suitable for autobody applications: high tensile strength, low Y.S. (Yield Strength)/UTS (Ultimate Tensile Strength) ratio, high initial work hardening rate, high uniform elongation, and no yield point elongation. A recent study proposed an ultra light steel auto body (ULSAB) for new vehicle designs that contain as much as 74% of dual phase steel [6]. The use of dual phase steels in state-of-the-art vehicle designs is currently approaching 10% by weight and is projected to increase to 30% by 2015.

The concept of ultra fine grained dual phase steel was introduced to combine the strengthening effect of the ultrafine ferritic structure with the superior formability of the dual phase steels [7]. Moreover, the enhanced workhardening of the dual phase structure would introduce attractive ultimate tensile strength values.

In this research a potential processing route for producing ultra fine ferrite dual phase steel was studied. Ferrite grain refinement was achieved by deformation induced ferrite transformation (DIFT). The effects of different processing parameters (austenitization

temperature, deformation temperature, strain) on DIFT were studied for two steel chemistries. This work dealt with experimental studies on the formation of ultra fine grain dual phase microstructures in a steel with a commercial Mo DP 600 chemistry and a plain C steel having the same base chemistry as the former. Based on the experimental results a microstructure model of DIFT was proposed using the phase field approach. This study was carried out under the auspices of the National Centre of Excellence (NCE) AUTO 21 programme. The main goal of AUTO 21 is to develop a new generation car for the 21st century. Another researcher of this project (Sujoy Hazra) did similar experiments in parallel, on forming ultra fine grained dual phase microstructures in two other steels with the same base chemistry as the DP 600 steel but with varying Mo and/or Nb contents. The present work completed this previous study by characterizing the final microstructures obtained in these steels by advanced techniques.

2. Literature review

2.1 The advantage of fine grained dual phase steel

One of the ways to improve the mechanical properties of steel is to refine the ferrite grain size. Currently, ferrite grain refinement is achieved through controlled rolling and subsequent accelerated cooling [8]. The technique of controlled rolling of steel is called Thermomechanical Controlled Processing (TMCP) of steel. Hickson et al. reported that for a plain carbon steel composition in plate rolling, TMCP and subsequent water cooling can produce a ferrite grain size of 5 μm , whereas the ferrite grain size obtained through conventional hot rolling and air-cooling was 10 μm [8]. The Hall-Petch relation can be used to estimate the increase in the yield strength with the decrease in ferrite grain size, i.e.

$$\sigma_{Y.S.} = \sigma_0 + K_{H-P} d_{\alpha}^{-\frac{1}{2}} \quad (2.1)$$

where, $\sigma_{Y.S.}$ is the yield strength, σ_0 is the “friction stress” that represents the overall resistance of the crystal lattice to dislocation movement, K_{H-P} is the Hall-Petch constant, and d_{α} is the ferrite grain size. Hickson et al. estimated an increase of 80 MPa in the yield strength, when the ferrite grain size was reduced from 10 μm to 5 μm [8].

The TMCP of steel involves rolling austenite below the recrystallization temperature. This pancakes the austenite and increases the effective austenite grain boundary area. Considering the fact that ferrite nucleation takes place at the austenite grain boundary, the

TMCP of steel increases the ferrite nuclei density as compared to conventional hot rolling. This is because, in the conventional hot rolling of steel, ferrite transformation occurs from undeformed austenite. A number of studies were performed [9-14] that showed the strong effect of deformation on the austenite to ferrite transformation and provided clear evidence that retained strain in austenite contributes to ferrite grain refinement. However, the limit of ferrite grain refinement by TMCP of plain carbon steel is limited to 5 μm [8].

Using the Hall-Petch relation, Hickson et al. estimated an increase of 350 MPa in the yield strength of steel, if the ferrite grain size could be reduced from 5 μm to 1 μm [8]. However, ferritic steel with a grain size of 1 μm lacks strain hardening after yielding [15]. Hodgson et al. compared the tensile behavior of ultrafine ferritic steel with a conventional steel [16] (**Figure 2.1**). From **Figure 2.1** it is observed that the strength of the ultrafine ferritic steel is very close to its yield strength as there is very little work hardening after yielding.

Although ultrafine ferrite steel has increased yield strength, it is unsuitable for automotive application due to the absence of strain hardening. In this regard, the properties of coarse-grained dual phase steels were revisited by Son et al. [15]. Dual phase steels exhibit continuous yielding, low yield strength, high tensile strength, moderately high uniform elongation, and rapid strain hardening at the initial plastic deformation stage [17]. The rapid increase in work hardening at low plastic strain for dual phase steels results from the increased density of “geometrically necessary

dislocations” in the ferrite. These dislocations are created by the need to maintain compatibility between the two plastically incompatible phases during plastic deformation [18]. Based on these promising properties of dual phase steels for automotive application, Son et al. proposed the concept of ultra fine grained dual phase steel [15].

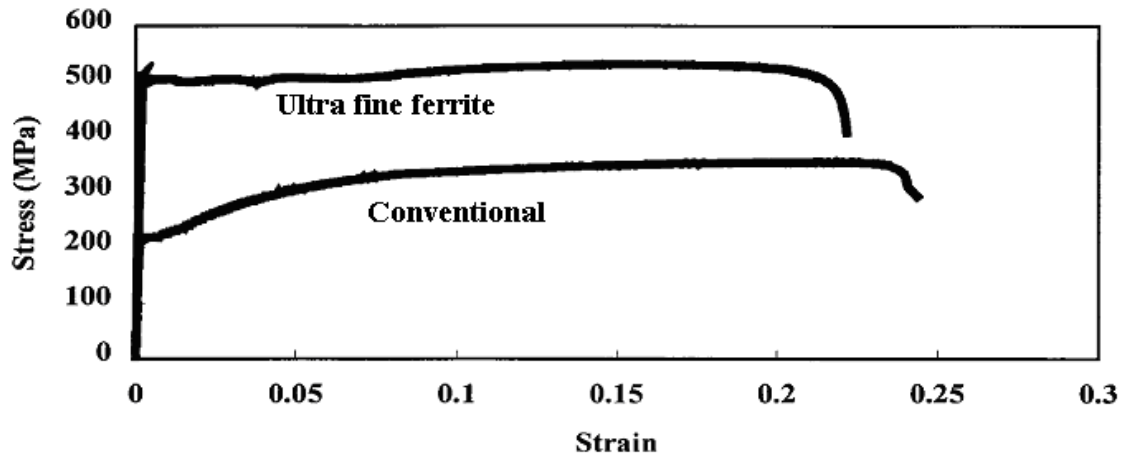


Figure 2.1: Stress-strain curve showing the absence of work hardening in ultra fine ferrite steel [16].

Son et al. quantified the effect of ferrite grain refinement on mechanical properties of dual phase steels [15]. They produced ultra fine grained dual phase steel through equal channel angular pressing (ECAP) and subsequent annealing, as described in detail in section 2.2.3. Figure 2.2 shows the engineering stress-strain curves of the three ultra fine grained dual phase steels and a coarse grained dual phase steel. All steels have the same base chemistry of 0.15 wt% C, 0.25 wt% Si and 1 wt % Mn. However the V content varies for each of them as indicated in Figure 2.2. It is observed that the ultra fine grained dual phase steels have in general higher tensile strength than the coarse grained

dual phase steels. Continuous yielding is also present in ultra fine grained dual phase steel as in coarse grained dual phase steel. The microstructural details and mechanical properties for these steels are given in **Table 2.1**. From **Table 2.1** it can be concluded that the size of the martensite islands is also refined in conjunction with ferrite grain refinement. Addition of V increases the fraction of martensite. This increased martensite fraction raise the tensile strengths for the V containing steels. The uniform and total elongations are not affected by this refinement in ferrite grain size.

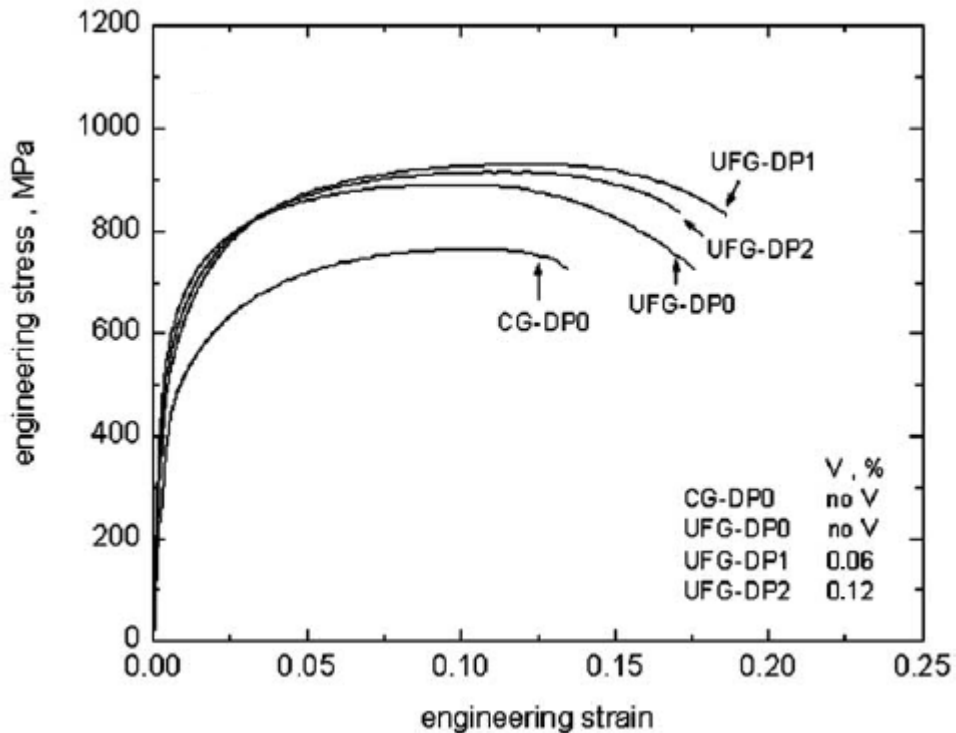


Figure 2.2: Engineering stress-strain curves for coarse and ultrafine grained (CG and UFG, respectively) dual phase steels [15].

Table 2.1: Microstructural and tensile characteristics of dual phase steels [15]

Identification	Martensite fraction	Martensite island size, μm	d_{α} , μm	$\sigma_{y.s.}$, MPa	$\sigma_{T.S.}$, MPa	True uniform elongation (%)	Total engineering elongation to fracture (%)
CG-DP0	0.22	9.8	19.4	510	843	9.8	13.5
UFG-DP0	0.28	0.8	0.8	581	978	9.3	17.6
UFG-DP1	0.35	1.1	0.9	540	1044	11.5	18.1
UFG-DP2	0.32	1.1	1.2	565	1015	10.4	16.6

Dual phase steels are either produced through hot rolling or through intercritical annealing of cold rolled material. Cold rolled dual phase steels are either quenched to room temperature after intercritical annealing in the austenite-ferrite region (continuous annealing line) or quenching is interrupted to galvanize the sheet (hot dip galvanizing line). Industrial constraints (e.g. insufficient cooling rates at line or holding at the temperature of the zinc bath, which is approximately 460°C in hot dip galvanizing lines) require addition of alloying elements (e.g. Mo) to avoid or minimize austenite transformation to ferrite and/or bainite during holding and/or cooling. In the case of hot rolled dual phase steels, the cooling path on the run out table of a hot strip mill is controlled in such a fashion that the austenite to ferrite transformation is terminated at the desired 80-90% level. Subsequently, a faster cooling rate is employed such that the

remaining austenite is transformed to martensite instead of pearlite or bainite. As simple C-Mn chemistries require a coiling temperature below 150°C to obtain the desired martensite formation, alloying elements (e.g. Si, Cr) can be added to get the same level of martensite at higher coiling temperatures [19].

2.2 Grain refining techniques

There are several methods of grain refinement, which can be employed to produce ultra fine ferritic steel: (1) asymmetric rolling, (2) deformation and annealing of martensite, (3) equal channel angular pressing, (4) dynamic recrystallization of ferrite, and (5) deformation induced ferrite transformation (DIFT). Among them deformation induced ferrite transformation was selected and modified in the present study to produce ultra fine grained dual phase steel. A brief description of all the methods to produce ultra fine ferritic steels will be given subsequently. Based on that, the advantage of deformation induced ferrite transformation will be discussed, in terms of its applicability to produce ultra fine grained dual phase steel.

2.2.1 Asymmetric rolling

Asymmetric rolling can be performed in two ways: (i) using two rolls of the same diameter but different velocities, (ii) using two rolls of different diameters. Both methods introduce severe plastic deformation in the rolled material by simultaneous action of two modes: compression and additional shear deformation [20]. Morimoto et al. reported the

industrial production of fine grained steel at Nakayama Steel, Japan, with grain sizes of 2-5 μm , in a 2 mm thick plain C steel strip by applying asymmetric hot rolling [21].

2.2.2 Deformation and annealing of martensite

Deformation and annealing of a plain low-carbon steel sheet with a martensitic microstructure can be used to produce an ultra-fine ferritic microstructure [22, 23]. Ueji et al. studied the effect of deformation and annealing temperature on ferrite grain refinement by this process [24]. Using rolling reductions of 25%, 50% and 70% (von Mises' equivalent strain of 0.5, 0.8 and 1.3, respectively), they found that 50% rolling reduction gives the optimum fine grained structure and mechanical properties (annealing temperature: 500°C, annealing time: 0.5 hour). In another set of experiments, Ueji et al. studied the effect of annealing temperature on final microstructure [22]. For this purpose, they annealed the cold rolled samples at various temperatures ranging from 200 to 700°C (rolling reduction: 50%, and annealing time: 0.5 hour). For annealing temperatures of 450-500°C the final microstructure was composed of ultrafine equiaxed ferrite grains (mean grain size of 180 nm) produced by recrystallization of martensite [22]. The main advantage of this process is that it does not need intense straining and hence it will be comparatively easy to adapt for practical use without any new metal working facilities.

2.2.3 Equal channel angular pressing (ECAP)

In Equal Channel Angular Pressing (ECAP) a material is subjected to intense plastic straining in a specifically designed die. The schematic diagram of ECAP die is shown in **Figure 2.3**. The strain per pass depends on the inner contact angle (ϕ) and the arc of curvature (ψ) at the outer point of contact between the channels of the die. Ultrafine grains with an average diameter of $0.3\mu\text{m}$ were obtained in a plain low-carbon steel by imposing a severe plastic strain close to 8 by this method at 350°C [25].

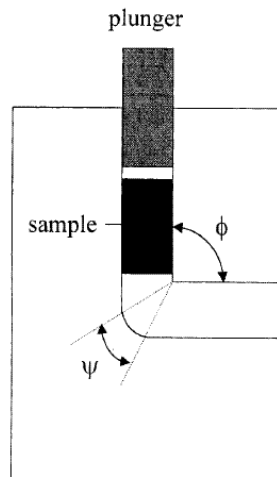


Figure 2.3: Schematic diagram of an Equal Channel Angular Pressing die [25].

Hwang et al. studied the mechanical properties of a ultra fine grained steel produced through ECAP. They reported a tensile strength of 943 MPa and a total elongation of 11% for a ultra fine grained ferrite-pearlite steel with a ferrite grain size of $0.5\mu\text{m}$ [26]. Son et al. produced ultra fine grained dual phase steel through ECAP and subsequent annealing [15]. During ECAP they applied an effective strain of 4 at 500°C .

Subsequently, they intercritically annealed the sample at 730°C for 10 min. The microstructural details of the steels produced are summarized in **Table 2.1**. Ultra fine grained ferrite with a grain size of 1 μm along with martensite islands of similar size were obtained by this technique. However, one of the major drawbacks of this technique is that it is not capable of producing flat products.

2.2.4 Dynamic recrystallization of ferrite

The deformation of steel in the ferrite region was studied as a possible path of ferrite grain refinement. However, the mechanism that introduces ferrite grain refinement during warm rolling of steel (i.e., rolling in the ferrite region) can vary for different steel chemistries and deformation conditions. Najafi-Zadeh et al. reported ferrite grain refinement in Interstitial Free steels by warm rolling [27]. They concluded that dynamic recrystallization was responsible for decreasing the ferrite grain size to 1-3 μm .

2.2.5 Deformation induced ferrite transformation (DIFT)

When a metal is mechanically deformed, most of the energy is dissipated as heat. Approximately, 1% of the applied energy is stored in the metal as defects (mainly dislocations). But when the metal is deformed at high temperature (hot deformation, deformation temperature > 0.6 of melting temperature) this stored energy is also dissipated during deformation by recovery, recrystallisation or phase transformation.

To achieve DIFT, the steel is deformed when heavily undercooled and metastable austenite is present (**Figure 2.4**). Usually the steel is deformed 25 to 100°C above the A_{r3} temperature; i.e. the transformation start temperature for the same cooling path, but without the deformation step. This superheat above the A_{r3} temperature is referred as ΔT in this study.

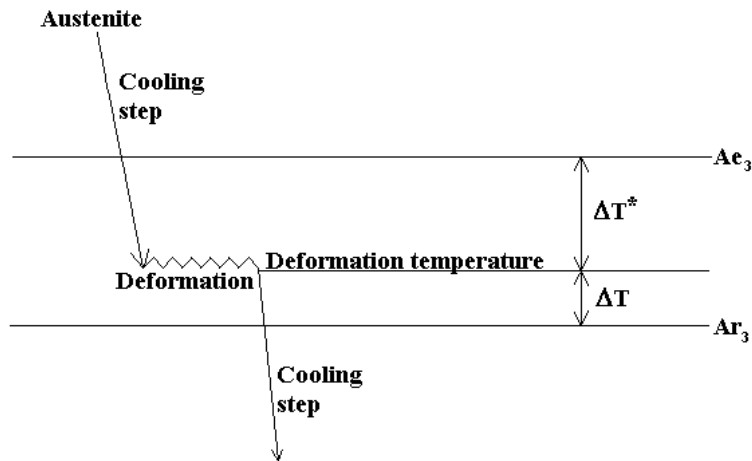


Figure 2.4: Schematic diagram showing the procedure for Deformation Induced Ferrite Transformation (DIFT)

The undercooling ΔT^* below the A_{e3} temperature provides sufficiently high driving pressure for ferrite nucleation. Austenite to ferrite transformation is favourable over recrystallization of austenite at this high undercooling (ΔT^*). Deformation at this temperature enhances ferrite nucleation resulting in finer ferrite grains. There are other names for DIFT used in the literature: Strain induced ferrite transformation (SIFT), Strain induced transformation (SIT), Strain induced dynamic transformation (SIDT), Dynamic

ferrite transformation (DFT). It is assumed that in DIFT, the austenite to ferrite transformation starts during the deformation [28]. The austenite to ferrite transformation during the deformation is called dynamic transformation.

Yada et al. [29] achieved a ferrite grain size of 2-3 μm in a C-Mn steel through deformation in the temperature range of $A_{r3}+50^\circ\text{C}$ to $A_{r3}+100^\circ\text{C}$. They applied reductions of more than 50% in less than 1 s. Niikura et al. achieved a ferrite grain size of 1.8 μm by applying DIFT in a 0.1 wt%C-1.3 wt%Mn-0.005 wt%Nb steel [1]. To achieve DIFT they deformed the steel with a strain of 1.5, at 700°C (d_γ or T_γ is not mentioned in the paper). Whereas, Huang et al. applied the same technique but reported a somewhat higher final ferrite grain size of 3-5 μm [2]. Nevertheless, the studies of Niikura et al. and Huang et al. implemented the idea of deforming undercooled austenite. But a systematic investigation to quantify the role of deformation temperature was not provided in their studies. Applying DIFT, several other groups produced 1 μm equiaxed ferrite grains in low C steel by laboratory rolling of thin strip [8, 30, 3]. But the ultrafine ferrite layer was present at the surface of the strip only.

Hurley et al. proposed that ferrite nucleates within substructures formed in the work hardened austenite grains [30]. Once ferrite is formed it will also be deformed and may dissipate stored energy by dynamic recrystallization. Some researchers suggested that dynamic recrystallization of ferrite might played a role in ferrite grain refinement [4, 31-33]. However, this was not quantified in detail in the literature. Hodgson et al. described that dynamically formed ferrite will undergo further deformation [32]. If dynamic

recrystallization of ferrite was not occurring then the dynamically formed ferrites would have been elongated in shape [32]. But, in their study Hodgson et al. did not find any change in the aspect ratio of the ferrite grains in the final microstructure, with increasing deformation (the aspect ratio of the ferrite grains was approximately 1.5). From this observation they concluded that dynamic recrystallization of ferrite occurred in parallel to DIFT [32]. By TEM observations, Hong et al. confirmed the presence of recrystallized ferrite grains in the final microstructure [4].

As a high amount of deformation is required for DIFT to take place and most of the existing hot strip mills do not have the capacity to provide such high strains in a single pass, new processing methods need to be found to implement this technique commercially. Hot rolling of thin strip produces high undercooling and high shear strain at the surface and thus the region of ultra fine ferrite is limited only at the surface of the rolled strip. Through asymmetric rolling the high shear zone can be extended to the centre of the strip. Hence asymmetric rolling of thin strip could be a potential method for industrial application of DIFT. A recent work by Morimoto et al. suggested that asymmetric rolling leads to DIFT and the combination of both grain refinement techniques provides an efficient way to produce ultra fine grained steels in a hot mill [34].

Several researchers have quantified the necessary deformation temperature and amount of deformation to introduce DIFT in different chemistries. However, there are other processing parameters which affect the final microstructure obtained by this technique,

e.g. prior austenite grain size, cooling rate from the austenitization temperature to the deformation temperature, and strain rate. A systematic study of the effect of processing parameters on DIFT is necessary to understand this novel technique.

2.2.6 Advantages of Deformation Induced Ferrite Transformation

Application of asymmetric hot rolling to produce fine grained steel strip is an extrapolation of the TMCP of steel. Although this gives finer ferrite grains than the TMCP of steel, still, further ferrite grain refinement can be achieved through DIFT. Combining DIFT with the rapid cooling pattern for hot rolled dual phase steels appears to be a suitable route to produce ultra fine grained dual phase steel. Other grain refinement techniques do not permit such a straight forward processing route. For example, ferrite grain refinement by dynamic recrystallization of ferrite was achieved in the ferrite phase region. To form martensite after ferrite grain refinement by dynamic recrystallization of ferrite, the steel was reheated to the intercritical region and subsequently quenched. To reheat flat steel products intermediately is difficult in industrial application. The drawback of the ECAP route is that it is not applicable for flat steel products. The advantage of DIFT over the cold rolling and annealing of martensite technique is that the former can be implemented into existing hot rolling mills, whereas, the later needs an additional annealing step.

As DIFT was selected for ferrite grain refinement in this study, the following two sections are devoted to describe the processing parameters and grain refinement mechanism for DIFT.

2.3 Processing parameters for DIFT

Different processing parameters that can influence DIFT are prior austenite grain size, strain, strain rate, and deformation temperature. These parameters are interrelated and at times, it is difficult to discuss the effect of one parameter on DIFT independently. Here in the effects of different processing parameters on DIFT are discussed together instead of discussing one at a time.

Strain is one of the most important parameters for ultra fine ferrite formation (UFF) through DIFT processing. Beladi et al. defined two strain conditions for DIFT [35]. The strain value for the start of DIFT is called as the critical strain for DIFT ($\epsilon_{C,DIFT}$). But the strain to produce an ultra fine ferrite final microstructure through DIFT processing is higher than $\epsilon_{C,DIFT}$. This strain is called as critical strain for ultra fine ferrite formation ($\epsilon_{C,UFF}$). At strains higher than $\epsilon_{C,UFF}$ the final microstructure does not change significantly. According to Choi et al. deformation accelerates the rate of austenite to ferrite transformation, both in terms of nucleation (i.e. transformation start) and growth [36]. **Figure 2.5** schematically represents the effect of strain on the start of the austenite to ferrite transformation. For a small strain ($\epsilon=\epsilon_1$) dynamic transformation (i.e., transformation during deformation) does not occur at all. For higher strain ($\epsilon=\epsilon_2$) transformation starts during deformation and thus, occurs as dynamic transformation.

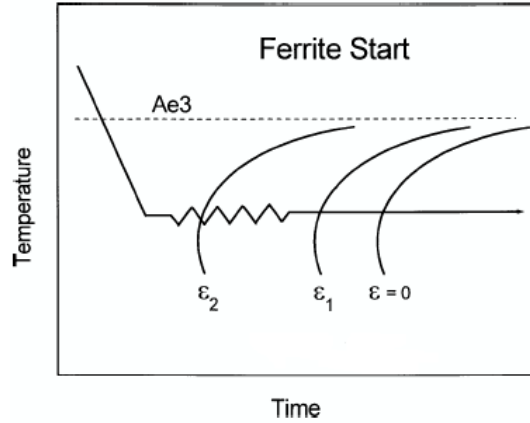


Figure 2.5: Schematic representation of the variation of the transformation start curve as a function of strain [36].

Figure 2.6 shows that $\epsilon_{C,UFF}$ decreases with increase in ΔT^* [4]. This behaviour is expected because of the increase in driving pressure for the austenite to ferrite transformation with increasing ΔT^* . The volume fraction of ferrite formed by DIFT increases with increase in strain as illustrated in **Figure 2.7** for a C-Mn-V steel [35].

Hickson et al. studied DIFT in a C-Mn steel, austenitized at 1250°C, in different deformation modes: rolling, compression, and torsion [8]. They observed different critical strains for formation of UFF. In rolling, a nominal strain between 0.3 and 0.4

$\left(\epsilon_{VM} \text{ for rolling} = \frac{2}{\sqrt{3}} \text{ nominal strain} = 0.35 \text{ and } 0.46 \right)$ was sufficient to form a fully

ultra fine ferrite structure at the surface of the rolled sheets. But for the compression test a strain of 0.5 (ϵ_{VM} for uniaxial compression = strain = 0.5) was not sufficient to form a large volume fraction of ultra fine ferrite. For the torsion test, even a Von Mises equivalent strain of 3.0 was insufficient to form a predominantly ultra fine ferrite

structure. However, their study did not mention the required strains to form a predominantly ultra fine ferrite microstructure through compression and torsion. Hickson et al. performed a finite element modelling of the rolling practice used in their work. The modelling suggested that the strain in the surface layer was up to 2.8 times higher than the nominal strain [8]. This might be the reason for the formation of UFF microstructure at the surface of the rolled sheet.

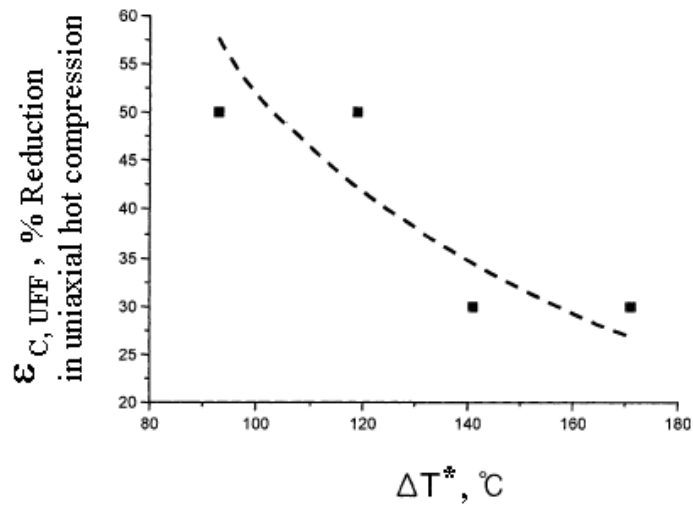


Figure 2.6: The critical amount of reduction $\epsilon_{C, UFF}$ with degree of undercooling (ΔT^*) for a low carbon steel (0.14C-1.5Mn-0.79Si, in wt%) [4].

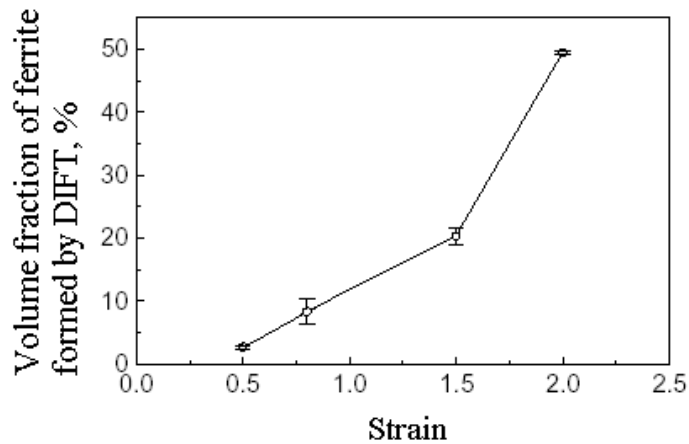


Figure 2.7: Volume fraction of ferrite formed by DIFT as a function of strain for austenitization and deformation temperatures of 1200 and 775°C, respectively for a C-Mn-V steel [35].

Beladi et al. studied the effect of strain rate on DIFT for a C-Mn-V steel. They reported that lowering the strain rate from 1 s^{-1} to 0.1 s^{-1} increased the mean ferrite grain size and decreased the polygonal ferrite fraction [35]. For the lower strain rate they observed that some of the ferrite grains contain many subgrains. For higher strain rate the time between the finish of deformation and the start of quench is important. As discussed later in more detail, this time can be significant as compared to the actual time of deformation.

The effect of prior austenite grain size on DIFT is still not conclusive. According to Beladi et al. finer prior austenite grains have more potential for DIFT as compared to larger prior austenite grains [35, 37]. However, Hurley et al. argued that larger prior

austenite grains suppress formation of grain boundary proeutectoid ferrite and encourage DIFT [30].

Beladi et al. and Hurley et al. selected deformation temperatures, which were in between Ae_3 and Ar_3 . Their selection of the deformation temperature did not have any specific relation with the Ar_3 temperature, i.e. deformation temperature minus Ar_3 (ΔT) was not selected in a systematic fashion [30, 35, 37]. However, several research groups used deformation temperatures that were dependent on the Ar_3 temperature. For example, Hong et al. utilized a deformation temperature which was 10°C above the Ar_3 temperature [38].

A systematic study was done by Hong et al. to characterize the effect of pre-deformation cooling rate on DIFT [4]. They reported that the Ar_3 temperature decreased with an increase in the cooling rate. Further, they decreased the deformation temperature at par with the decrease in the Ar_3 temperature. They found that 20% compressive reduction introduced fine ferrite grains (~2 μm in size) for higher cooling rates (5°C/s and 10°C/s); while these fine ferrite grains were not observed for lower cooling rates (0.5°C/s and 2°C/s). With the increase in deformation, the effect of cooling rate on final microstructure became negligible. In the case of 70% reduction a similar final microstructure (in terms of ferrite grain size and ferrite fraction) was obtained for all cooling rates. It is difficult to separate the effect of pre-deformation cooling rate from the effect of deformation temperature as the cooling rate from the austenitization temperature also affects the Ar_3 temperature, which in turn affects the deformation temperature.

Alloying elements and prior austenite grain size affect the A_{r3} temperature. Subsequently, the A_{r3} temperature affects the deformation temperature for DIFT. Hong et al. [38] reported the effect of Nb on A_{r3} temperature (**Table 2.2**). It can be observed from **Table 2.2** that the microalloying element Nb has complex effects on A_{r3} temperatures. The decrease in A_{r3} temperature with increasing reheating temperature for a particular chemistry can be attributed to the increasing austenite grain size as summarized in **Table 2.2**. For the C-Mn steel the A_{r3} temperature decreased only by 20°C when the austenite grain size was increased from 25 to 240 μm . But, for the Nb steel the A_{r3} temperature decreased by 60°C when the austenite grain size was increased from 20 to 200 μm . This is due to the fact that in the case of Nb steel the higher reheating temperature that leads to larger austenite grain size also increases the amount of Nb in solution. And this dissolved Nb delays ferrite transformation by solute drag.

Table 2.2: A_{r3} temperatures (cooling rate from reheating temperature is 2°C/s and austenite grain sizes are indicated in brackets) [38]

Reheating temperature, °C	900	1000	1100	1250
C-Mn steel (0.14 wt% C, 1.5 wt% Mn, 0.8 wt% Si)	740°C (25 μm)	730°C (35 μm)	725°C (130 μm)	720°C (240 μm)
Nb steel (same base chemistry with 0.052 wt% Nb)	762°C (20 μm)	753°C (25 μm)	715°C (100 μm)	705°C (200 μm)

For the lower reheating temperatures (900°C and 1000°C) the differences in A_{r3} temperatures of Nb steel and C-Mn steel can be attributed to the effect of austenite grain size on the A_{r3} temperature. That is, there is an increase in A_{r3} temperature with a decrease in austenite grain size. But for the higher reheating temperatures (1100°C and 1250°C) the A_{r3} temperatures are lower for the Nb steel even though the austenite grain sizes are lower as compared to the C-Mn steel. This is due to the fact that higher reheating temperatures dissolve more Nb into austenite solid solution and delay the ferrite formation in the Nb steel.

Hong et al. studied the effect of undercooling (ΔT^*) on the amount of ferrite formed by DIFT (**Figure 2.8**) [4]. From **Figure 2.8** it can be observed that for lower strain increasing the undercooling increases the amount of ferrite formed. In their study they applied a strain rate of 10s^{-1} and thus, the maximum strain of 1.2 (for 70% reduction) was attained in 0.12 s. However, this time is much less than the time gap between the end of deformation and the start of water quench. They reported that the water quench was started within 1 s after the end of deformation. Thus, a significant amount of ferrite could also form after deformation (the lowest deformation temperature was 683°C and it could be expected that the specimen temperature did not go below the ferrite formation stop temperature before the start of the water quench).

Beladi et al. [35] reported the effect of post deformation cooling rate on UFF formation in a C-Mn-V steel. They concluded that post deformation cooling rate has an effect on $\mathcal{E}_{C,UFF}$ and ferrite grain refinement. The $\mathcal{E}_{C,UFF}$ significantly increased with a decrease in

the cooling rate. While, for a given strain the ferrite grain refinement increased with an increase in the cooling rate. They suggested that for a given steel composition and initial austenite microstructure, there is a maximum cooling rate to obtain a fully ultra fine ferritic microstructure. Employing a cooling rate higher than the maximum cooling rate yields non-polygonal structures even at further increased strain levels. This suggests that time between deformation and cooling as well as initial cooling stages (in ferrite region) are significant for the formation of ultra fine ferritic microstructure.

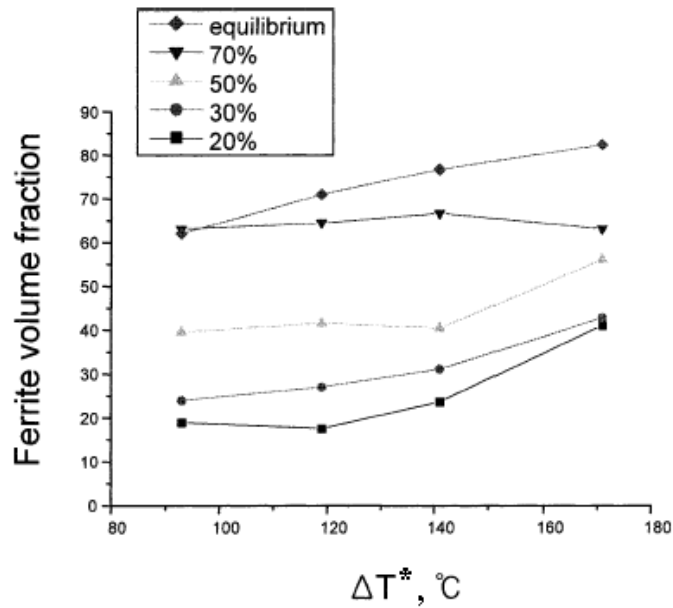


Figure 2.8: The variation of ferrite volume fraction with degree of undercooling (ΔT^*) for different amounts of reduction in a low carbon steel (0.14C-1.5Mn-0.79Si, in wt%) [4].

Beladi et al. [37] reported that the growth of ferrite grains during post deformation cooling was altered by different initial austenite grain sizes. Consequently, the coarse and the fine austenite grains exhibit different ferrite grain–size distributions produced by DIFT. They argued that in the case of finer prior austenite grain, both grain boundary ferrite and intragranular ferrite coarsened in similar fashion resulting in a homogeneous final ferrite grain size distribution [37]. But, for the coarse austenite grain the coarsening rate of ferrite grains formed in the austenite grain boundary region was slower than the coarsening rate of ferrite grains formed in the austenite grain interior. This resulted in a more inhomogeneous ferrite grain size distribution for coarse grained austenite as compared to fine grained austenite.

Figure 2.9 shows the effect of post deformation isothermal holding time for a V-Nb microalloyed steel which was deformed 80% at 751°C ($A_{r3}+10^{\circ}\text{C}$) [39]. With increasing isothermal holding time both ferrite volume fraction and mean ferrite grain size are increased. This increase in ferrite volume fraction may be attributed to the new ferrite grains formed during the isothermal holding. Also, the growth of the dynamically formed ferrite may increase the final ferrite fraction and the final ferrite grain size. However, from the data of **Figure 2.9** it can be estimated that the increase in ferrite fraction is due to the growth of ferrite only. Because, assuming that for a particular holding time, all ferrite grains have the same size as reported in the graph, the number of ferrite grains for a normalized volume decreases with increase in isothermal holding time. Examination of misorientation angle between neighboring grains indicated that for a holding time of 10 s the grain boundaries were made up of a mixture of high and low angle boundaries, while

for a holding time of 100 s the grain boundaries were made up of mostly high angle boundaries [39].

Kelly et al. [31] studied the effect of post deformation isothermal holding in a plain C steel at 760°C. They reported that the mean ferrite grain size increased and the grain size distribution broadened during the isothermal hold. Further, the isothermal hold also decreased the proportion of lower misorientation angle in the distribution of misorientation angles between the adjacent ferrite grains.

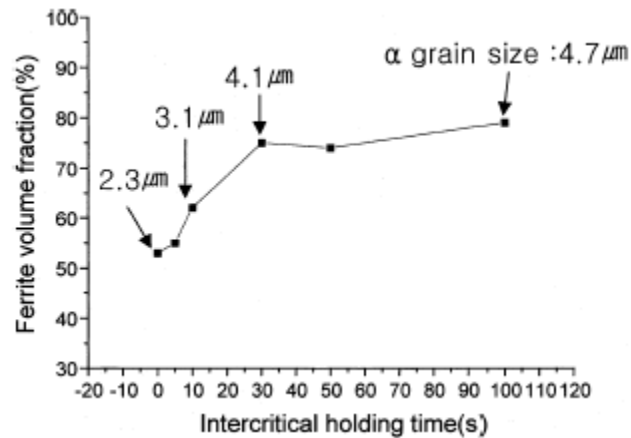


Figure 2.9: The effect of post deformation isothermal holding time on ferrite fraction and grain size for a V-Nb microalloyed steel [39].

However, Cho et al. [40] argued that dynamically formed ferrite grains were very stable against grain growth even at elevated temperature. In their study they found that during isothermal holding at 700°C for 10 min after 50% deformation a mixture of fine ferrite grains (~2-3 μm) and coarse ferrite grains (~7-8 μm) were observed in 0.15 wt% C-0.3

wt% Si-1.2 wt% Mn steels with and without V microalloying. They proposed that the fine ferrite grains (2-3 μm) nucleated and grew during deformation along prior austenite grain boundaries, while the coarse ferrite grains (~7-8 μm) nucleated and grew during isothermal holding. But, a detailed description to distinguish between the dynamically formed ferrite and statically formed ferrite was not included in this study. Therefore, the ferrite grains which were 7-8 μm in size might well have been formed during deformation and later grew to their final size during isothermal holding. Further, the critical strain for DIFT was not reported and the applied deformation might have been below this critical strain.

The major challenge in a systematic analysis of different processing parameters on DIFT is that all the parameters are interlinked to each other. In general, it can be said that a high amount of deformation and a high amount of undercooling below the A_{e3} temperature enhances DIFT. However, the amount of deformation and the strain rate are not independent parameters for DIFT. The effect of prior austenite grain size on DIFT is still not conclusive. It was also observed that the post deformation cooling rate influences the amount of deformation to introduce DIFT. The prior austenite grain size also affects the amount of deformation to introduce DIFT and the post deformation cooling rate to obtain an ultra fine ferritic structure.

2.4 Mechanisms of DIFT

2.4.1 Ferrite nucleation sites in deformed austenite

When undeformed austenite transforms to ferrite, ferrite nucleates at typical heterogeneous nucleation sites such as grain corners, edges and surfaces, in that order of preference [41]. However, in deformed austenite, there are additional nucleation sites both at the grain boundaries, i.e. due to pancaking and associated increase in the grain boundary area, and inside the austenite grains, due to the presence of microbands, microshearbands, and also high angle misorientation boundaries [42-44]. The activation of intragranular ferrite nucleation sites is dependent on prior austenite grain size, amount of deformation, and mode of deformation.

Hurley et al. proposed that the alloy Ni-30% Fe, which has a similar stacking fault energy (75 mJ/m^2) as compared to austenite of low C steel, can be examined to study the evolution of the deformed structure in undercooled austenite [44]. As the alloy retains the austenitic structure till room temperature it is easy to do microstructural analysis of the deformed austenite. Microstructural evolution of low temperature deformation of this alloy was reported for three sets of austenite grain sizes ($\sim 20 \mu\text{m}$, $\sim 125 \mu\text{m}$, and $210 \mu\text{m}$). In some cases, direct comparisons were made between microstructures obtained by deformation of steel and Ni-30% Fe alloy for similar austenite grain sizes and similar thermomechanical paths. These comparisons were helpful in identifying the nucleation sites for DIFT.

Hurley et al. [44] studied nucleation sites for DIFT for a prior austenite grain size of 200 μm . They rolled a Ni-30% Fe alloy and a 0.095 wt% C-1.6 wt% Mn-0.22 wt% Si-0.27 wt% Mo steel at 800°C for this purpose. They reported that for the highest amount of strain achieved at the surface of the rolled strip, intragranular ferrite nucleates at the cell boundaries of the microshearbands produced within the austenite grains. The planes of the microshearbands are within 20° to the rolling direction. The cell boundaries of the microshearbands are planar defects of significant elastic strain energy stored within the deformed austenite grains as they accommodate moderate to high local lattice misorientation. The high density of the potential ferrite nucleation sites is one of the major factors to obtain ultra fine ferritic microstructure through DIFT. The scale of the dislocation cell structure in the austenite was found to be consistent with the final ultra fine ferrite grain size observed [44]. According to Hurley et al. ferrite embryos form at the cell-boundary junctions and along the boundaries of the dislocation cells [44].

Suh et al. studied the effect of strain on the microstructure of the Ni-30Fe% alloy to predict the ferrite nucleation sites for DIFT in low carbon steels [45]. They experimentally determined the variation of high angle misorientation boundary spacing with strain for an austenite grain size of 20 μm , deformation temperature of 700°C, and strain rate of 10s^{-1} , (**Figures 2.10** and **2.11**). They compared these spacings with the ferrite grain size obtained for low C steels [46-47] with similar deformation conditions and prior austenite grain size (**Figure 2.11**).

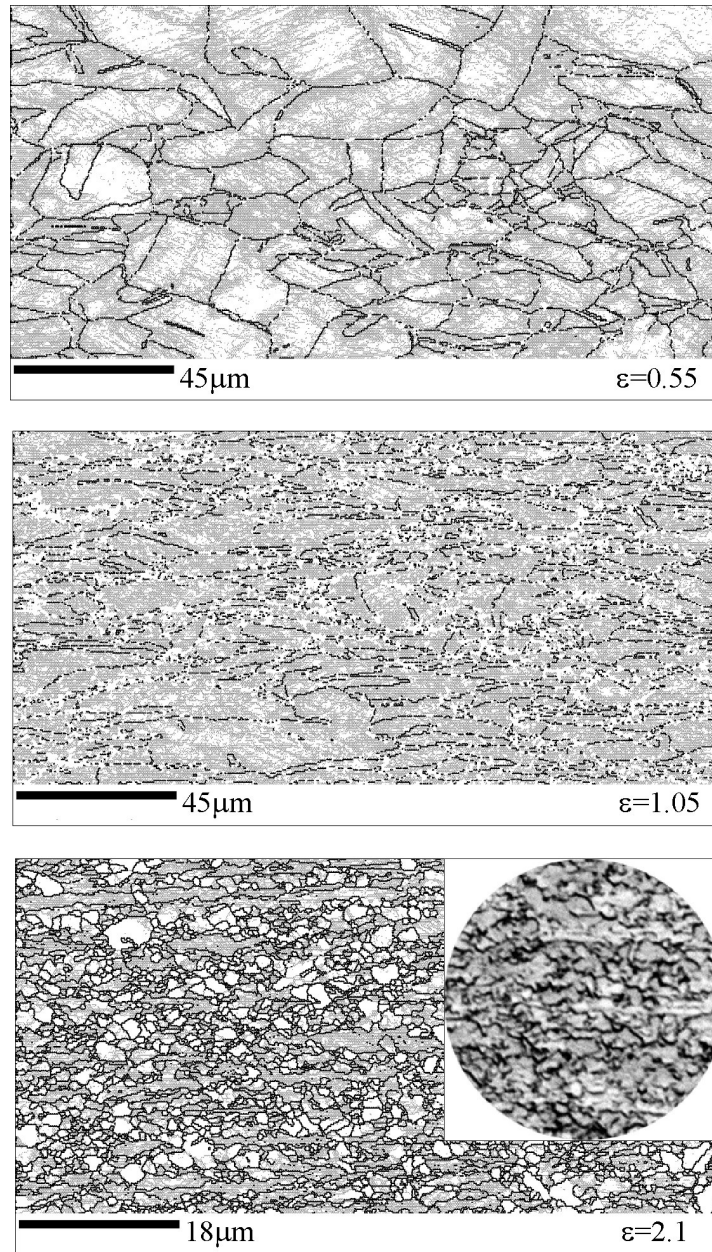


Figure 2.10: High angle grain boundaries ($>15^\circ$) in compressively deformed Ni-30% Fe alloy (deformation temperature 700°C , initial austenite grain size $20\mu\text{m}$), (inset for $\epsilon=2.1$ shows an optical micrograph) [45].

From **Figure 2.11** Suh et al. concluded that the ferrite grain size obtained in steel was similar to the high angle misorientation boundary spacing in austenite [45]. They proposed that the ferrite nucleation occurred at high angle misorientation boundary in the severely plastic deformed austenitic structure.

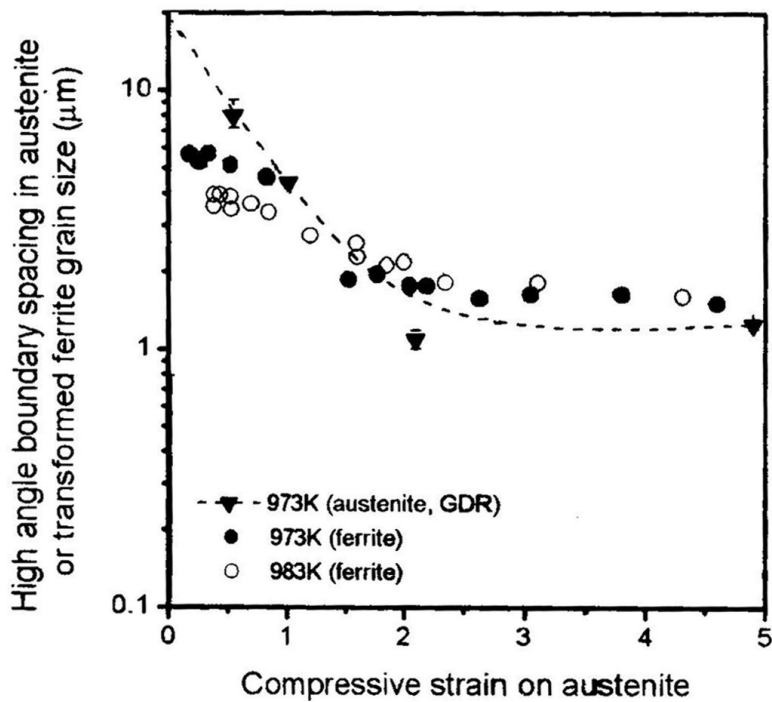


Figure 2.11: High angle misorientation boundary spacing in austenite for a Ni-30% Fe alloy and ferrite grain size for a low C steel, as a function of compressive strain in austenite [45-47], GDR: Geometric dynamic recrystallization.

Further, Suh et al. reported that in the Ni-30Fe% alloy geometric dynamic recrystallization occurred at a strain of 2.1 at 700°C for a prior austenite grain size of 20 μm [45]. Unlike discontinuous dynamic recrystallization, geometric dynamic nucleation does not occur by nucleation of strain free grains. Geometric dynamic recrystallization is a result of interpenetration of serrated grain boundaries. The recovered structures such as dislocation cells and deformation bands are unaffected by geometric dynamic recrystallization. However, as the geometrically recrystallized structure is evolved, additional deformation does not alter the high angle misorientation boundary spacing. Suh et al. adopted this concept in the case of DIFT in steel and predicted that the finest ferrite grains are produced when the geometrically recrystallized austenite grains reaches the smallest possible size. As the smallest possible size of the geometrically recrystallized austenite grain is the subgrain size (0.6 μm) [45], the smallest possible high angle misorientation boundary spacing will be 0.6 μm . Hence, the smallest ferrite grain observed in case of DIFT will be 0.6 μm .

Suh et al. theoretically calculated the strain needed for geometric dynamic recrystallization to occur in a Ni-30% Fe alloy at 700°C [48]. They argued that this occurred when the thickness of the deformed austenite grain decreased to the amplitude of the grain boundary serrations. They assumed that the maximum serration amplitude of the austenite (A_s) grain boundary was 5.5 μm . Thus, the critical strain for geometric dynamic recrystallization to occur for a 20 μm initial austenite grain size (d_γ) was $\ln(A_s/d_\gamma)=1.3$.

Beladi et al. studied the evolution of microstructure in a Ni-30% Fe alloy with a prior austenite grain size of 110 μm in a torsional mode of deformation at 700°C [28]. They reported the formation of microbands within a strain of 1. These microbands were inclined at an angle of 45° with the direction of the macroscopic shear. They predicted that the microbands acted as a potential ferrite nucleation site for steels with similar austenite grain size.

2.4.2 Growth of DIFT ferrite

Beladi et al. reported that $\epsilon_{C,UFF}$ depended on post-deformation cooling rate. They found that $\epsilon_{C,UFF}$ significantly increased with a decrease in the post-deformation cooling rate [35]. This could be explained by the fact that, for slower cooling rate a significant amount of ferrite forms after deformation. Whereas, for faster cooling rate there is little time available for austenite to ferrite transformation after deformation. Thus, for the higher post-deformation cooling rate the $\epsilon_{C,UFF}$ is higher as a significant amount of ferrite has to be formed during deformation. Cho et al. [40] depicted a simple procedure to find out the amount of ferrite dynamically formed during DIFT. They assumed that the equilibrium fraction of each phase was not significantly affected by strain energy. They proposed that the difference in dilations between non-deformed and deformed specimens during isothermal holding could be interpreted as the ferrite dynamically formed during deformation. In the case of deformed specimen the dilation was measured after the deformation and normalized by the diameter of the specimen just after deformation. In their steel they found that almost 60% ferrite is formed during deformation at 700°C.

Further, from the experiment they found that the transformation rate of the remaining austenite was accelerated after deformation, as compared to the transformation rate of the undeformed austenite. However, various research groups claimed that ferrite was formed dynamically from austenite and not during post deformation treatment [49-51]. Recent studies by Dong et al. and Zheng et al. quantified the enhancement of the austenite to ferrite driving pressure during DIFT by the stored energy of the work hardened austenite [52-53]. However, Beladi et al. argued that the deformation had insignificant effect on the free energy of austenite to ferrite transformation and diffusion of elements [28].

2.4.3 Dynamic recrystallization of austenite vs. DIFT

Choi et al. argued that DIFT and dynamic recrystallization are similar phenomenon as they are both dynamic softening mechanisms of deformed austenite [36]. Consequently, they applied the method of Poliak et al. [54] developed for dynamic recrystallization, to determine the critical strain for DIFT. Poliak et al. [54] analyzed the onset of dynamic recrystallization in terms of thermodynamics and kinetics based on the principles of non-equilibrium thermodynamics. They deduced that the initiation of dynamic recrystallization required two conditions: local maximum stored energy and minimum dissipation rate. Using this approach, Choi et al. determined the critical strains for DIFT/dynamic recrystallization of austenite from their experimental stress-strain curves [36]. These critical strains are given in **Figure 2.12**. In this set of experiments the cooling rate employed from the austenitization temperature to the deformation temperature was 2°C/s. The results of the microstructural investigations are also included in **Figure 2.12**:

the dynamic recrystallization of austenite are reported as open symbols, the DIFT are reported as closed symbols, and the DIFT after ferrite transformation start are reported as half solids.

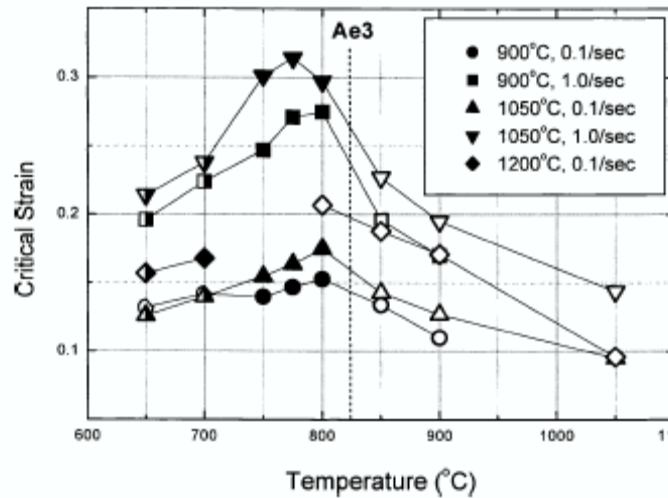


Figure 2.12: Change of critical strain for DIFT (or dynamic recrystallization of austenite) with deformation temperature. Results of microstructural investigation are indicated as open marks (dynamic recrystallization of austenite), solid marks (DIFT), and half solid marks (DIFT after ferrite transformation start) [36].

From **Figure 2.12** it is seen that below the Ae_3 temperature, DIFT takes place rather than dynamic recrystallization of austenite (except for T_γ of 1200°C and a strain rate of 0.1/s). Also the critical strain for DIFT decreased with decreasing temperature. Further, the critical strain for DIFT also decreases with decreasing austenitization temperature. On the other hand there was a significant increase in critical strain with increasing strain rate. In case of dynamic recrystallization of austenite the critical strain increases with increasing

Zener-Holloman parameter. However, for DIFT the temperature has an opposite effect, i.e., as temperature decreases the Zener-Hollomon parameter increases (for a constant strain rate), but the critical strain for DIFT decreases with temperature.

2.4.4 Effect of microalloying elements on DIFT

Although DIFT is observed in all steel chemistries by a suitable choice of processing parameters, the effect of different alloying elements on DIFT reveals some interesting facts. In the case of microalloyed steel, Nb affects DIFT differently depending on whether it is in solid solution or it is in precipitate form (NbC) [38]. When Nb was dissolved, DIFT was hardly observed even after reduction of 80% [38]. This was attributed to the retarding effect of Nb on austenite to ferrite phase transformation. When NbC preexisted, the DIFT kinetics was similar to that of C-Mn steels. However the ferrite grain size was reported to be finer than that in C-Mn steels. Hutchinson et al. studied the effects of Nb in solid solution in austenite and NbC precipitate in austenite on the retardation of austenite recrystallization during hot-rolling of steel [55]. They reported that the fine NbC precipitates (2-10 nm in size) were more efficient than the solute drag in retarding the recrystallization of austenite for most of the conventional hot-rolling temperatures (>900°C). Whereas at low temperatures (<900°C), probably, the solute drag was more effective than the NbC precipitates to retard austenite recrystallization [55]. Thus, for achieving DIFT, where austenite has to be deformed at low temperature, NbC precipitates are preferred over Nb in solid solution in austenite. This retards austenite recrystallization and at the same time does not affect the austenite to ferrite

transformation. Cho et al. studied the effect of addition of V on DIFT. According to them, V addition to low carbon steels enhances DIFT [40]. They attributed this to the presence of V(C,N) particles. Hickson et al. studied DIFT in a low carbon (0.04 wt% C) steel microalloyed with Mo and B. It was concluded that austenite stabilizers such as Mo and B do not enhance the ultrafine ferrite formation [56].

2.5 Modelling the austenite to ferrite transformation

The austenite to ferrite phase transformation has an important effect on the final properties of steel products. For example, the final ferrite grain size and the ferrite fraction affect the tensile properties of steels. A number of models were proposed to describe this technologically important transformation in steels. Based on the underlying physics, these models can be categorized as: (i) empirical JMAK (Johnson-Mehl-Avrami-Kolmogorov) model [57-66], (ii) physical based models, (iii) stochastic Monte Carlo model [67], and (iv) Cellular Automaton model. The physical based models are: (a) carbon-diffusion-controlled model [64, 68-73], (b) interface-controlled model [70, 74-78], and (c) mixed-mode model [53, 79-88]. Based on the application approach the austenite to ferrite transformation models can be classified as: (i) macroscopic length scale approach, and (ii) mesoscale approach [89]. In general, the austenite to ferrite transformation models predicted the effects of various processing parameters on the final microstructure of steels. For example, the JMAK approach can describe the final ferrite fraction based on the cooling strategy of the run-out table. In addition to the ferrite fraction the final ferrite grain size distribution can be predicted by mesoscale approaches.

2.5.1 Macroscopic length scale approach

In this approach some average microstructure property (e.g. ferrite fraction, grain size), of a macroscopic domain was considered. The JMAK model and the physical based models of the austenite to ferrite transformation models were implemented through this approach.

2.5.1.1 The JMAK model

Kolmogorov [57], Johnson and Mehl [58], and Avrami [59-61] described the isothermal kinetics of diffusional phase transformations by the following equation (JMAK equation):

$$X = 1 - \exp(-bt^n) \quad (2.2)$$

where X is the fraction transformed, b is a temperature dependent rate parameter related to the magnitude of the nucleation and growth rates, n is a parameter that depends on nucleation site saturation, continuous nucleation etc. and the dimensionality of the growing particle (1D, 2D, 3D) that, at least in part, is related to the activated nucleation sites (grain corners, grain edges, grain faces etc.).

Unemoto et al. modified the JMAK equation for the austenite to ferrite transformation [62]. They argued that the austenite to ferrite transformation kinetics should depend on the initial austenite grain size as ferrite nucleation occurs heterogeneously at prior austenite grain boundaries, edges or corners. Hence, the modified JMAK equation includes the initial austenite grain size d_γ :

$$X = 1 - \exp\left(\frac{-bt^n}{d_\gamma^m}\right) \quad (2.3)$$

Here b_l is a temperature dependent rate parameter, and m is a fitting parameter that is related to nucleation and growth conditions. n has the same significance as described for **Equation 2.2**. For the austenite to ferrite transformation, the value of n is usually reported to be ~ 1 [63]. This indicates nucleation site saturation and one-dimensional ferrite growth from austenite grain boundaries [63]. Further, to model the transformation during continuous cooling conditions which are relevant for industrial processing, the additivity principle was employed successfully. Here continuous cooling (or heating) transformation behavior is described as the summation of a series of short durations of fractional isothermal transformations events. Scheil [65] applied isothermal kinetics to non-isothermal conditions by adopting nucleation during cooling based on the incubation period associated with isothermal transformation. Christian [66] suggested that additivity is fulfilled when the transformation rate can be expressed with two independent functions, one of which depends on the instantaneous temperature and the other on fraction transformed, respectively, i.e.:

$$\frac{dX}{dt} = \frac{\xi(T)}{\xi_a(X)} \quad (2.4)$$

Reactions that are additive are so-called isokinetic reactions. Differentiating **Equation 2.2** with respect to time:

$$\frac{dX}{dt} = \frac{n(-b)^{-n}}{(1-X)^{-1} \left(\frac{1}{\ln(1-X)} \right)^n} \quad (2.5)$$

is obtained indicating that the criterion for additivity is fulfilled for the JMAK equation provided $b = f(T)$ and $n = const$.

2.5.1.2 The physical based transformation models

For carbon-diffusion-controlled model of austenite to ferrite transformation, it was assumed that the equilibrium carbon concentrations in ferrite and austenite are attained instantaneously at the moving austenite/ferrite interface. Based on this assumption Vandermeer proposed a simple ferrite growth equation (**Equation 2.6**) [90]. He assumed simple spherical growth geometry of ferrite in this approach.

$$\frac{dR_f}{dt} = D_\gamma^c \frac{C_\gamma^{eq.} - C_0}{C_\gamma^{eq.} - C_\alpha^{eq.}} \frac{1}{R_f} \quad (2.6)$$

where R_f is the radius of the growing ferrite grain, and C_0 is the average carbon concentration of the steel. However, in this simple approach it was assumed that growth of ferrite occurred without impingement. Militzer et al. modified this simple ferrite growth equation to model ferrite growth from the ferrite nucleation temperature (the temperature at which there are reasonable ferrite nuclei form at grain corners) to the measurable austenite to ferrite transformation start temperature in C-Mn steels. [73]. The required modification was done to implement the retarding effect of Mn on ferrite growth.

Kamat et al. modelled the austenite to ferrite transformation by assuming that carbon diffusion in the remaining austenite was the rate-controlling step. They assumed a simple austenite geometry model [64] where in a spherical austenite grain with a diameter replicating the austenite grain size, a ferrite shell was growing inward from the surface of the sphere (prior austenite grain boundary). Assuming a spherical ferrite-austenite

interface, they modelled the unsteady state carbon diffusion in the remaining austenite grain. The ferrite growth velocity was derived by a mass balance at the austenite/ferrite interface. This model was reported to describe the austenite to ferrite transformation in steels, containing 0.2wt% or more carbon, with reasonable accuracy [70]. Militzer et al. suggested that the carbon-diffusion-controlled model could be extended to Fe-C-Mn steels by modifying the boundary conditions at the austenite/ferrite interface to account for Mn segregation [73]. Growth of ferrite requires redistribution of both carbon and Mn. As the equilibrium Mn concentration in ferrite is lower than that for austenite, during ferrite growth Mn atoms segregate to the austenite/ferrite interface. But as Mn diffusion in austenite is a comparatively slow process Mn enrichment is restricted to the interface region and long range diffusion is usually negligible. The segregation of Mn at the austenite/ferrite interface reduces the interfacial carbon concentration. This results in a decrease of the gradient for carbon diffusion. Hence, Mn is considered to exert a solute drag like effect on the austenite/ferrite interface movement. Militzer et al. proposed a segregation model for Fe-C-Mn steels where the solute drag of Mn at the austenite/ferrite interface changes the interfacial carbon activity. This model was applied to describe the ferrite transformation kinetics in low carbon steels during continuous cooling [73].

The drawback of the diffusion-controlled model is that it is unsuitable to describe the austenite to ferrite transformation in ultra low carbon steels and interstitial free (IF) steels. Due to their very low carbon content, carbon diffusion plays a less significant role in the phase transformation of these steels. Kinetics of lattice transformation or interface reaction is then the rate-controlling step for the austenite to ferrite transformation. Kop et

al. [74] studied the austenite to ferrite transformation during continuous cooling for three commercial lean C-Mn grade steels based on the concept of interface mobility. They described the ferrite-austenite interface velocity v as:

$$v = \mu_{\gamma\alpha} \Delta G_V \quad (2.7)$$

and

$$\mu_{\gamma\alpha} = \mu_{\alpha\gamma}^0 \exp\left(-\frac{Q}{RT}\right) \quad (2.8)$$

where, $\mu_{\alpha\gamma}$ is the ferrite-austenite interface mobility, $\mu_{\alpha\gamma}^0$ is the pre-exponential term for the ferrite-austenite interface mobility, Q is the activation energy of the mobility of the interface, and ΔG_V is the Gibbs free energy difference between the austenite and the ferrite phases. For the low carbon steels, it was assumed that during austenite to ferrite transformation the carbon rejected by the growth of ferrite was immediately distributed homogeneously in the remaining austenite. Hence, the carbon concentration in the remaining austenite (C_γ) was calculated using a simple mass balance between the loss of carbon by the growth of ferrite and the increase of carbon concentration in the remaining austenite. The carbon concentration in ferrite was always considered to be the equilibrium carbon concentration (C_α^{eq}). ΔG_V was calculated as a function of chemical free energy difference between austenite of carbon composition C_γ and ferrite of carbon concentration C_α^{eq} . In their study, Kop et al. employed $\mu_{\alpha\gamma}^0$ as the fit parameter. Through suitable choices of the $\mu_{\alpha\gamma}^0$'s, their model satisfactorily described the transformation rates at all cooling rates. Regarding the nucleation sites for ferrite, they assumed that the initial austenite grain was tetrakaidecahedron in shape and the ferrite grains nucleated at the corners of the initial austenite grain. To modify the interface-controlled model for alloyed

steel the following considerations were made: As the degree of disorder in the interface was much higher than that in the adjacent grains, the substitutional solute atoms segregated in the interface. During the movement of the interface, these segregated atoms move with the interface by diffusion. This significantly decreases the interface mobility. This is called as solute drag effect. Several researchers solved this problem by incorporating the effect of solute drag in the $\mu_{\alpha\gamma}^0$ or in the ΔG_V term [70, 75-78].

Low-carbon steels fall into the region where there is a potential overlap of carbon diffusion and interface controlled growth modes. Thus, a mixed-mode model approach was introduced where the carbon diffusion in the remaining austenite was coupled with the interface reaction to describe the ferrite growth behaviour [79]. According to this model, the interface carbon concentration on the austenite side changes with time. It changes from the initial carbon concentration of austenite C_0 , to the equilibrium carbon concentration of austenite C_γ^{eq} . The non-zero net carbon flux at the interface is responsible for the carbon build up at the interface. Krielaart et al. described the austenite to ferrite transformation in a Fe-0.2 wt% C steel using the mixed-mode model [79]. In their study they assumed a simple austenite geometry, where in a spherical austenite grain with a diameter replicating the austenite grain size, a ferrite shell was growing inward from the surface of the sphere (prior austenite grain boundary). Further, the ferrite-austenite interface was assumed to be flat. They refined the interface-controlled model (**Equation 2.7**) to the mixed-mode model by making the following modification: ΔG_V depends on the changing carbon concentration at the interface (i.e. not just simple mass

balance as was done for the interface-controlled model). Further, they considered $\mu_{\alpha\gamma}^0$ to be a fit parameter.

The effect of solute drag can be incorporated into mixed-mode models. To describe the austenite to ferrite transformation in dual-phase and Transformation Induced Plasticity (TRIP) steels by mixed-mode modelling, Fazeli and Militzer included the effect of solute drag [80]. This led to further modifications in calculating ΔG_V . This modification was done by replacing ΔG_V with $(\Delta G_V - \Delta G_{SD})$, where ΔG_{SD} was the energy dissipated by solute drag [80]. ΔG_{SD} depends on the interface velocity and is a function of the solute-interface binding energy and the jump frequency of the solutes across the interface [80].

2.5.2 Mesoscopic length scale approach

The advancement of computer power has made possible the modelling of austenite to ferrite transformation on the meso-scale, i.e. on the length scale of the microstructural features. Physical based models, Monte Carlo model, and Cellular Automaton model were employed in mesoscopic model approaches. The macroscopic length scale approaches of austenite to ferrite transformation are basically ferrite growth models with the assumption of ferrite nucleation site saturation at the prior austenite grain boundary. The mesoscale approaches require both a ferrite nucleation model and a ferrite growth model to describe the austenite to ferrite phase transformation. The ferrite nucleation model should describe the time and spatial appearance of ferrite nuclei in the austenite microstructure.

2.5.2.1 The physical based mesoscopic models

Increasingly 2D and 3D simulation methods of microstructure evolution are implemented with phase field model (PFM). The phase field model is based on the Allen-Cahn equation for a non-conserved order parameter [91]. As the Allen-Cahn equation includes the gradient energy term, diffuse interfaces are considered in the phase field model to quantify the gradient energy. Several researchers simulated austenite to ferrite transformation using the phase field model [82-86].

Mecozzi et al. followed the phase field concept of Steinbach et al. [92] to formulate the single phase field equation for austenite to ferrite transformation in terms of physical parameters [83]. In their formulation the phase field parameter was defined as follows:

$\phi(x,t)=1$ if in the location x at time t the phase ferrite (α) is present.

$\phi(x,t)=0$ if at x at t the phase austenite (γ) is present.

$\phi(x,t)$ changes continuously from 0 to 1 ($0 < \phi(x,t) < 1$), within a transition region at the interface of width η (i.e. diffuse interface).

The phase field evolution equation in terms of physical material parameters was given by,

$$\frac{\partial \phi}{\partial t} = \mu_{\alpha\gamma} \frac{\partial F}{\partial \phi} = \mu_{\alpha\gamma} \left[\sigma_{\alpha\gamma} \left(\nabla^2 \phi - \frac{18}{\eta^2} (1-\phi)\phi \left(\frac{1}{2} - \phi \right) \right) + \frac{6\Delta G_V}{\eta} (1-\phi)\phi \right] \quad (2.9)$$

where, $\mu_{\alpha\gamma}$, $\sigma_{\alpha\gamma}$ and ΔG_V are the interface mobility, the interfacial energy, and the driving force, respectively.

A simple phase field model is equivalent to an interface-controlled model. Combining the phase field model with the diffusion of carbon gives a mixed-mode model of the austenite to ferrite transformation.

Ferrite nucleation mechanism was not incorporated in the phase field formalism, and the method needs nucleation criteria to be imposed for each ferrite grain [93]. Using the nucleation criteria, and the $\mu_{\alpha\gamma}^0$ as adjustable parameters, the calculations of two-dimensional and three-dimensional phase field models were found to replicate the experimental transformation data for different cooling rates in Fe-C-Mn steel accurately [83,93]. Militzer et al. reported simulations in 3D space that provided more accurate morphologies of the final microstructure [82]. In these studies the austenite to ferrite transformation were studied in undeformed austenite. Ferrite nucleation was considered to occur at the prior austenite grain boundary. The adjustable parameter in the ferrite nucleation model was the range of ferrite nucleation temperatures. For a smaller range of ferrite nucleation temperatures, nucleation was assumed to occur both at the austenite grain corners only, while for higher range of nucleation temperature, nucleation was assumed to occur at the grain corners and the grain surfaces. The time distribution of ferrite nucleation gave rise to a ferrite grain size distribution in the final simulated microstructure [93]. Comparison of calculated and measured ferrite grain size distribution provides a criterion to evaluate the proposed nucleation parameters.

2.5.2.3 Stochastic Monte Carlo model for DIFT

Tong et al. used a Monte Carlo (MC) technique to model DIFT in a Fe-C binary system. In this technique the microstructure is mapped onto a two dimensional hexagonal lattice. There are four parameters to describe the state of a Monte Carlo cell: Orientation, carbon concentration, order parameter, and stored energy. The order parameter characterizes the phases in the applied Monte Carlo technique. During transformation of a Monte Carlo cell, the four parameters change simultaneously and randomly. The free energies of the system before and after the aforementioned transition attempts are stored as E_1 and E_2 respectively. The transition is accepted if $E_1 \geq E_2$. Otherwise, the transition occurs with a probability of $W = \exp((E_1 - E_2) / k * T)$, where k^* is the Boltzmann constant, and T is the absolute temperature [67]. Applying this technique to a two dimensional cell structure, isothermal DIFT was modelled at the Ae_3 temperature; the stored energy in the system promotes DIFT. It was reported that DIFT initiated at a strain of 0.104 and the volume fraction of ferrite increased gradually as the deformation proceeded. Here, a nucleation model with a constant nucleation rate was adopted. But the procedure of adding the embryonic nuclei to the system was not explained. They modelled the DIFT at Ae_3 (where $\Delta G_V=0$). The only driving force for DIFT was the deformation energy. But, in this situation it is difficult to accept that DIFT occurs instead of austenite recrystallization.

2.5.2.4 Cellular Automaton Model for DIFT

In the Cellular Automaton approach the state of a cell is defined by several state variables. For austenite to ferrite transformation the state variables considered are a phase state variable (this implies whether the cell belongs to austenite, ferrite or interface), fraction of ferrite (if the cell is at the interface), carbon concentration in austenite, carbon concentration in ferrite, average carbon concentration, etc. Based on the principles of physical based models, the interface velocity for each transforming cell was determined. Some research groups applied Cellular Automaton method for carbon-diffusion-controlled modelling of the austenite to ferrite phase transformation [71, 72]. This technique was used not only to compute the carbon diffusion field but also to track the growth of individual ferrite grains. Lan et al. used the Cellular Automaton method for mixed-mode modelling of the austenite to ferrite transformation [87]. Zheng et al. used this method to model the nucleation scenario during DIFT [53]. They concluded that the ferrite grain refinement in DIFT was possible by repeated ferrite nucleation inside the prior austenite grain. This event started from the grain boundary and gradually took place inside the prior austenite grain, near to the pre-existing austenite-ferrite interface. During the deformation of austenite, they calculated the dislocation density (ρ) with respect to strain (ε) by using the Kocks-Mecking model [94]:

$$\frac{d\rho}{d\varepsilon} = k_1\sqrt{\rho} - k_2\rho \quad (2.10)$$

where k_1 and k_2 are the parameters indicating workhardening and recovery-softening respectively. Further, they calculated the stored energy of the deformation in austenite, as a function of dislocation density.

$$E_{def} = \alpha \rho \mu^* \left| \vec{b} \right|^2 \quad (2.11)$$

where α is a constant, μ^* is the shear modulus, and \vec{b} is the Burgers vector. They added this stored energy of deformed austenite, to the chemical driving force for the austenite to ferrite transformation, ΔG_V , and quantified the ferrite nucleation rate (I_s). They adopted the classical nucleation theory to calculate I_s [95].

$$I_s = K_1 D_\gamma^c (k^* T)^{-\frac{1}{2}} \exp \left(-\frac{K_2}{k^* T (\Delta G_V + E_{def})^2} \right) \quad (2.12)$$

where K_1 is a constant related to the nucleation site density, K_2 is a constant related to the ferrite-austenite interface energy, and k^* is the Boltzmann constant. The addition of E_{def} as an additional driving force for the ferrite nucleation, provided the high density of ferrite nuclei during DIFT [53]. However, the large strain employed at low temperature to impose DIFT, creates deformation structures inside the parent austenite grain, e.g. transition band, microband etc. As discussed in **Section 2.4.1**, these intragranular deformation structures act as ferrite nucleation sites during DIFT. The proposed model of Zheng et al. did not take into account the ferrite-nucleation sites at these intragranular deformation structures in the prior austenite grain.

Zheng et al. used **Equation 2.7** to calculate the velocity of the ferrite-austenite interface. (However, in their paper they did not mention the values of $\mu_{\alpha\gamma}^0$ and Q .) They included

the effect of deformed austenite on the driving force of austenite to ferrite transformation. For this purpose they modified ΔG_V in **Equation 2.7** to $(\Delta G_V + E_{def})$.

They quantified E_{def} to be approximately 85 J/mol at a temperature of 750°C without giving the level of strain considered for this quantification. The austenite to ferrite driving pressures at the same temperature were 265 J/mol, and 0 J/mol, for C_γ of 0 wt%C, and 0.6 wt%C, respectively [53]. The reduction of the driving force with increasing C_γ can be approximated as linear.

Although a number of details were not reported in the publication of Zheng et al., nevertheless, their study provided the procedure for incorporating various physical parameters in the modelling of DIFT.

2.5.3 Summary

JMAK modelling of the austenite to ferrite transformation is an empirical approach. This can be replaced by physical based models. The application of physical based models through macroscopic length scale approaches are subjected to various assumptions. For example, the austenite-ferrite interface is assumed to be planar or spherical in shape and nucleation site saturation is assumed at the prior austenite grain boundary. To avoid these assumptions mesoscopic length scale modelling can be done, where the evolution of individual ferrite grains can be studied. Experimental austenitic microstructures can be used as an initial microstructure in the mesoscopic models, while in the macroscopic

length scale approach the austenite grains are assumed to be spherical or tetrakaidecahedron in shape.

The macroscopic length scale approaches for modelling the austenite to ferrite transformation are basically ferrite growth models with the assumption of ferrite nucleation site saturation at the prior austenite grain boundary. However, in addition to the ferrite growth model, a nucleation model should be included to describe DIFT. As intragranular nucleation sites are activated during DIFT, a spatial distribution of ferrite nuclei has to be considered for modelling DIFT. Mesoscopic length scale approaches of the austenite to ferrite transformation will be suitable for describing DIFT.

The Monte Carlo model is stochastic in nature. The translation of the Monte Carlo simulation of the austenite to ferrite transformation, into the real time scale is not described in the available literature. In the Cellular Automaton model, the velocity of the ferrite-austenite interface and the position of the interface are tracked separately. This additional calculation burden can be avoided in the phase field model, where the evolution of the phase field parameter contains the location of the ferrite-austenite interface. The advantages of the phase field model over the Cellular Automaton model is described in details by Militzer [89]. Phase field modelling of austenite to ferrite transformation is now well established. This model provides the benefit of an inherent physical based model. The only variations in this model are the different forms of the phase field equation. But those are minor numerical differences only and the basic physics remains the same. However, the Cellular Automaton model does not have an

inherent physical background. It can employ any empirical as well as physical based relationships.

The phase field model will be a suitable growth model to describe austenite to ferrite transformation during DIFT. A ferrite nucleation model can be combined with it to describe the spatial and time distribution of the appearance of ferrite nuclei. Further, a carbon diffusion model can be combined with the phase-field model to implement the principle of mixed-mode modelling.

3. Objectives

The objectives of this work are to propose DIFT processing routes for ultra fine grained dual phase steels suitable for automotive applications and to develop a first generation model to describe DIFT.

The experimental work can be divided into the following sub-objectives. First, a series of systematic DIFT tests were carried out to determine the optimized processing conditions to obtain a ultra fine grained dual phase microstructure in a commercial DP 600 steel and a plain C steel having the same base composition as the DP 600 steel, but with no microalloy addition. For this purpose the effect of the following processing parameters on the final microstructures were quantified: (i) austenitization temperature (or prior austenite grain size), (ii) deformation temperature, (iii) amount of strain, and (iv) post deformation cooling pattern. Secondly, DIFT processing was simulated as an integral part of conventional hot strip mill rolling to evaluate the industrial viability of this novel technique in producing ultra fine grained dual phase microstructure. This simulation was done for the plain C steel through hot torsion.

The objective of the modelling work was to conduct phase field simulations with a variety of nucleation assumptions to obtain insight into microstructure evolution mechanisms during DIFT.

4. Materials and experimental procedure

4.1 Steels investigated

The chemical compositions of the steels used in this study are given in **Table 4.1**. In addition, the Ae_3 temperatures are reported that have been obtained from ThermoCalc using the Fe 2000 data base.

Table 4.1: Chemical composition (in wt%) and Ae_3 temperature of the steels studied

Steel	Mo	Plain C
C	0.06	0.057
Mn	1.9	1.8
Si	0.08	0.085
Nb	0.004	–
Mo	0.16	–
Ti	0.01	0.006
Al	0.04	0.041
N	0.007	0.0064
Ae_3	820°C	821°C

The Mo steel is a commercial grade dual phase steel (DP 600) with a tensile strength of 600 MPa. The steel was supplied by STELCO (now US Steel Canada) in form of a transfer bar material. The plain C steel was laboratory cast and subsequently hot-rolled to 23 mm thick plates at CANMET. The plain C steel has the same base chemistry as the Mo steel, but with no addition of Mo. The present study did a complete investigation of these two chemistries in terms of producing fine grained dual phase steels.

Conventionally, DP 600 steels are either cold rolled annealed (coated) or hot rolled products. The present DP 600 chemistry is typically used for the cold rolled annealed processing route. However, investigations had also been carried with this steel chemistry for hot rolling processing routes [96].

To gain a more comprehensive insight into the role of microalloying additions on DIFT, the two Nb-microalloyed steels that previously had been investigated by Hazra [97] were included in an in-depth EBSD analysis of the fine grained dual phase microstructures. The chemical compositions of these two additional steels are given in **Table 4.2**. They were laboratory cast and subsequently hot-rolled to 23 mm thick plates at CANMET. Starting from the DP 600 steel chemistry the Nb and Mo contents were varied in these steels to study the effect of these two alloying elements on DIFT. The A_{e3} temperatures are essentially the same for all four chemistries. This indicates that changing the microalloying content of Mo and/or Nb has, for the investigated range, little effect on equilibrium transformation temperatures. The procedure to form fine grained dual phase structure in these two chemistries had previously been established by Hazra [97].

Table 4.2: Chemical composition (in wt%) and Ae_3 temperature of the steels initially studied by Hazra

Steel	Nb	Nb+Mo
C	0.06	0.06
Mn	1.8	1.8
Si	0.09	0.09
Nb	0.06	0.045
Mo	–	0.15
Ti	–	–
Al	0.04	0.06
N	0.006	0.006
Ae_3	822°C	823°C

4.2 Experimental equipment

The DIFT tests were done in a Gleeble 3500 thermomechanical simulator. The Gleeble 3500 was selected for this purpose because it gives precise heating and cooling rates, strain, and strain rate at a vacuum of 1.33×10^{-4} Pa or 10^{-6} torr (mmHg). The hot torsion

testing machine Gleeble HS 100 was used for the DIFT experiments with higher strain (>0.6) and to simulate hot strip mill rolling that included a final DIFT pass.

4.3 Experimental methodology

4.3.1 Prior austenite grain sizes

To measure the austenite grain size, and establish suitable reheat conditions small rectangular samples (6mm×15mm×3mm) were heated at a rate of 5°C/s to different austenitization temperatures (950°C, 1000°C, 1050°C, 1100°C, 1150°C, 1200°C) and isothermally held there for 2 minutes. Subsequently, the samples were water quenched to room temperature and the cooling rate obtained was 400°C/s. The samples were then heat treated in a tube furnace at 550°C for 17 h to deposit alloying elements at the grain boundaries and thereby facilitating subsequent metallographic studies. For metallographic observations the samples were cut perpendicular to their length in the plane where the thermocouples had been attached.

Prior austenite grain boundaries in the resulting martensitic microstructure were revealed using the following etchant: 2 g picric acid + 1 mL hydrochloric acid + 1 g dodecylbenzenesulfonic acid + 100 mL distilled water. Etching was done at 65°C by immersing the specimens in this solution for 30 to 600 s.

For prior austenite grain size analysis the optical micrographs were traced. Then the average grain area was measured by Jeffries planimetric procedure as per ASTM E 112-

96 (2004) standard [98]. From this average grain area the average equivalent area diameter (EQAD) of the grains was calculated.

4.3.2 Detection of Ar_3

The Ar_3 temperatures during continuous cooling were determined by dilatometry. For this purpose, tubular samples were used with 20 mm height, 8 mm diameter and 1 mm thickness. The samples were heated to the austenization temperature and held there in the same fashion as were done for the determination of prior austenite grain size. This ensured austenization conditions for which d_γ were known. Subsequently, the samples were cooled at a cooling rate of 40°C/s by passing helium through them. The volumetric changes during the continuous cooling transformation were measured by a crosswise dilatometer located at the temperature measurement cross-section plane. Both of them were located on the midlength of the specimen. The austenite phase transformation was quantified based on the difference between the molar volume of the austenite and the product phase (ferrite/bainite). Austenite is FCC, i.e. a close packed structure, while ferrite/bainite is BCC, with lower packing density. This is the reason for the higher molar volume of ferrite/bainite as compared to austenite. As a result of this change in molar volume, the sample volume increased during phase transformation. This was recorded and presented by dilation response vs. temperature. Applying lever rule, the fraction transformed, $X(T)$, was given by

$$X(T) = \frac{d_m(T) - d_a(T)}{d_p(T) - d_a(T)} \quad (4.1)$$

where $d_m(T)$ is the measured dilation,

$d_a(T) = I_a + S_a T$ is the extrapolated dilation from the austenite region,

$d_p(T) = I_p + S_p T$ is the extrapolated dilation from the product region,

with thermal expansion coefficients S_a and S_p for the austenite and product phases, respectively. The A_{r3} temperatures were determined from $X=0.05$.

4.3.3 Static isothermal ferrite transformation tests

Isothermal ferrite transformation tests were conducted at $A_{r3}+25^\circ\text{C}$. After rapidly cooling from the established austenitizing conditions with a cooling rate of 40°C/s , specimens were held isothermally at the aforementioned temperature for 20 min prior to natural cooling to room temperature. The initiation and completion of austenite decomposition were precisely detected by dilatometry.

4.3.4 DIFT tests

To determine the specimen geometry for DIFT tests cylindrical compression samples and cylindrical tensile samples were investigated. A first set of tests was done to evaluate the thermal response of different geometries by replicating the thermal path of DIFT from literature [2]. This included heating to 900°C at a heating rate of 5°C/s , holding at 900°C for 2 minutes, cooling at a rate of 40°C/s to 770°C and holding there for one minute. The cylindrical compression sample with a 15 mm length and 10 mm diameter had to be

quenched with He to get the required 40°C/s cooling step. It showed initial temperature fluctuation from 760°C to 785°C during isothermal holding at 770°C. This led to the exclusion of this geometry for DIFT studies. Next cylindrical tensile samples with 6 mm and 8 mm gauge diameters were investigated. The length of the cylindrical working zone was 10 mm for both gauge diameters. The 40°C/s cooling rate was achieved naturally (i.e. by air cooling) only in the case of the specimen with 6 mm gauge diameter. Thus, this geometry was selected for DIFT tests. **Figure 4.1** shows the details of the selected specimen geometry. The axis of the DIFT specimens was parallel to the rolling direction of the transfer bar/plate. This sample geometry satisfied the different requirements of these tests that included deformation and rapid cooling. Rapid cooling was the key to establish a high degree of undercooling.

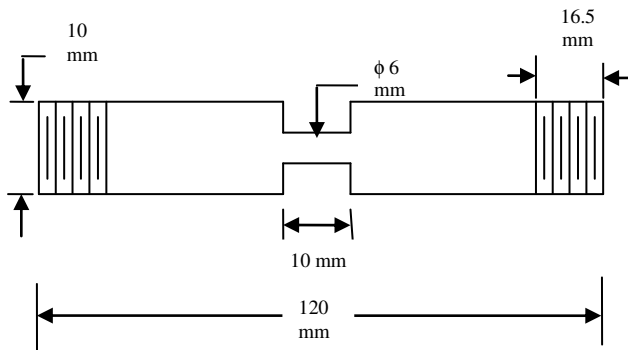


Figure 4.1: Specimen geometry for DIFT tests

However, the selected geometry has certain disadvantages in comparison to the cylindrical compression sample. The cylindrical compression sample provides a state close to the true uniaxial compression. Whereas the selected design has a constrained

geometry and is non-ideal for generating axisymmetric compression. But the cylindrical compression sample was unable to follow the thermal path, which was crucial to achieve DIFT. Rapid cooling was necessary to provide a high degree of undercooling (ΔT^*) before deforming the austenite.

Due to the constrained geometry of the selected sample design, the strain distribution was not uniform along the axis of the sample. In this study, the reported strain values are the diametrical strains. To achieve a relation between the stroke of the piston and the diametral strain a calibration test was done at 700°C.

The thermocouple was spot-welded to the surface of the sample in the middle of the reduced cross section. As the Gleeble operates by resistance heating and there was an increase in resistivity with the increase in temperature for metals the temperature through the cross section of the sample can be assumed to be uniform. But there was a temperature gradient along the axis of the reduced cross section.

The thermomechanical path for the DIFT tests is schematically shown in **Figure 4.2**. The specimens were first austenitized at the established conditions to form a desired austenite grain size. Then they were cooled to the deformation temperature with a cooling rate of 40°C/s, and this was immediately followed by deformation at a strain rate of 1s⁻¹ to a prescribed diametrical strain. The deformation temperatures included in this study were in the range of $A_{r3}+25^{\circ}\text{C}$ to $A_{r3}+50^{\circ}\text{C}$. After deformation the specimens were quenched to room temperature. As the flow of the quenching medium required some time to reach the

sample, there was a delay time between the end of deformation and the start of quench. For He quench this delay was 0.14 s, while for the water quench it was 0.42 s. In general He has been applied as quenching medium, which gave a surface cooling rate of approximately 100°C/s. To evaluate the role of the quench rate, water quench was applied in selected cases. This resulted in an average surface cooling rate of 750°C/s. The surface cooling rates were quantified in between the deformation temperature and 340°C. To estimate the cooling rate in the centre of the sample, the temperature at the centre of the sample was calculated when the surface temperature reaches 340°C. For this purpose heat conduction was considered in an infinitely long cylinder where heat flow occurred only in the radial direction. Further, the surface cooling rate was assumed to be constant between the deformation temperature and 340°C. Based on those considerations a centre temperature of 400°C for He quenching (when the surface temperature was 340°C) and a centre cooling rate of 80°C/s (from the deformation temperature to 400°C) were concluded. For water quenching the centre temperature was 450°C when the surface temperature was 340°C and this gave a centre cooling rate of 330°C/s (from the deformation temperature to 450°C).

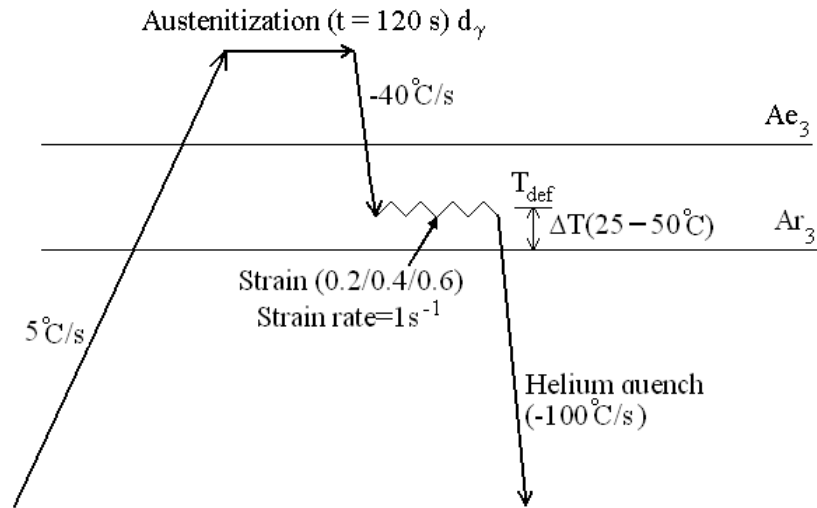


Figure 4.2: The experimental procedure for DIFT tests

There was a variation in strain values of DIFT tests. For example, in the case of the largest deformation although a strain of 0.6 was programmed for the Gleeble tests, the obtained strains ranged between 0.55 to 0.67. The factors responsible for these variations were:

1. The initial stroke was placed manually. It was determined by the instant when the piston touches the sample. This was indicated by the sudden jump in the compression force value. However, as this was determined manually there might be a potential source of error, which can cause variation in the final strain.

2. The thermocouple was spot-welded to the surface of the sample in the midlength of the reduced cross section. As the Gleeble operates by resistance heating and there is an increase in resistivity with increase in temperature for metals, the temperature through the

cross section of the sample can be assumed to be uniform. But there was a temperature gradient along the axis of the reduced cross section. As the positioning of the thermocouple was done manually, it could also act as a potential source of error. Because, if the thermocouple was not in the exact midlength of the reduced cross section, the temperature distribution along the axis of the reduced cross section would not be symmetrical. This could lead to asymmetric deformation along the axis of the reduced cross section and cause variation in the final diametrical strain.

Simulation of DIFT hot rolling schedules were conducted with hot torsion tests. For this purpose a preliminary set of tests were done to replicate the Gleeble tests in the torsion set up. Torsion specimens were machined from the C-Mn plate, with the axis of the torsion specimen parallel to the axis of the rolling direction of the plate. The torsion specimens were 183 mm in length with a diameter of 14.3 mm, and the gauge length of the working zone was 12.7 mm with a diameter of 10mm. During reheating the temperature was monitored with a spot-welded thermocouple. During deformation, however, the temperature was controlled by an optical pyrometer. The post-deformation cooling rate for these tests were approximately 30°C/s.

4.4. Microstructural investigation for tests

The DIFT and continuous cooling transformation (CCT) samples from the Gleeble tests were cut at the welded thermocouple position, along a plane perpendicular to the longitudinal axis. As there was a temperature gradient along the axis of the sample, great

care was taken to determine the exact position of this cut. The cut samples were then mounted and prepared for optical microscopy and secondary electron microscopy (SEM) analysis. The samples were etched with a 2 volume% solution of nitric acid in ethyl alcohol. The ferrite grain sizes were measured from SEM micrographs. The micrographs were traced and the traced images were analyzed with the help of image analyzer software CLEMEX. Based on the measured area of each grain, the equivalent area diameter (EQAD) was determined.

The selected microstructures for all four steels were mapped by EBSD using a FEG (field emission gun)-SEM. The sample preparation for EBSD consisted of standard mechanical polishing to 0.05 μm followed by electropolishing in a 5% perchloric acid and 95% acetic acid solution (by volume) with an applied voltage of 35V. The HKL Channel 5 system was used for data acquisition and analysis. A step size of 0.2 μm was employed for the EBSD maps. The ferrite grain sizes were quantified as equivalent area diameter for both conventional SEM and EBSD images. At least 1000 grains were included in the grain size measurements from conventional SEM images and from EBSD maps employing the minimum critical misorientation angle of 2° . However, for the EBSD maps the number of grains decreased when the critical misorientation angle was increased such that, approximately 500 grains were analyzed when the critical misorientation angle was 10° .

After torsion testing, metallographic observations were made within a position 1 mm below the surface at the centre of the gauge length. The sample preparation for SEM of the torsion tested samples was similar as described for the Gleeble samples.

4.5 Identification of microstructural constituents

Different phases were observed during microstructural observations performed in this study. For example the microstructures obtained from the continuous cooling tests consisted of bainite or a mixture of ferrite and bainite. Whereas, the microstructures obtained from the DIFT tests in the Gleeble, with employed strain of 0.6, consisted of ferrite and martensite. For some of the selected secondary electron micrographs, the microconstituents are labelled to enable rapid identification (F for ferrite, M for martensite, B for bainite, and P for pearlite).

Transmission electron micrographs are necessary to confirm martensite. But an estimate of the second phase product could be obtained from the critical cooling rate equation formulated by Liu et al. [96].

$$\phi_C (^{\circ}C / s) = e^{(a^* + b^* f_{\alpha})} \quad (4.2)$$

where, ϕ_C is the critical cooling rate to obtain martensite, a^* , and b^* are two parameters that depend on the chemistry of the steel, and f_{α} is the ferrite fraction. The values of a^* and b^* for the Mo steel and a C-Mn-Si steel, as determined by Liu et al., are given in **Table 4.3** [96]. In detail the composition of the C-Mn-Si steel was 0.07 wt% C, 1.45 wt% Mn and 0.73 wt% Si [96].

Table 4.3: Parameters describing the critical cooling rates for remaining austenite-to-martensite transformation after ferrite formation [96]

Steel	a^*	b^*
Mo	10.0	-10.6
C-Mn-Si	8.1	-4.4

For the Mo steel the optimized ultra fine microstructure contained a ferrite fraction of 0.86, which required a critical cooling rate of 4°C/s to transform the remaining austenite to martensite. But the applied cooling rate after ferrite formation for the Gleeble DIFT sample was ~80°C/s. This calculation estimate that the second phase obtained in this case was martensite.

The optimized ultra fine microstructure for the plain C steel contained a ferrite fraction of 0.89. To estimate the critical cooling rate to obtain martensite (as the second phase) in this chemistry, the parameter a^* and b^* are assumed to be the same as determined by Liu et al. [96] for the C-Mn-Si steel (see **Table 4.3**). This required a critical cooling rate of 66°C/s to transform the remaining austenite to martensite. As, the applied cooling rate for the Gleeble DIFT was slightly higher than the required cooling rate, a definite conclusion can not be made for this chemistry.

4.6 Mechanical properties

Hollow tensile samples were prepared from torsion tested specimens to conduct mechanical testing [99]. The geometry of the samples is shown in **Figure 4.3**. A hole of 6.35 mm ($\frac{1}{4}$ inch) was drilled in the centre of the torsion samples for this purpose. The wall thickness of the samples was 1.83 mm. The tensile tests were done in a MTS machine with a crosshead speed of 0.025 mm/s equivalent to an initial strain rate of 2×10^{-3} /s.

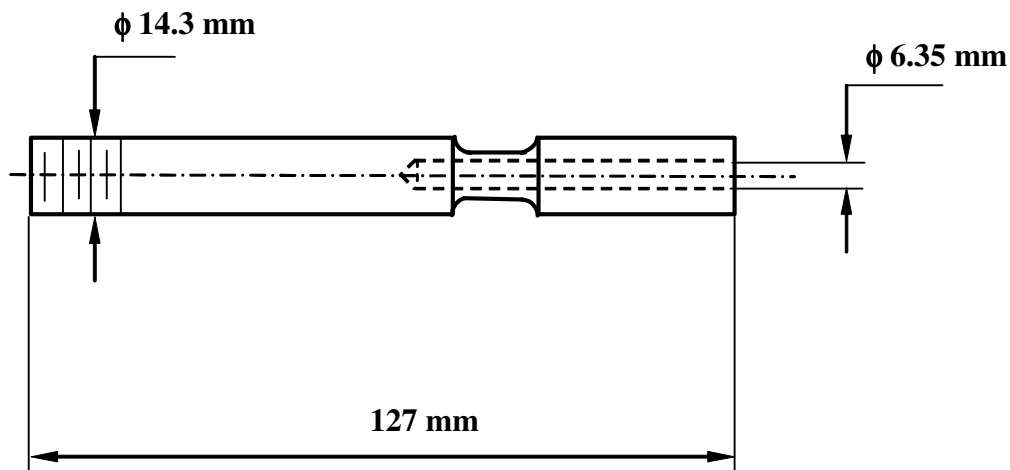


Figure 4.3: Specimen geometry for hollow tensile samples prepared from tested torsion specimen

Unfortunately, the DIFT specimen geometry was unsuitable for performing tensile test. Hence, to obtain an indication of the mechanical properties hardness measurements were carried out for selected microstructures. Hardness measurements were made following the ASTM E 384-99 standard [100]. The microhardness tester (Micromet 3, Buehler Ltd.)

was used with 500 gm load on Vicker's scale with measurements taken in the same cross-sectional plane as the microstructural analysis is performed. A random selection of five measurement fields were made for each specimen.

4.7 Novelty of experimental studies

The present author determined the test matrix to study DIFT as a potential route to produce fine grained dual phase steels. For this purpose the present author developed the specimen geometry. Another researcher, Sujoy Hazra, followed that test matrix and performed the following tests for the Nb and Nb+Mo steels.

(i) Determination of d_γ and corresponding Ar_3 .

(ii) Performing DIFT tests following the test matrix developed by the current author.

(iii) Analyzing the DIFT microstructures by SEM.

The current author did the EBSD analysis of the DIFT microstructures of the Nb containing steels. The current author also evaluated the effect of chemistry on DIFT by analyzing the experimental results of all four steels.

5. Results

5.1 Determination of d_γ and Ar_3

The deformation temperature for DIFT was selected based on the Ar_3 temperature obtained by continuous cooling of the steel sample from a particular austenitization condition. Austenite grain sizes and the corresponding transformation start temperatures for the Nb and Mo containing steels have been determined previously, as listed in **Table 5.1** [9, 97]. The accuracy of the Ar_3 had been determined to be $\pm 6^\circ\text{C}$ [9].

Table 5.1: Transformation data for Mo and Nb chemistries [9, 97]

Steel	$T_\gamma, ^\circ\text{C}$	$d_\gamma, \mu\text{m}$	$Ar_3, ^\circ\text{C}$	$Ae_3-Ar_3, ^\circ\text{C}$
Mo	950	13	670	150
	1050	20	655	165
	1100	27	650	170
Nb	950	11	647	175
	1100	25	504	318
Mo-Nb	950	10	602	221
	1100	26	528	295

A series of isochronal grain growth tests have been done for the plain C steel to quantify the austenite grain sizes at different reheat temperatures (950°C, 1000°C, 1050°C, 1100°C, 1150°C, 1200°C, and 1250°C). The holding time selected was 2 min. The microstructures could not be revealed for the austenitization temperatures of 950°C, 1000°C and 1050°C, presumably because of the fine grain size and lower alloying content as compared to the microalloyed chemistries.

From the rest of the tests, an austenitization temperature of 1200°C was selected for further study because it had a relatively homogeneous grain size of 67µm [Figure 5.1] as compared to other reheating conditions where a more inhomogeneous austenite microstructure was observed indicating abnormal grain growth at these intermediate temperatures. The reheating temperature of 950°C was also selected for further experiments since, based on previous studies for other low-carbon steels, the austenite grain size at that temperature could be expected to be around 15-20 µm [9]. Subsequently, the A_{r3} temperatures for the two reheating conditions selected were determined. The transformation behavior for both austenitization temperatures of 950°C and 1200°C are illustrated in Figure 5.2. The A_{r3} temperature for the T_{γ} of 950°C was 650°C, which was higher than the transformation start temperature of 575°C obtained for T_{γ} of 1200°C. This was consistent with the increase of d_{γ} with T_{γ} . Further, the transformation start temperature determined for T_{γ} of 1200°C indicates the bainite transformation start temperature as a bainitic microstructure was obtained in this continuous cooling test [Figure 5.3].

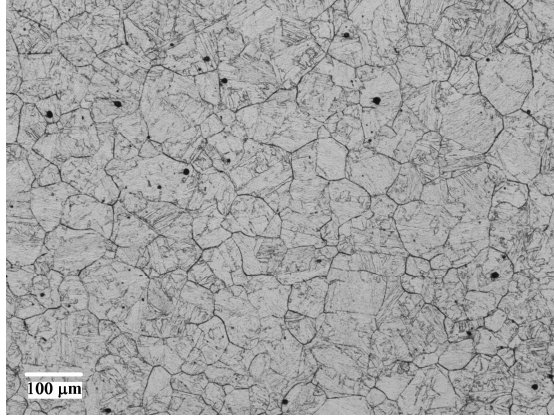


Figure 5.1: Austenite microstructure after reheating to 1200°C, with a holding time of 2 min and water quenching for the plain C steel.

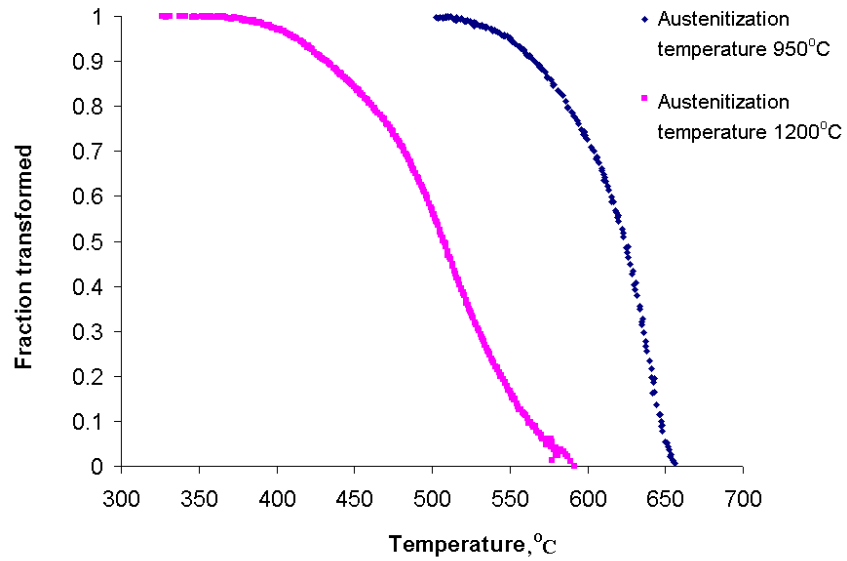


Figure 5.2: Continuous cooling transformation behaviors for plain C steel austenitized at 950°C and 1200°C and then cooled with a cooling rate of 40°C/s.

Figure 5.4 shows the resulting microstructure obtained after continuous cooling transformation of the plain C steel from 950°C. The microstructure consisted of ferrite and bainite. The fraction of ferrite was quantified as 0.63. From the transformation graph shown in **Figure 5.2** the ferrite fraction of 0.63 corresponds to a temperature of 612°C. Thus, this temperature could be estimated to be ferrite formation stop temperature. The transformation data for the plain C steel is summarized in **Table 5.2**.

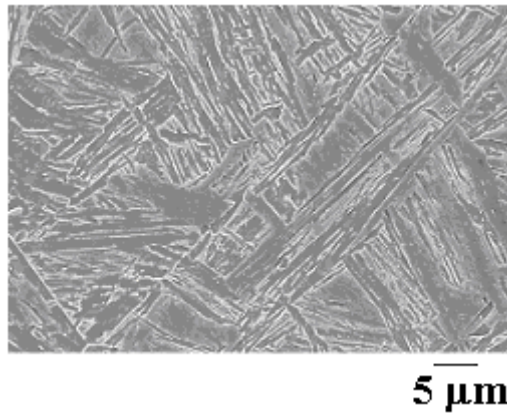


Figure 5.3: Microstructure after continuous cooling test for plain C steel austenitized at 1200°C and cooled with a cooling rate of 40°C/s.

Table 5.2: Transformation data for Plain C chemistry

Steel	T_{γ} , °C	d_{γ} , μm	Ar_3 , °C	Ae_3-Ar_3 , °C
Plain C	950	20*	650	171
	1200	68	575	246

*estimate

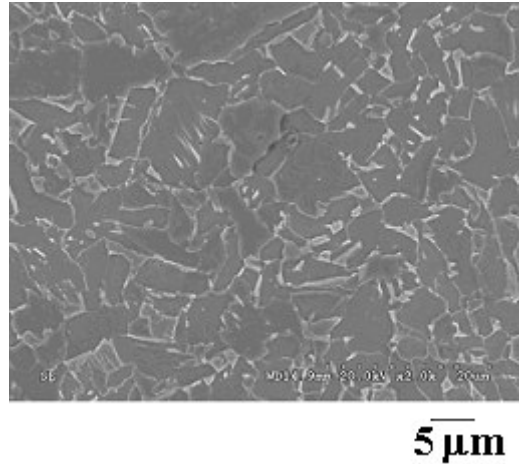


Figure 5.4: Microstructure after continuous cooling test for plain C steel austenitized at 950°C and cooled with a cooling rate of 40°C/s.

For all steels the A_{r3} temperature decreased with increasing initial austenite grain size. Strong effect of Nb was seen in delaying ferrite formation. This effect was more pronounced for larger austenite grain sizes, which were obtained by increasing the reheat temperature from 950 to 1100° C thereby also increasing the amount of Nb in solution. Typically an undercooling of 150-180°C was observed for the A_{r3} temperatures after reheating at 950 °C except for the Mo+Nb steel where this undercooling was in excess of 200°C. For higher reheat temperatures the level of undercooling was increased to 250°C or above in the Nb containing steels and also in the plain carbon steel where reheating at 1200°C resulted in a significantly larger austenite grain size.

5.2 Effect of different processing parameters on DIFT

5.2.1 Overview of DIFT tests performed

Different processing parameters that can affect DIFT are initial austenite grain size, deformation temperature, amount of strain and strain rate. A systematic study was conducted to quantify the effects of these various processing parameters, except for strain rate that is kept at 1 s^{-1} , on DIFT. **Tables 5.3** and **5.4** summarize the tests employed for this purpose in the investigated Mo and plain C steels, respectively.

The maximum strain that could be applied was 0.7. The deformation temperature was varied from 25°C to 50°C above the A_{r3} temperature. A reheating temperature of 1200°C was not selected for the plain C steel as **Figure 5.3** indicates that the transformation product is not in the ferrite formation region. The effects of all the investigated parameters on DIFT are described in detail in **sections 5.2.2 to 5.2.5**.

Table 5.3: DIFT test matrix for Mo steel

Austenitisation temperature and resulting austenite grain size (EQAD)	Deformation temperature= $A_{r3}+\Delta T$ (°C)	Strain
950°C, 13µm	$A_{r3}+25=695$	0.67
	$A_{r3}+50=720$	0.61
1050°C, 20µm	$A_{r3}+30=685$	0.14
	$A_{r3}+30=685$	0.33
	$A_{r3}+30=685$	0.57
	$A_{r3}+45=700$	0.14
	$A_{r3}+45=700$	0.33
	$A_{r3}+45=700$	0.55
	$A_{r3}+50=705$	0.63
1100°C, 27µm	$A_{r3}+50=700$	0.58

Table 5.4: DIFT test matrix for plain C steel (the reheating temperature is 950°C)

Deformation temperature= $Ar_3+\Delta T$, °C	Strain
$Ar_3+25=675$	0.23
	0.47
	0.67
$Ar_3+50=700$	0.22
	0.44
	0.64

5.2.2 Effect of amount of strain on DIFT

For the Mo steel a prior austenite grain size of 20 μm , and deformation temperatures ($Ar_3+50^\circ\text{C}$ and $Ar_3+30^\circ\text{C}$) of 700°C and 685°C were selected to study the effect of strain on DIFT. For the deformation temperature of 700°C the different amounts of strain applied were 0.14, 0.33, 0.55, and 0.63. The final microstructures obtained in these tests are shown in **Figure 5.5 a-d**. From this figure it could be concluded that the volume fraction of ferrite increases with the amount of strain up to a strain of 0.55. For the lowest

amount of strain the microstructure obtained was predominantly bainitic (**Figure 5.5 a**). For strains of 0.55 and higher the ferrite formed was mostly polygonal in shape (**Figure 5.5 c-d**). **Figures 5.5 c and d** show the effect of variation of strain on final microstructure for the highest amount of deformation. A strain of 0.55 produced a d_α of 1.2 μm and a ferrite fraction of 0.76. While the strain of 0.63 resulted in a d_α of 0.9 μm and a ferrite fraction of 0.78. Hence, a strain of 0.55 was needed to get a predominantly ultra fine ferrite (UFF) structure and this could be estimated to be the critical strain to get ultra fine ferrite structure. On increasing the strain beyond the critical strain of DIFT (i.e. 0.55) there was a marginal change in the final microstructure. Another set of tests were done with the same prior austenite grain size but with different deformation temperature ($A_{r3}+30^\circ\text{C}=685^\circ\text{C}$) which confirmed this trend of the effect of strain on DIFT.

For the plain C steel the effect of strain on DIFT is shown in **Figure 5.6 a-c**. In this chemistry the lowest amount of strain resulted in a microstructure which had fine and large grained ferrite along with other transformation products (e.g. bainite and martensite). Increasing the amount of strain increased the amount of fine grained ferrite. From **Figure 5.6** it can be concluded that a strain of 0.67 is needed to get a predominantly ultra fine ferrite structure. Thus, this could be estimated to be the critical strain to get ultra fine ferrite for this chemistry and prior austenite grain size. The fraction of ferrite were 0.64, 0.67 and 0.89 for strains of 0.23, 0.47 and 0.67 respectively. The change in ferrite grain size with strain is reported in **Section 5.7**.

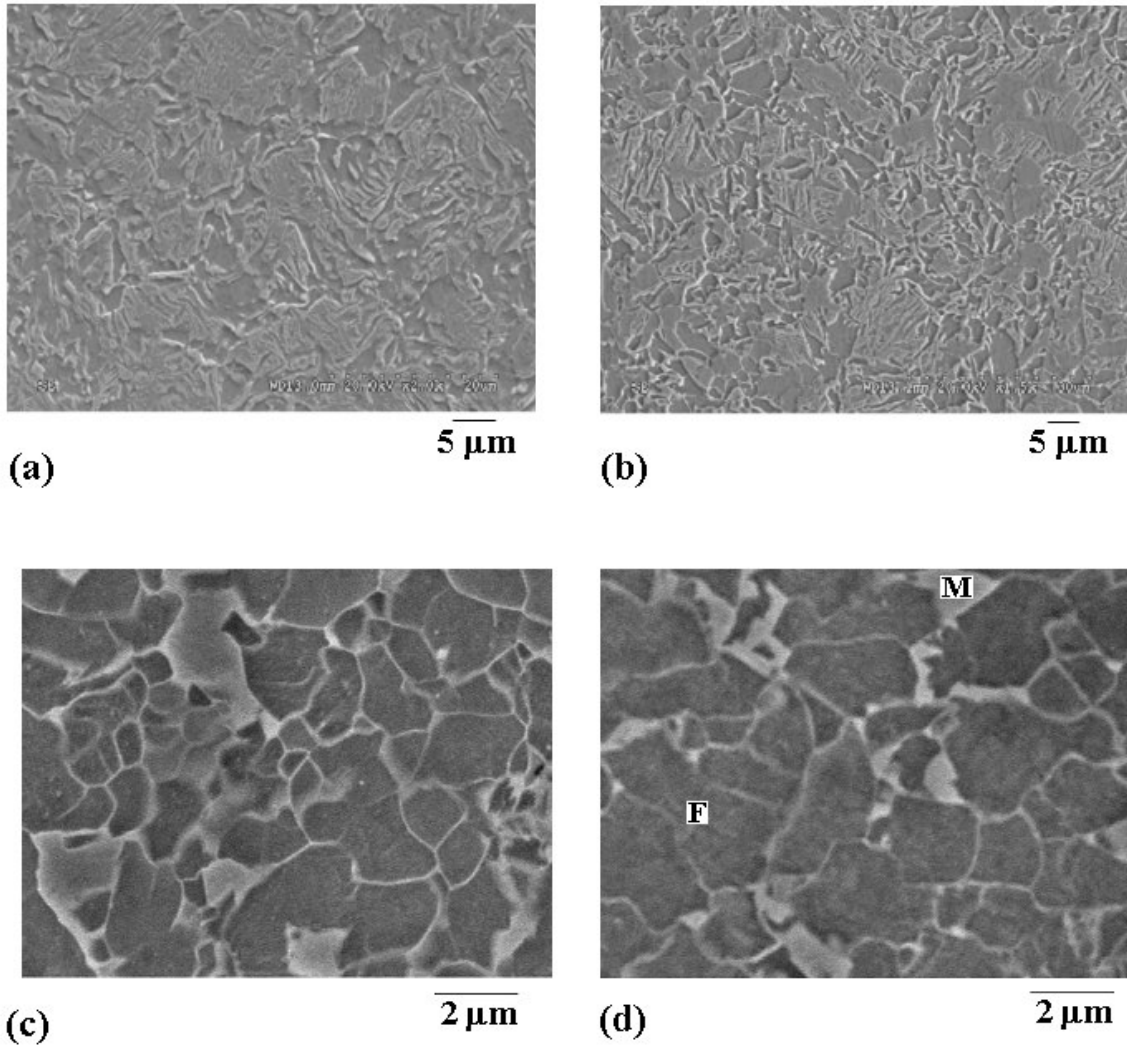


Figure 5.5: Effect of strain on DIFT for Mo steel, for initial austenite grain size $d_{\gamma}=20$ μm , deformation temperature= 700°C , (a) Strain=0.14, (b) Strain=0.33, (c) Strain=0.55, (d) Strain=0.63.

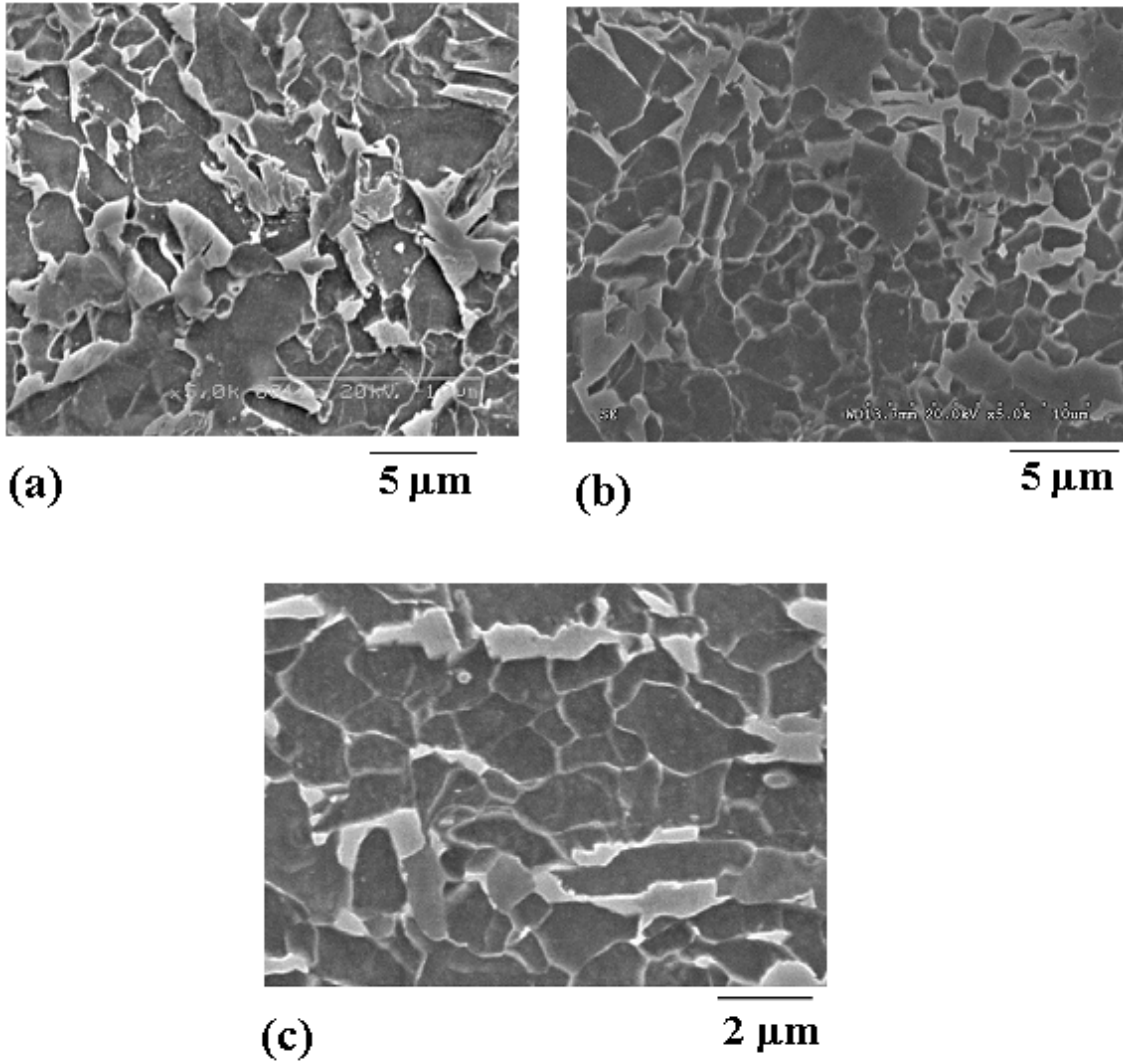


Figure 5.6: Effect of strain on DIFT for plain C steel, for austenitization temperature=950°C, deformation temperature=675°C, (a) Strain=0.23, (b) Strain=0.47, (c) Strain=0.67.

The effect of amount of strain was different for the two chemistries. For the Mo steel increasing the amount of strain converted the microstructure from predominantly bainite to ferrite+martensite. While, for the plain C steel increasing the amount of strain converted a predominantly large grained ferrite microstructure to an ultra fine

ferrite+martensite microstructure. These set of tests were done for selected prior austenite grain sizes. The evaluation of the effect of prior austenite grain size on DIFT is reported in the subsequent section.

5.2.3 Effect of prior austenite grain size on DIFT

The effect of prior austenite grain size on DIFT was quantified for the Mo chemistry. For this purpose the following d_γ 's were considered: 13, 20 and 27 μm . The deformation temperatures were selected to be 50°C above the corresponding A_{r3} temperatures. The deformation temperatures were different in the three cases because the A_{r3} temperatures depend on the prior austenite grain size. But the amount of applied strain was the same ($\epsilon \sim 0.6$). From the final microstructures, it could be concluded that d_γ has little effect on the final microstructure in the range of the parameters studied. All the tests produced a similar average ferrite grain size ($\sim 1 \mu\text{m}$) and ferrite fraction (~ 0.8) (**Figures 5.7 a-c, Table 5.5**).

As discussed in section 5.1 an inclusion of the plain C steel into this comparison on the DIFT potential for an austenite grain size of 25 μm was not possible due to abnormal austenite grain growth. After quantification of the effect of strain and prior austenite grain size on DIFT, the effect of the remaining processing parameter, i.e. the deformation temperature is reported in the following section.

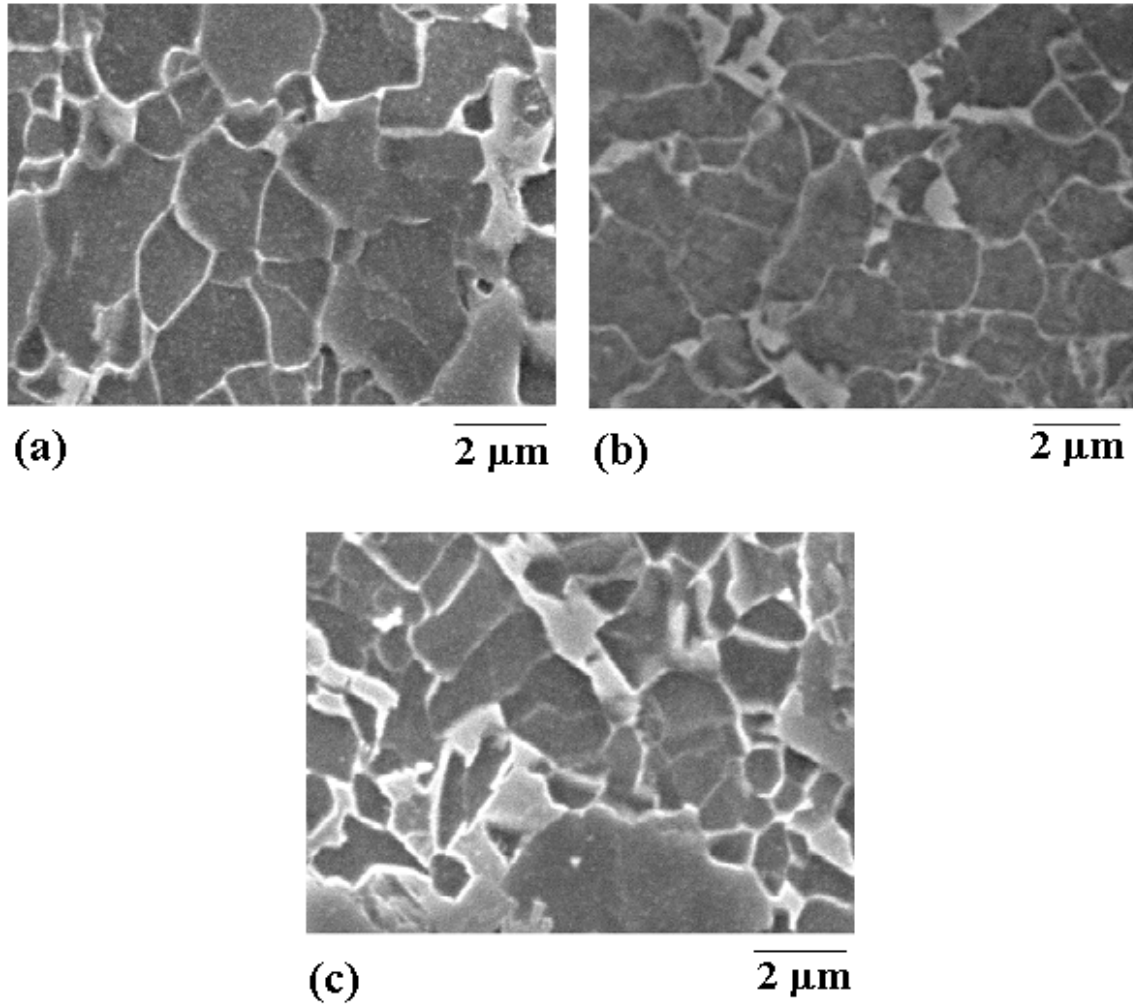


Figure 5.7: Effect of prior austenite grain size on DIFT for Mo steel for $\Delta T=50^{\circ}\text{C}$ (a) Deformation temperature= $Ar_3+\Delta T =670^{\circ}\text{C}+50^{\circ}\text{C}=720^{\circ}\text{C}$, Strain=0.61, initial austenite grain size $d_{\gamma}=13\ \mu\text{m}$, (b) Deformation temperature= $Ar_3+\Delta T =655^{\circ}\text{C}+50^{\circ}\text{C}=705^{\circ}\text{C}$, Strain=0.63, initial austenite grain size $d_{\gamma}=20\ \mu\text{m}$, (c) Deformation temperature= $Ar_3+\Delta T =650^{\circ}\text{C}+50^{\circ}\text{C}=700^{\circ}\text{C}$, Strain=0.6, initial austenite grain size $d_{\gamma}=27\ \mu\text{m}$.

Table 5.5 Summary of effect of d_γ on DIFT for Mo steel

$d_\gamma(\mu\text{m})$	Deformation temperature ($^\circ\text{C}$)	$d_\alpha(\mu\text{m})$	Ferrite fraction
13	720	1.3	0.85
20	705	0.9	0.78
27	700	1.2	0.81

5.2.4 Effect of deformation temperature on DIFT

The effect of deformation temperature on DIFT was studied for two sets of d_γ for the Mo steel: 13 and 20 μm . For d_γ of 13 μm , the deformation temperatures employed were $A_{r_3}+25^\circ\text{C}$ (695°C , **Figure 5.8 a**) and $A_{r_3}+50^\circ\text{C}$ (720°C , **Figure 5.8 b**). The amount of strain was similar in both cases (~ 0.65). In the case of d_γ of 20 μm , the deformation temperatures employed were $A_{r_3}+30^\circ\text{C}$ (685°C , **Figure 5.9 a**) and $A_{r_3}+45^\circ\text{C}$ (700°C , **Figure 5.9 b**). The amount of strain was similar in both cases (~ 0.55). The effect of deformation temperature on DIFT in terms of d_α and ferrite fraction is summarized in **Table 5.6**.

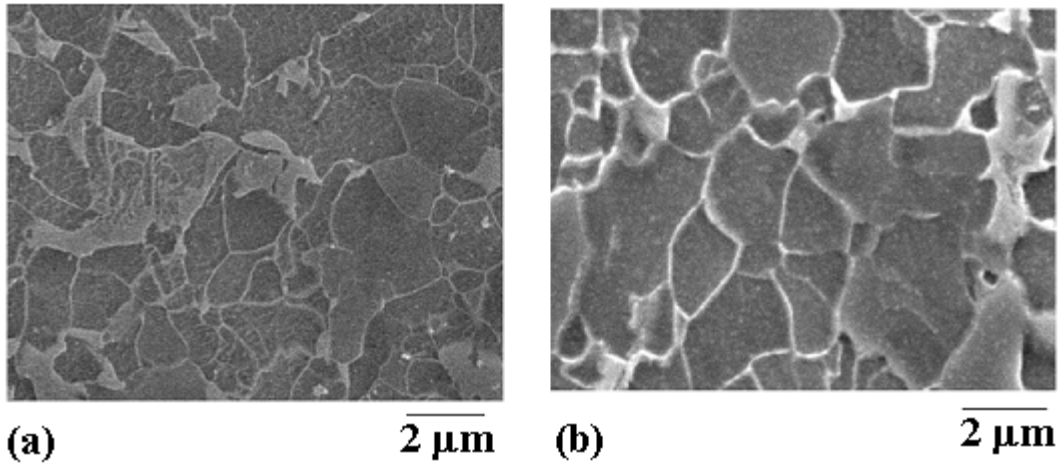


Figure 5.8: Effect of deformation temperature on DIFT for Mo steel, for initial austenite grain size $d_\gamma=13 \mu\text{m}$ (a) Strain=0.67, deformation temperature= $670^\circ\text{C}+25^\circ\text{C}=695^\circ\text{C}$, (b) Strain=0.61, deformation temperature= $670^\circ\text{C}+50^\circ\text{C}=720^\circ\text{C}$.

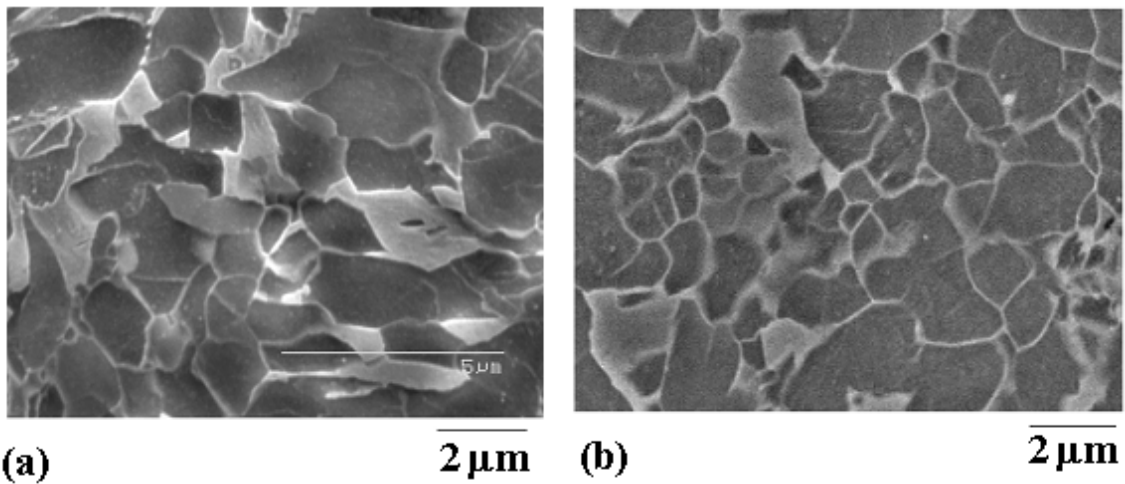


Figure 5.9: Effect of deformation temperature on DIFT for Mo steel, for initial austenite grain size $d_\gamma=20 \mu\text{m}$ (a) Strain=0.57, deformation temperature= $655^\circ\text{C}+30^\circ\text{C}=685^\circ\text{C}$, (b) Strain=0.55, deformation temperature= $655^\circ\text{C}+45^\circ\text{C}=700^\circ\text{C}$.

Table 5.6 Effect of deformation temperature on DIFT for Mo steel

d_γ , μm	Strain	Deformation temperature, $^\circ\text{C}$	d_α , μm	Ferrite fraction
13	0.67	695	1.3	0.86
	0.61	720	1.3	0.85
20	0.57	685	1.3	0.84
	0.55	700	1.2	0.76

From **Table 5.6** it can be concluded that in the case of the finest d_γ there was no effect of deformation temperature on final microstructure. A d_γ of 13 μm produced d_α of 1.3 μm with a ferrite fraction of approximately 0.85 for both deformation temperatures. However, for the larger d_γ of 20 μm the final ferrite fraction increased from 0.76 to 0.84 with decrease in deformation temperature from 700 $^\circ\text{C}$ to 685 $^\circ\text{C}$. But in both cases the ferrite grain size was 1.3 μm . Hence, the effect of deformation temperature on d_α was insignificant in the studied ranges of d_γ and deformation temperatures.

For the plain C steel an austenitization temperature of 950 $^\circ\text{C}$ was employed to study the effect of deformation temperature on DIFT. The deformation temperatures applied were $A_{r3}+25^\circ\text{C}$ (675 $^\circ\text{C}$, **Figure 5.10 a**) and $A_{r3}+50^\circ\text{C}$ (700 $^\circ\text{C}$, **Figure 5.10 b**). The amount of strain was similar in both cases (~0.65). From **Figure 5.10** it can be concluded that increasing the deformation temperature from 675 $^\circ\text{C}$ to 700 $^\circ\text{C}$ reduced the ferrite fraction from 0.89 to 0.76. However, d_α was unchanged (approximately 1.3 μm) with this increase in the deformation temperature. Hence, deformation temperature affected the final microstructure of the plain C steel in the same way as in the case of the Mo steel with

larger d_{γ} i.e. there was no effect of deformation temperature on d_{α} , but the final ferrite fraction increased with the decrease in the deformation temperature.

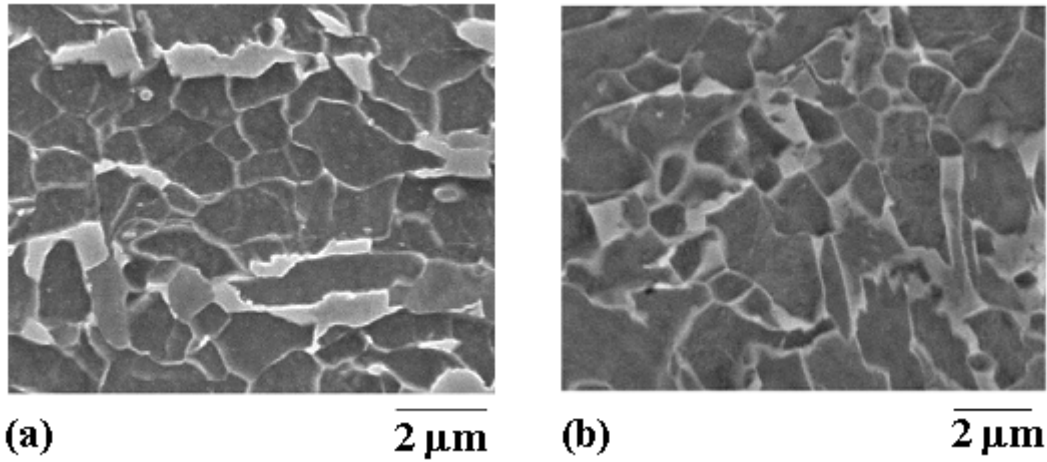


Figure 5.10: Effect of deformation temperature on DIFT for plain C steel, for austenitization temperature=950°C, (a) Strain=0.67, deformation temperature=650°C+25°C=675°C, (b) Strain=0.64, deformation temperature=650°C+50°C=700°C.

After analyzing the effects of different processing parameters on DIFT, the following section is focussed on summarizing the conditions to obtain a predominantly ultra fine ferrite dual phase structure. The detailed analyses of the optimized microstructures are also reported along with.

5.3 Predominantly ultrafine ferrite microstructure

5.3.1 Conditions to obtain predominantly ultrafine ferrite microstructure

From **Figures 5.5 d** and **5.6 c** it is seen that a sufficient amount of strain (>0.55) is required to form a dual phase microstructure with a ferrite fraction of 0.8 or higher as desired in automotive steels. Higher undercooling and finer initial austenite grain size is beneficial to obtain the target ferrite fraction of 0.85. The experimental conditions where a predominantly ultrafine ferrite microstructure was obtained are reported in **Tables 5.7** and **5.8**, for Mo and plain C steels, respectively. In the case of the Mo steel, a ferrite fraction of 0.8 or higher was obtained for all investigated austenite grain sizes. In addition, for the Mo steel with the finest d_γ of 13 μm , there was no effect of the deformation temperature on the final microstructure. However, for the plain C steel austenitized at 950°C the ferrite fraction decreased by 0.13 when the deformation temperature increased from 675°C to 700°C.

As mentioned in **Chapter 1** this study was a part of a larger project dealing with ultra fine grained dual phase steels in four chemistries. The present study examined the optimized microstructure for all four chemistries by advanced EBSD technique. The experimental conditions to obtain optimized ultra fine ferrite dual phase structure for the Nb and Mo-Nb containing steels was previously determined as listed in **Table 5.9 [97]**. However, in none of the cases, a ferrite fraction of 0.8 were obtained for these steels.

Hence, in **Table 5.9** those conditions are reported, where the ferrite fraction obtained was 0.7 or higher.

Table 5.7: Test conditions where a predominantly ferrite microstructure has been obtained for Mo steel

Test No.	d_γ , μm	Deformation temperature, °C	Strain	d_α , μm	Standard deviation *	Ferrite fraction
1.	20	$Ar_3+30=685$	0.57	1.3	0.56	0.84
2.	20	$Ar_3+50=705$	0.63	0.9	0.66	0.78
3.	13	$Ar_3+25=695$	0.67	1.3	0.61	0.86
4.	13	$Ar_3+50=720$	0.61	1.3	0.60	0.85
5.	27	$Ar_3+50=700$	0.58	1.2	0.65	0.81

(* standard deviation is determined from log-normal fit of ferrite grain size distribution)

Table 5.8: Test conditions where a predominantly ferrite microstructure has been obtained for plain C steel

Test No.	Austenitization temperature, °C	Deformation temperature, °C	Strain	d_α , μm	Standard deviation *	Ferrite fraction
1.	950	$Ar_3+25=675$	0.67	1.3	0.59	0.89
2.	950	$Ar_3+50=700$	0.64	1.4	0.65	0.76

(* standard deviation is determined from log-normal fit of ferrite grain size distribution)

Table 5.9: Test conditions where a predominantly ferrite microstructure has been obtained for Nb and Mo-Nb steels [97]

Chemistry	Austenitization temperature, °C and d_γ , μm	Deformation temperature, °C	Strain	Strain rate, s^{-1}	d_α , μm	Standard deviation*	Ferrite fraction
Nb	950 and 11	$A_{r_3+25}=672$	0.6	1	1.3	0.56	0.75
Mo-Nb	950 and 10	$A_{r_3+50}=627$	0.6	1	1.0	0.50	0.70

(* standard deviation is determined from log-normal fit of ferrite grain size distribution)

5.3.2 Grain size distribution

The grain size distributions are log normal in all cases. The frequency $f(x)$ of grains with a diameter x is then given by:

$$f(x) = \frac{1}{x\sigma\sqrt{2\pi}} \exp\left(\frac{-\{\ln(x/x_p)\}^2}{2\sigma^2}\right) \quad (5.1)$$

Here σ is the standard deviation and x_p is the median grain size.

As summarized in **Tables 5.7-5.8**, the distributions were very similar in all cases with median ferrite grain sizes being approximately 1 μm and σ -values were 0.6 ± 0.1 as measured for the conventional SEM micrographs. As an example, the ferrite grain size distribution for the Mo steel austenitized at 950°C ($d_\gamma=13 \mu\text{m}$) and deformed at 695°C ($A_{r_3+25}^\circ\text{C}$) is plotted in **Figure 5.11**. The bar chart in the figure shows the measured size distribution, while the line represents the log-normal fit of the measured distribution.

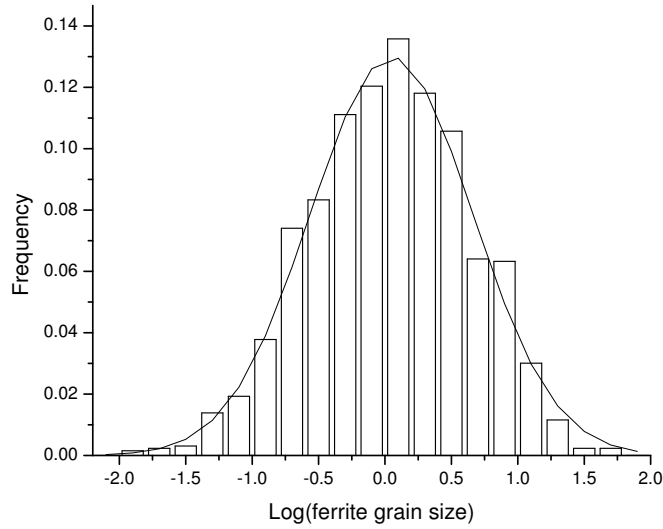


Figure 5.11: Grain size distribution for Mo steel as measured ($d_{\gamma}=13 \mu\text{m}$, $T_{def}=695^{\circ}\text{C}$, $\varepsilon=0.65$) and as-fitted log-normal distribution (solid line).

5.3.3 EBSD micrographs

The optimized microstructures (with the smallest prior austenite grain size, highest amount of strain and $\Delta T=25^{\circ}\text{C}$) for all four compositions were mapped by EBSD. **Figure 5.12a-d** shows the orientation maps for all four steels. The colours indicate the crystal direction parallel to the compression direction of the samples. The high angle boundaries with a misorientation of 10° or more, and low angle boundaries with a misorientation of 2° - 10° are indicated by thick and thin black lines, respectively; 2° was taken as the lower limit of measurable grain boundary misorientation angles. The scheme for obtaining the EBSD maps shown in **Figure 5.12a-d** from the as-measured raw data is described in the

Appendix 2 where detail is also provided for the procedures to identify different phases and to obtain the ferrite grain size from the EBSD data.

The ferrite grain sizes obtained from EBSD studies are compared in **Table 5.10** with those obtained from the conventional SEM studies. It could be seen that the ferrite grain sizes determined by EBSD analysis, using a critical misorientation angle of 2° to define grains, were similar to those determined by conventional SEM studies. The discrepancy of ferrite grain size obtained by EBSD analysis with a critical misorientation angle of 2° and that obtained by SEM studies was greatest in case of the Nb steel. Interestingly, for the Nb steel the EBSD grain sizes were virtually independent whether a misorientation angle of 2 or 10° was employed to identify grains whereas for the other steels a substantial increase of the apparent grain size from $1.3\text{-}1.5\ \mu\text{m}$ to $1.9\text{-}2.1\ \mu\text{m}$ was recorded when the critical misorientation was raised to 10° that is characteristic for the high angle boundaries.

The accuracy of grain size measurements using EBSD is limited by the step size employed, here $\pm 0.2\ \mu\text{m}$, but the grain size itself becomes a function of the critical misorientation angle. In the present case, the situation is further complicated by the presence of the two phases, ferrite and martensite, that cannot be clearly separated by EBSD measurements. Using the pattern quality, a threshold level can be introduced to separate ferrite grains from martensite islands. However, pattern quality depends also on detail of specimen preparation such that in the present investigations phase fraction measurements using conventional SEM were used to determine the threshold level for each individual sample. The accuracy of measuring the ferrite fraction by SEM was

estimated to be ± 0.05 . These identification procedures for ferrite grains lead to an additional error in making grain size measurements. With conventional SEM, it appears that also low angle boundaries were visible and thus this grain size measurement does not clearly separate between low and high angle boundaries, which on the other hand, can be achieved by EBSD. Thus, the conventional SEM analysis provides a lower bound for the actual mean grain size. The current status of quantifying these and similar fine-grained dual-phase microstructures suggests using a combination of conventional SEM to measure phase fractions with EBSD to measure grain sizes and misorientation angle distributions.

The distribution of grain boundary misorientation angles that are shown in **Figure 5.13** for the four EBSD maps. These distributions confirm that the Nb steel has a higher proportion of high angle grain boundaries (grain boundaries with a misorientation angle of 10° or more) as compared to the other steels. It can be seen from **Figure 5.13** that in the Nb steel just 15% of the grain boundaries were low angle boundaries with misorientations below 10° whereas in all other steels, 40-45% of the grain boundaries had misorientation angles between 2 to 10° . This is consistent with the observation of clusters of ferrite grains with low angle boundaries between themselves for the Mo, plain C and Mo-Nb steels. A typical example of this kind of cluster of ferrite grains is shown in **Figure 5.12(a)**. However, such grain clusters were not observed in the Nb steel.

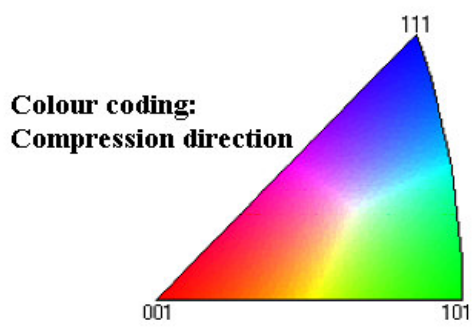
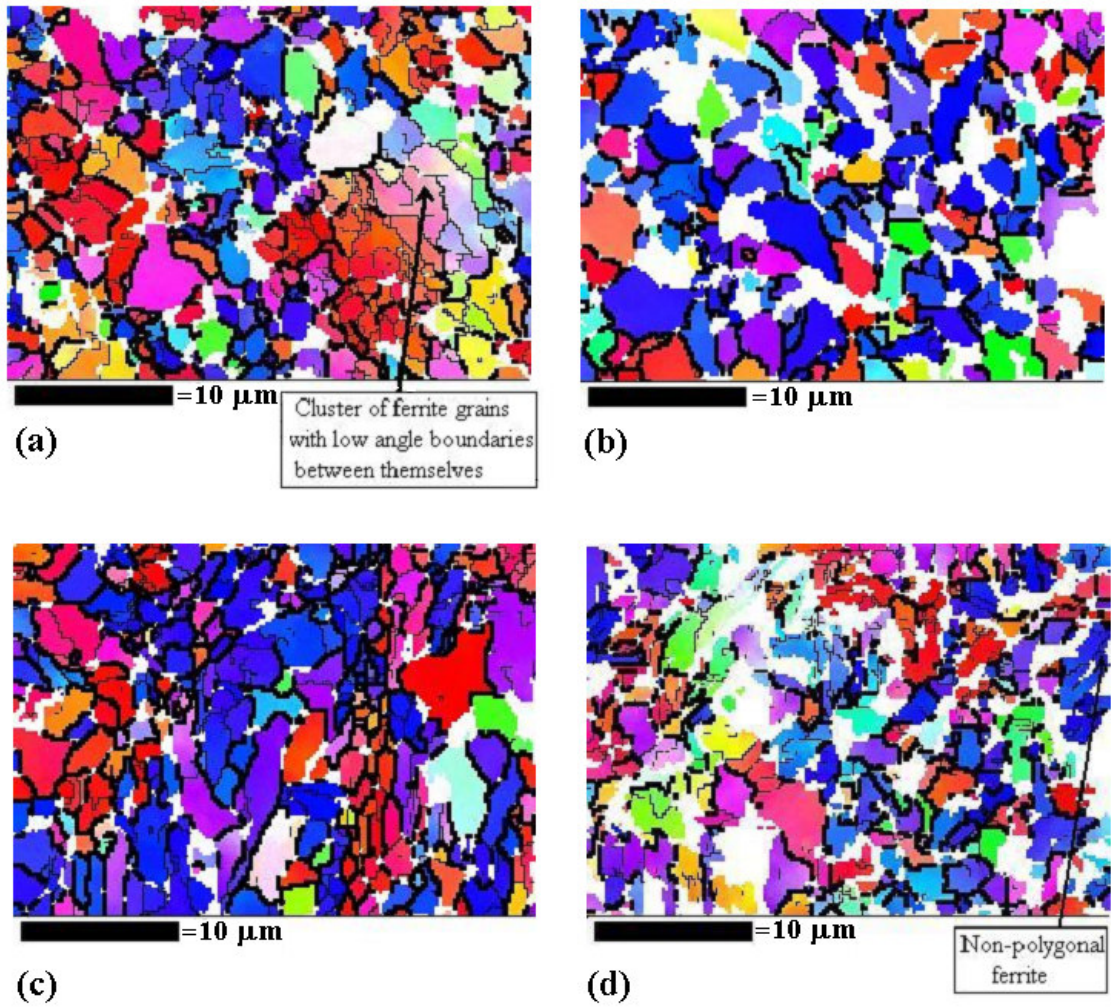


Figure 5.12: EBSD maps for optimized conditions for all steels (a) Mo steel, (b) Nb steel, (c) Plain C steel, (d) Mo-Nb steel.

Table 5.10: Mean ferrite grain sizes obtained from EBSD and conventional SEM for optimized cases

Steels	$d_{\alpha}, \mu\text{m}$ EBSD, (Critical misorientation angle=2°)	$d_{\alpha}, \mu\text{m}$ EBSD, (Critical misorientation angle=10°)	$d_{\alpha}, \mu\text{m}$ Conventional SEM
Mo	1.3	1.9	1.3
Plain C	1.5	2.1	1.3
Nb	1.8	1.9	1.3
Mo-Nb	1.3	1.9	1.0

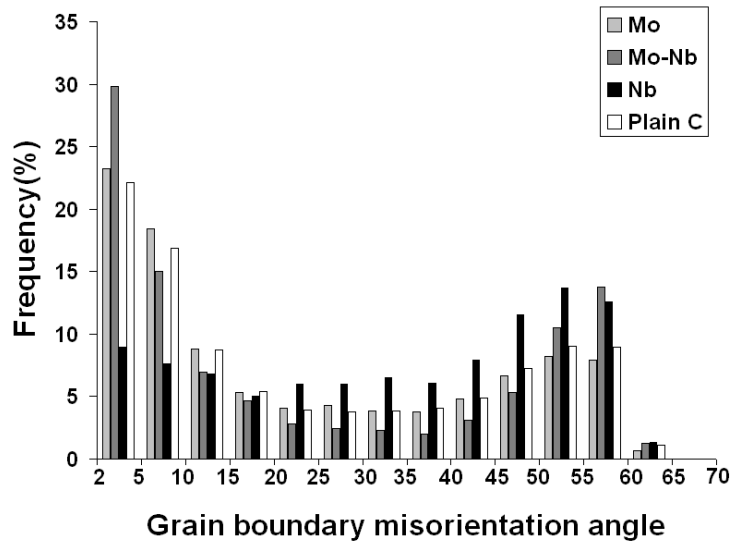


Figure 5.13: Distribution of grain boundary misorientation angle for all four chemistries for optimized conditions.

5.3.4 Mechanical properties

The DIFT specimen geometry was not suitable to perform standard tensile tests. Thus, hardness measurements were carried out to obtain an indication of the mechanical properties for the optimized microstructures. **Table 5.11** summarizes all the hardness data and the predicted flow stress at 8% strain ($\sigma_{0.08}$) estimated by Tabor's relation from hardness data [101], i.e.

$$H_V = 3\sigma_{0.08}$$

where H_V is the Vicker's hardness number.

Table 5.11: Summary of hardness measurements

Steels	H_V (kg/mm ²)	H_V (MPa)	Predicted $\sigma_{0.08}$ (MPa)
Mo	204±3	2001±30	667±10
Plain C	206±3	2021±30	674±10

After optimizing the processing parameters to obtain an ultra fine dual phase microstructure, further tests were done to evaluate the effect of the post deformation thermal treatment on the microstructure.

5.4 Post deformation treatments

5.4.1 Role of post deformation cooling rate

The Mo steel was selected to study the effect of post deformation cooling rate. Post deformation cooling rate was increased to enhance the martensite formation after DIFT. The time gap between the end of deformation and the start of quench were 0.14 and 0.42 seconds for He and water quench, respectively. The fraction of martensite was increased from 0.14 for He quenching (post deformation cooling rate of 80°C/s) to 0.28 for water quenching (post deformation cooling rate of 330°C/s) with an insignificant change in ferrite grain size (the cooling rates reported were predicted centre cooling rates in the deformed sample, as described in Experimental procedure, see **Section 4.3.4**). This indicated that some ferrite was formed during cooling (or post-deformation holding). **Figure 5.14** shows the microstructure after water quenching illustrating the increased martensite fraction.

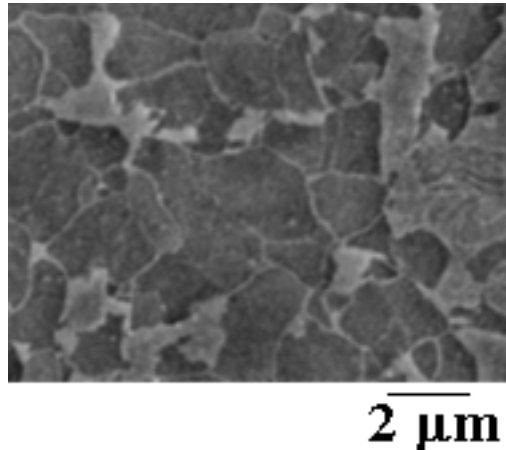


Figure 5.14: DIFT microstructure obtained for the Mo steel after reheating at 950°C, deforming 25°C above A_{r3} and subsequently water quenching.

For the Mo steel, a post deformation cooling rate of 100°C/s appeared to be adequate to form a desirable ultra fine dual phase microstructure with a martensite fraction of approximately 0.15. However, further studies are required to establish in more detail the post deformation cooling conditions for desired ferrite-martensite dual-phase structures.

5.4.2 Role of post deformation isothermal hold

To check the stability of the DIFT ferrite grains against grain growth, a plain C steel sample was isothermally held at deformation temperature for 5 s after completion of deformation step. The 5 s time was selected, as this is the typical time the steel spends after deformation in the hot rolling mill and prior to entering the run out table. The smallest prior austenite grain size was employed for this purpose and after the isothermal holding the sample was He quenched. The micrograph obtained is shown in **Figure 5.15**.

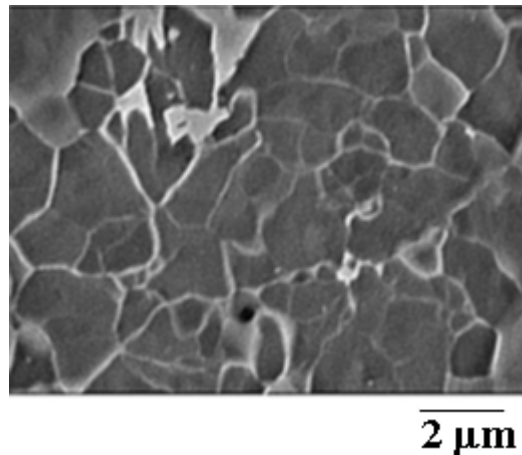


Figure 5.15: Micrograph resulting from DIFT test employing a strain of 0.72 and post deformation isothermal holding of 5 s at 675°C for the plain C steel reheated at 950°C.

The average ferrite grain size obtained was 1.1 μm and the ferrite fraction was 0.83. This was similar to the DIFT test with no isothermal hold after deformation, where an average ferrite grain size of 1.3 μm and a ferrite fraction of 0.89 were obtained. Hence, the ferrite grains obtained by DIFT were stable against grain growth for the time period studied.

This concludes the experimental work to obtain an ultra fine dual phase microstructure. The following section is attributed to a qualitative description of the ferrite grain refinement by DIFT.

5.5 Ferrite grain refinement by DIFT

To have a qualitative idea about the extent of ferrite grain refinement by DIFT the microstructure obtained by a DIFT test at $A_{r_3}+25^\circ\text{C}$, which included a post deformation holding time given by the isothermal 95% transformation time at $A_{r_3}+25^\circ\text{C}$ minus the time spent to deform the sample, was compared with a test with the same thermal path but no deformation employed.

Static isothermal holding experiments were done to determine the transformation kinetics for both chemistries at $A_{r_3}+25^\circ\text{C}$. The finest austenite grain sizes were employed in this study. The fraction transformed-time graph for the Mo steel held at 695°C is shown in **Figure 5.16**. The time scale for **Figure 5.16** was determined based on the start of the isothermal holding, i.e. the time was set to zero when the holding temperature was reached. The start of isothermal holding was selected at the instant after which the

temperature fluctuation from the holding temperature was within $\pm 2^\circ\text{C}$. The 95% transformation time was determined to be 6 min 8 s. For the plain C steel the 95% transformation time was 3 min 17 s. From these tests it could be concluded that the transformation rate is slower in the Mo steel as a result of the solute drag due to the presence of Mo in solid solution.

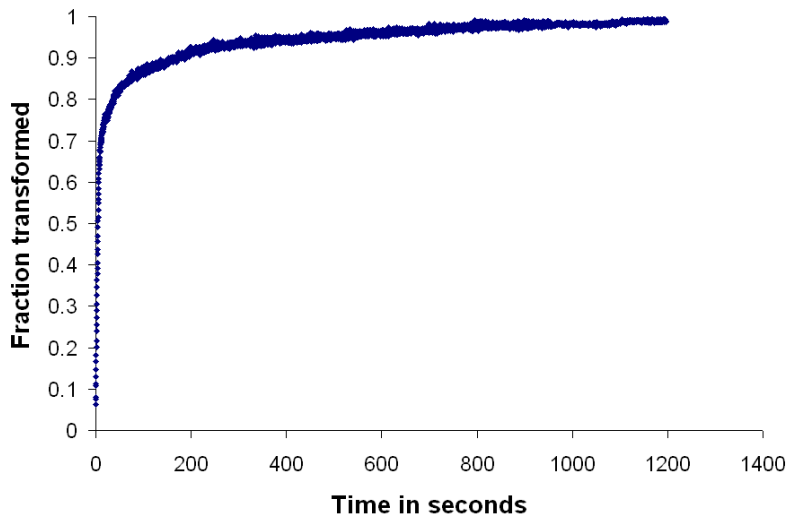
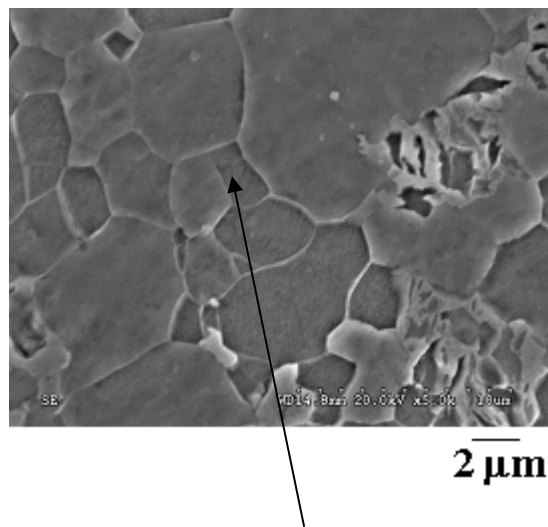


Figure 5.16: Fraction transformed-time graph for Mo steel (isothermally held at 695°C)

After obtaining the values of 95% transformation time at $A_{r3}+25^\circ\text{C}$, subsequent tests were performed where the samples were held isothermally after deformation. After the deformation+isothermal holding the samples were He quenched. The test matrix employed for these tests is shown in **Table 5.12** alongwith the quantification of the obtained final microstructures. The micrographs obtained are shown in **Figures 5.17-5.18** for Mo and plain C steels, respectively.

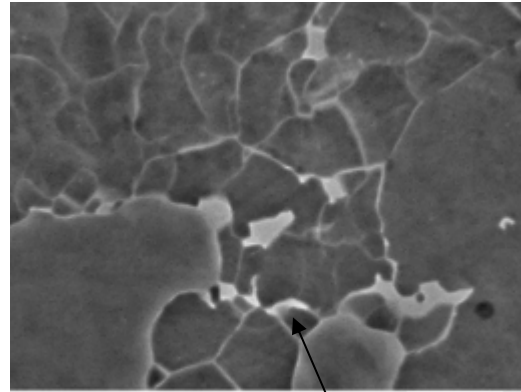
Table 5.12: Summary of post-deformation isothermal holding tests

Steel	Strain	Deformation and isothermal holding temperature, °C	Isothermal holding time	d_{α_s} μm	Ferrite fraction
Mo	0.78	695	6 min 8 s	2.8	0.68
Plain C	0.74	675	3 min 17 s	1.8	0.8



2 μm sized grains

Figure 5.17: Micrograph after DIFT test with $d_{\gamma}=13 \mu\text{m}$ employing a strain of 0.78 and post deformation isothermal holding of 6 min 8 s at 695°C for the Mo steel.

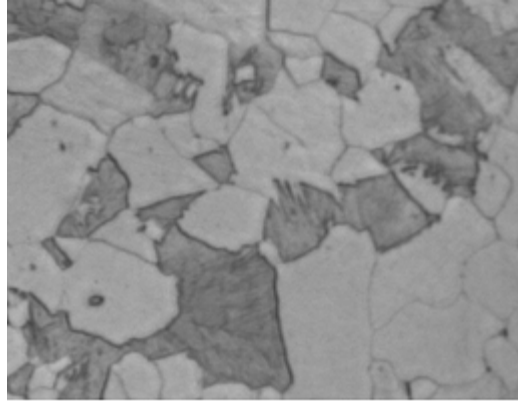


2 μm

1 μm sized grains

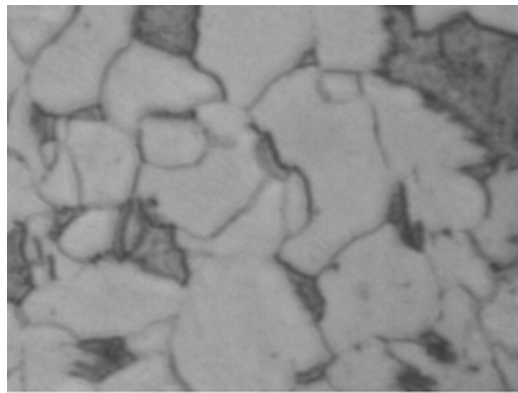
Figure 5.18: Micrograph after DIFT test employing a strain of 0.74 and post deformation isothermal holding of 3 min 17 s at 675°C for the plain C steel reheated at 950°C.

The microstructures obtained for the tests where no deformation was employed are shown in **Figures 5.19** and **5.20**, for Mo and plain C steels, respectively. The quantification of the microstructures is summarized in **Table 5.13**. Comparing the microstructures obtained from the static isothermal holding tests (holding time=95% of transformation time) with those obtained from DIFT+isothermal holding tests (**Figure 5.17** vs. **5.19** for Mo steel and **Figure 5.18** vs. **5.20** for plain C steel) it could be concluded that the fine ferrite grains seen in **Figures 5.17** and **5.18** were formed by DIFT.



5 μm

Figure 5.19: Microstructure after isothermal holding at 695°C for 6 min 8 s and subsequent He quenching for Mo steel with austenite grain size of 13 μm .



5 μm

Figure 5.20: Microstructure after isothermal holding at 675°C for 3 min 17 s and subsequent He quenching for plain C steel with austenitization temperature of 950°C.

Table 5.13: Summary of static isothermal holding tests (holding time is 95% of transformation time)

Steel	Isothermal holding temperature, °C	Isothermal holding time	d_{α} , μm	Ferrite fraction
Mo	695	6 min 8 s	6.1	0.73
Plain C	675	3 min 17 s	5.6	0.79

After completing the study to obtain ultra fine dual phase microstructure, it was evaluated whether this technique could be combined with the hot rolling process.

5.6 Torsion simulation of DIFT

5.6.1 Replication of Gleeble tests

From the Gleeble, tests plain C steel was found to be at par with the Mo steel in terms of grain refinement capacity. Regarding automotive applications, plain C steel is preferred over the Mo steel because of lower alloying cost and better weldability. Thus, the plain C chemistry was selected for industrial simulation of DIFT by performing hot torsion tests with the Gleeble HTS 100 machine. First, a set of pretests were done to replicate the thermomechanical path of the Gleeble 3500 tests that resulted in the optimized

microstructure for the plain C steel. As deformation in torsion was less efficient in forming ultra fine ferrite structure by DIFT in comparison to rolling and axisymmetric compression, a significantly higher amount of deformation was applied to produce an ultra-fine ferrite microstructure by DIFT in hot torsion [8]. The test matrix utilized for this purpose is summarized in **Table 5.14**. The effect of deformation temperature on final microstructure was also studied. For this set of tests the torsion samples were austenitized at 950°C and held there for 2 min. Then they were cooled at a rate of 40°C/s to the deformation temperature. Although the torsion samples have a different geometry than the Gleeble samples the cooling rate of 40°C/s from austenitization temperature to the deformation temperature may also be achieved in torsion tests by proper He cooling arrangement.

Table 5.14: Replication of Gleeble tests in torsion mode

Deformation temperature, °C	Strain
675	0.6
	1.5
	3.0
700	1.5

5.6.2 Effect of strain on DIFT

The torsion samples were subjected to different amount of strains, i.e. 0.6, 1.5 and 3.0 at 675°C. The microstructures obtained are shown in **Figure 5.21 a-c**. The quantification of the microstructures is summarized in **Table 5.15**. Increasing the amount of equivalent strain from 0.6 to 1.5 increased the fraction of finer ferrite grains, which is similar to the effect of increasing strain on the fraction of finer ferrite grains for the Gleeble 3500 tests. An equivalent strain of 1.5 produced a suitable ultra fine ferrite microstructure and increasing the equivalent strain to 3.0 did not further refine the microstructure. In both cases the ultra fine ferrite fraction was more than 0.8 and the ferrite grain size was ~1.7 μm , i.e. slightly larger than that of 1.3 μm , observed for the axisymmetric compression test.

Table 5.15: Summary of effect of strain on torsion replication of optimized (in terms of final microstructure) DIFT Gleeble tests, chemistry: plain C steel

Deformation temperature	Strain	Ferrite fraction	d_{α} , μm
675°C	0.6	0.91	1.9
	1.5	0.81	1.7
	3.0	0.85	1.6

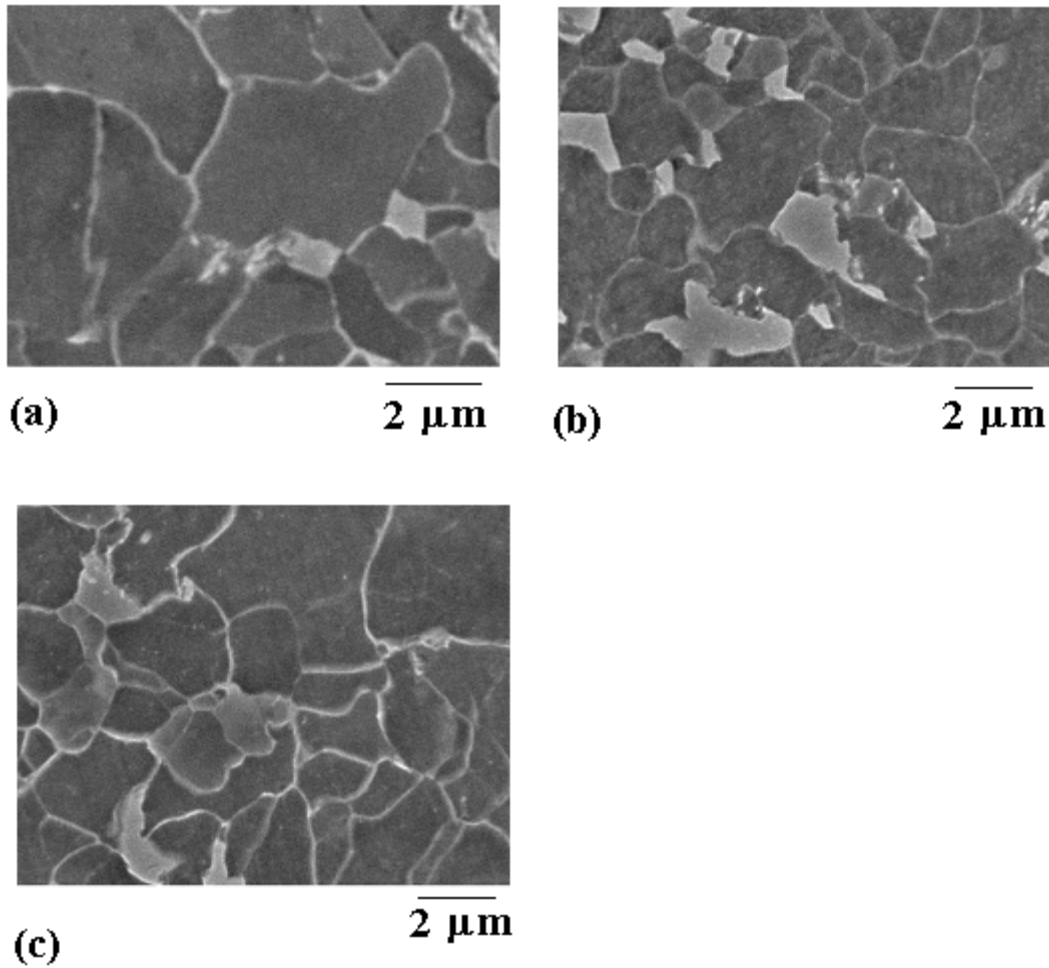


Figure 5.21: Microstructure obtained from torsion replication of the optimized (in terms of final microstructure) Gleeble DIFT test, deformation temperature 675°C, (a) strain=0.6, (b) strain=1.5, (c) strain=3.0.

5.6.3 Effect of deformation temperature on DIFT

To study the effect of deformation temperature on final microstructure, a strain of 1.5 was selected. **Figures 5.21 b** and **5.22** show the final microstructures for deformation temperatures of 675°C and 700°C, respectively. There was no effect of deformation

temperature on ferrite fraction (ferrite fraction of 0.81 at 675°C, vs. ferrite fraction of 0.82 at 700°C), and d_α (d_α of 1.7 μm at 675°C, vs. d_α of 1.5 μm at 700°C).

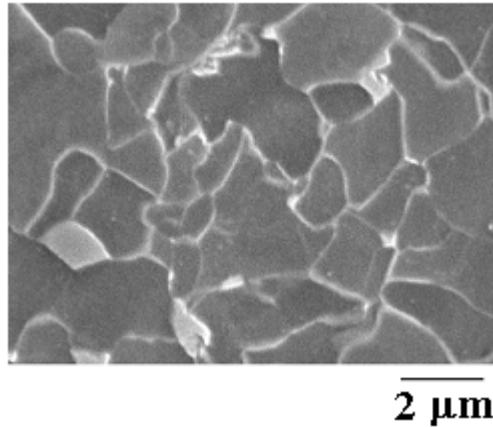


Figure 5.22: Microstructure obtained from torsion replication of Gleeble DIFT test, deformation temperature 700°C, strain=1.5.

However, the DIFT experiments in the Gleeble for the plain C steel, resulted in decreased ferrite fraction with increased deformation temperature.

After establishing the condition to obtain ultra fine ferrite structure through hot torsion, subsequent tests were done to simulate the entire hot strip mill processing with a final DIFT pass.

5.6.4 Simulation of DIFT for hot strip mill processing

A simulation schedule previously proposed for the hot strip rolling of dual phase steels [96] that consisted of reheating at 1200°C followed by one roughing and 7 finishing

passes executed in the austenite region, was modified for the DIFT treatment by adding an eighth finishing pass [Table 5.16]. After F7 the sample was cooled at 40°C/s to a selected DIFT pass temperature (i.e. 675 °C and 650 °C, respectively) where it was deformed to an equivalent strain of 1.5 and subsequently cooled at approximately 30°C/s. The stress-strain curves of the DIFT passes are shown in Figure 5.23. Here, the flow stress increased initially rapidly and showed dynamic softening at higher strains that could readily be attributed to ferrite formation during deformation. This flow stress behaviour provided some evidence that a significant volume fraction of ferrite was formed during deformation as opposed to immediately after deformation. The final microstructures are shown in Figure 5.24 confirming that this treatment resulted in an ultra fine ferrite microstructure with a ferrite fraction of 0.84 and grain size of 2 µm for the DIFT pass at 675°C, while for the DIFT pass at 650°C an even finer ferrite grain size of 1.3 µm was observed with a ferrite fraction of 0.90 [Table 5.17]. The second phases obtained here were depleted of martensite. As the cooling rate was slow (~30°C/s) after the final DIFT pass pearlite/bainite was observed in the final microstructure.

Table 5.16: Simulated rolling schedule for DIFT

Pass No.	R	F1	F2	F3	F4	F5	F6	F7	DIFT
Strain	1.05	0.68	0.56	0.47	0.41	0.37	0.3	0.26	1.5
Temperature(°C)	1150	1100	1060	1020	980	950	920	895	650,675
Interval time (s)	10.0	4.8	3.1	2.2	1.6	1.2	0.9	6.13, 5.5*	

*These two interval times indicate the times necessary to cool the samples to the required two deformation temperatures (650°C and 675°C) at a cooling rate of 40°C/s.

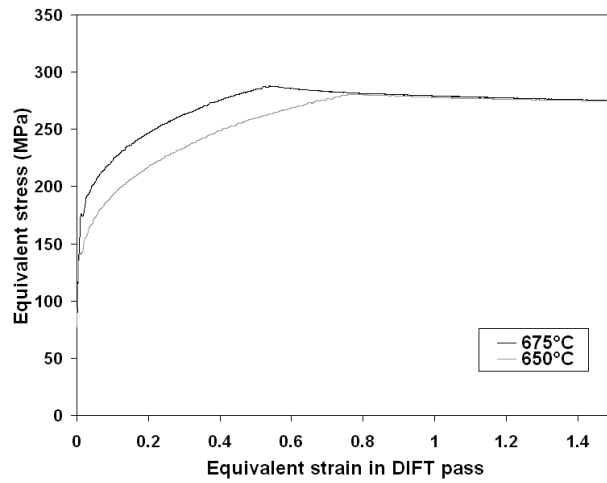


Figure 5.23: Stress-strain curve of DIFT passes during hot strip rolling simulation of plain C steel.

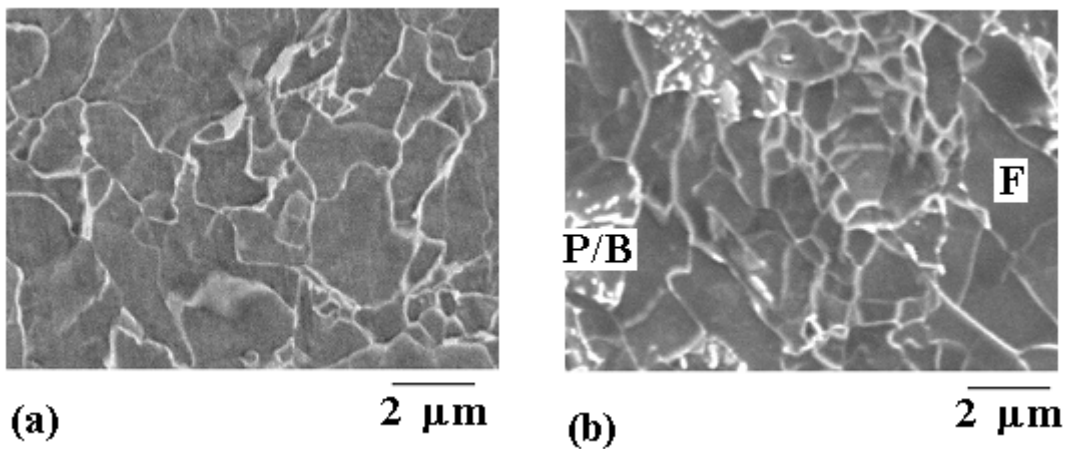


Figure 5.24: Simulated hot strip rolling microstructure of plain C steel with final DIFT pass at (a) 675°C, (b) 650°C.

Table 5.17: Ferrite fraction and grain size after hot rolling simulation of DIFT

DIFT pass temperature, °C	Ferrite fraction	d_{α_s} μm	H _v
650	0.90	1.3	176±3
675	0.84	2.0	179±3

Tensile tests were carried out for samples where the final DIFT pass was given at 650°C. Three tests have been performed and **Figure 5.25** shows a typical stress-strain curve obtained. Based on the three tests a yield strength of 503±7 MPa, UTS of 602±8 MPa, and uniform elongation 9.6±0.4% was determined. As the tensile specimen geometry was not a regular solid gauge one, total elongation could not be reported from these tests.

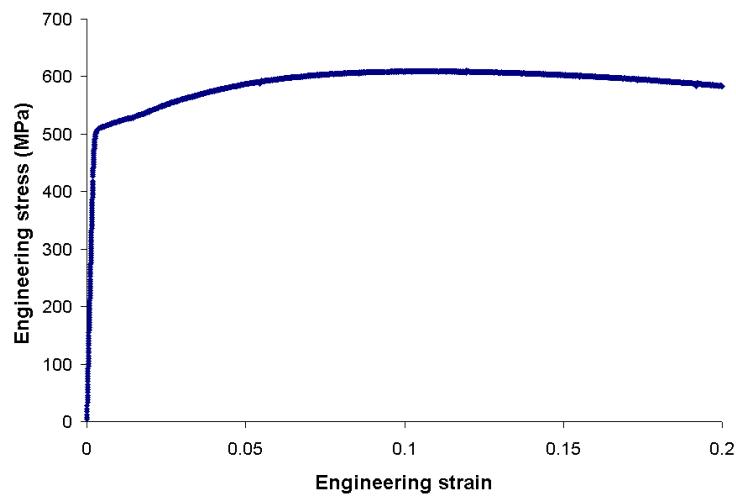


Figure 5.25: Tensile curve for simulated hot strip rolling microstructure of plain C steel with final DIFT pass at 650°C.

However, the tensile properties obtained were not attractive. The tensile strength obtained was much lower than that expected from an ultra fine dual phase steel. For example Son et al. reported a tensile strength of 978 MPa for a ultra fine grained dual phase steel with a martensite fraction of 0.28 [7]. In the present stress-strain curve a minor plateau was observed after the yield point. The yield point elongation might have been suppressed by the sample geometry. These relatively low strength tensile properties were attributed to the absence of martensite as the second phase, in the simulated hot strip rolling microstructure.

5.7 Discussion

Applying the largest deformation to the finest prior austenite grain size resulted in similar microstructures with predominantly ultra fine ferrite structure for all chemistries studied. However, the evolution of microstructure with strain depended in detail on steel chemistries. By studying the microstructures at different strain levels the path to the formation of ultra fine ferrite by DIFT can be described.

In this study it was observed that for the plain C steel, increasing the strain gradually replaced coarse grained ferrite with fine grained ferrite and simultaneously the overall ferrite fraction increased [**Figure 5.6**]. This was similar to the findings of Hong et al. [38] for DIFT in plain C steel with fine prior austenite grain size. In **Figure 5.26**, the volumetric grain size distribution of ferrite grains are plotted for different amounts of

strain. Using the frequency distribution $f(x)$, the volume fraction of grains with size x is given by:

$$f_v = \frac{x^3 f(x)}{\int_0^{\infty} x^3 f(x) dx} \quad (5.2)$$

For plain C steel dynamic ferrite nucleation occurred at all levels of applied strain. The nucleation density was lower in the case of lower strain leading to larger ferrite grains.

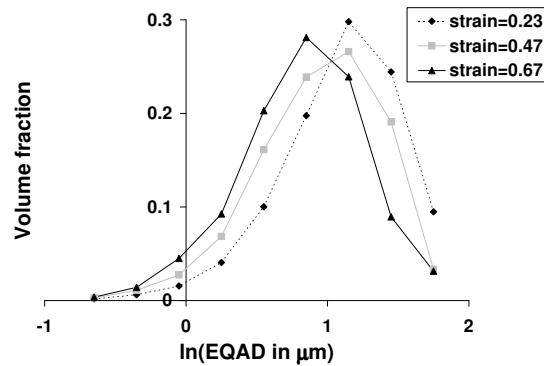


Figure 5.26: Volumetric grain size distribution of ferrite grains for plain C steel after DIFT with different strains.

The evolution of microstructure with strain for the Nb steel is shown in **Figure 5.27** [97]. The lowest amount of strain ($\epsilon=0.2$) resulted in a predominantly bainitic structure for the Nb steel. Comparing with the results of the plain carbon steel where essentially the same DIFT temperatures were employed (i.e. 672 vs 675°C) might suggest that in the Nb steel the velocity of the austenite-ferrite interface was much lower. This hypothesis is consistent with the well-established observation that Nb slows down ferrite transformation rates. Increasing the amount of strain to $\epsilon=0.4$ formed a more polygonal

ferritic structure with a ferrite fraction of 0.55 and an average grain size of 2.4 μm . Again, on increasing the amount of strain to 0.6 an ultra fine ferritic structure was obtained.

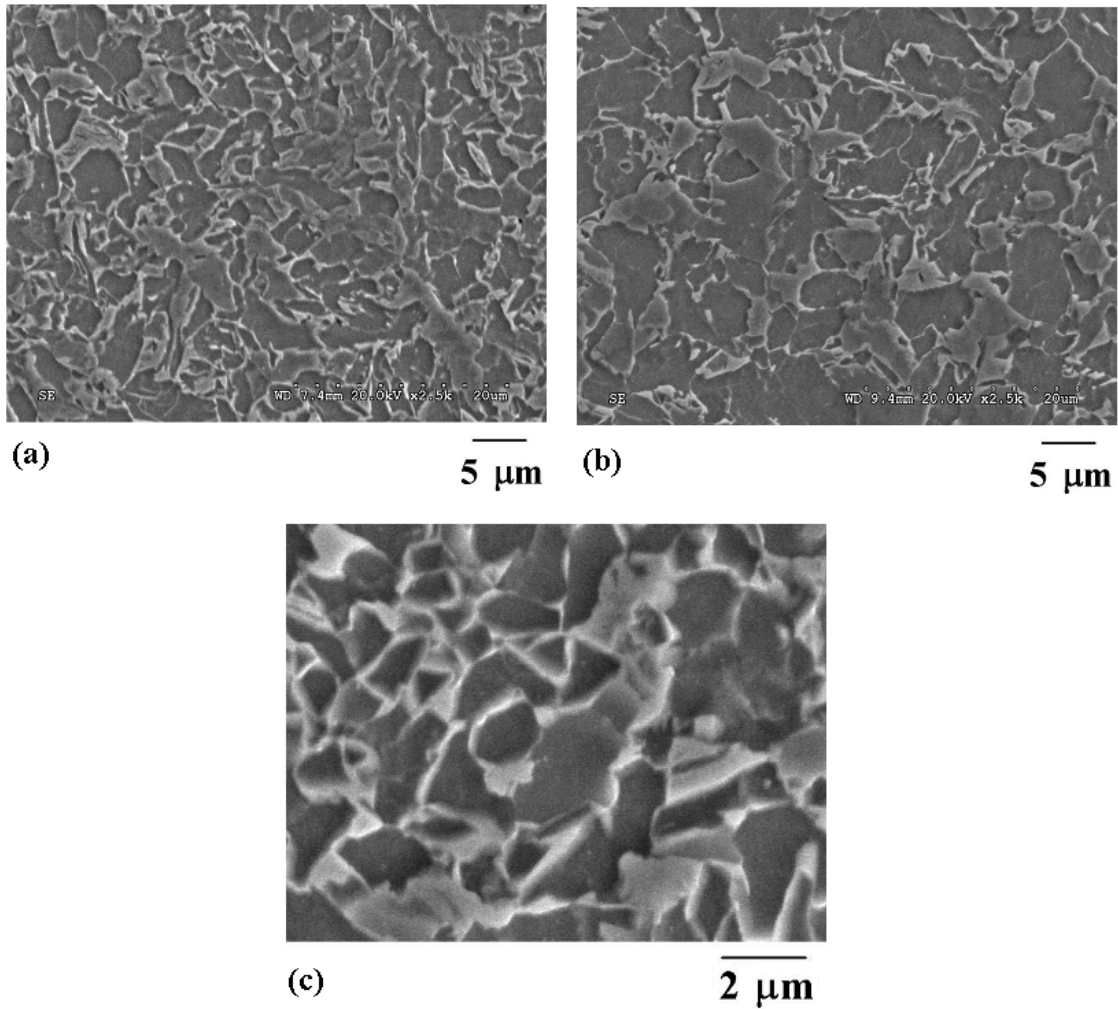


Figure 5.27: Effect of strain on microstructure for Nb steel reheated at 950°C and deformed at $\Delta T = 25^\circ\text{C}$: (a) Strain =0.2, (b) Strain =0.4, (c) Strain =0.6 [97].

For the Mo steel a predominantly bainitic structure was formed when lower strain was applied, which was gradually transformed to an ultrafine grained ferrite structure by increasing the amount of strain (**Figure 5.28**). From **Figure 5.28 (a)** it seems that the lowest amount of strain ($\epsilon=0.15$) initiated some ferrite transformation. With increasing the strain to 0.35, the amount of ferrite increased (**Figure 5.28 (b)**). Further increment of strain resulted in an ultra fine dual phase structure (**Figure 5.28 (c)**).

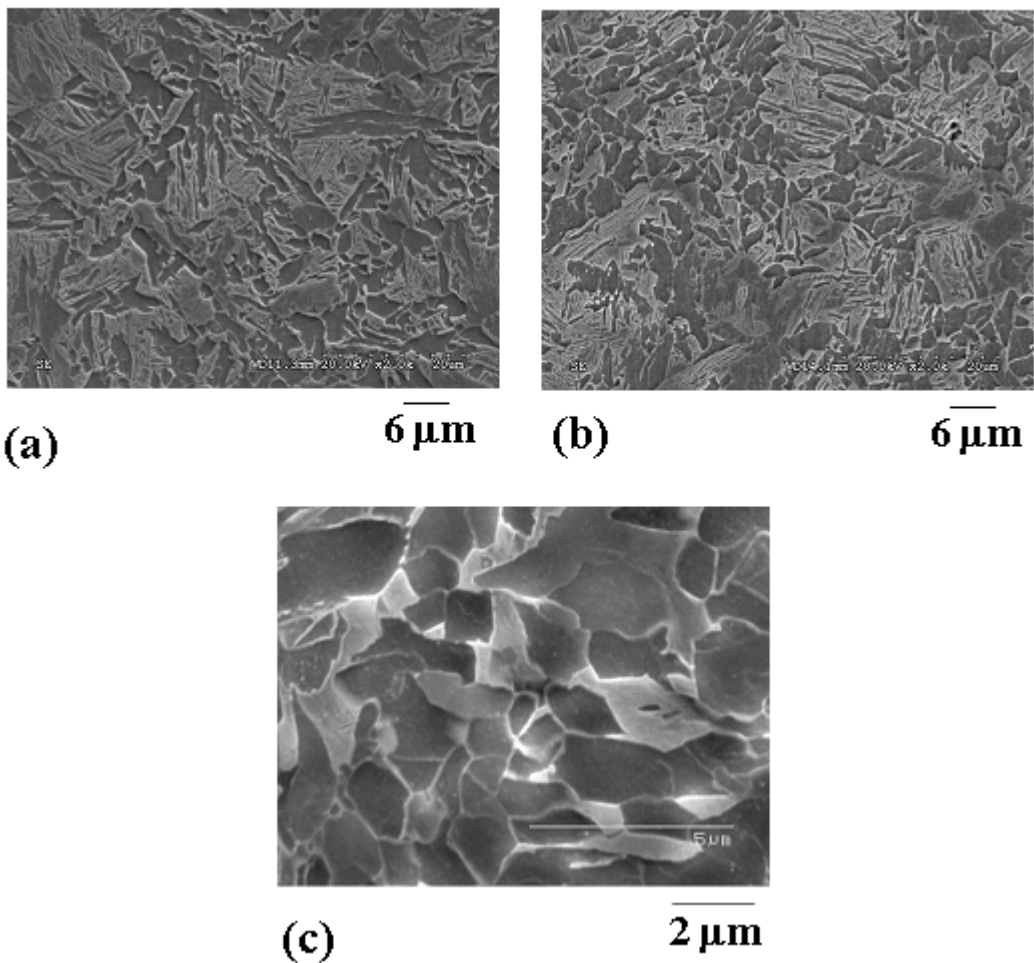


Figure 5.28: Effect of strain on microstructure for Mo steel reheated at 1050°C and deformed at $\Delta T = 30^\circ\text{C}$: (a) Strain = 0.15, (b) Strain = 0.35, (c) Strain = 0.55.

The evolution of microstructure with strain for the Mo-Nb steel is shown in **Figure 5.29** [2]. The Mo-Nb steel followed the trend of the Mo steel when the amount of strain was increased during deformation. But compared to the Mo steel, less ferrite was formed at a particular strain consistent with Nb microalloying. The partly non-polygonal nature of the ferrite grains (example shown in **Figure 5.12 (d)**) resulted from the comparatively low deformation temperature for this chemistry (627°C), i.e. the undercooling below the Ae_3 temperature was 220°C compared to 150 – 170°C for all other steels.

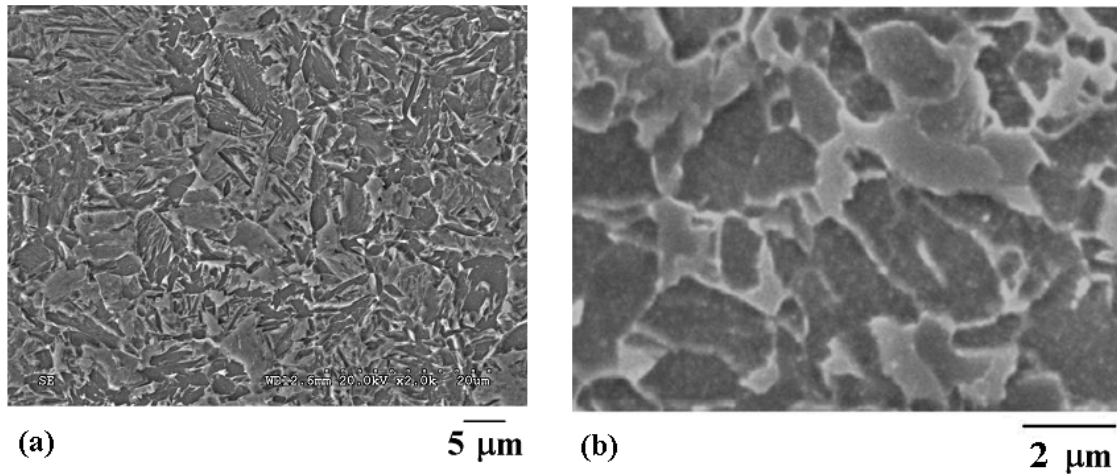


Figure 5.29: Effect of strain on microstructure for Mo-Nb steel reheated at 950°C and deformed at $\Delta T = 25^\circ\text{C}$: (a) Strain =0.2, (b) Strain =0.6 [97].

In the Mo steel, the initial austenite grain size had a marginal effect on the final microstructure. But for the Nb containing steels increasing the prior austenite grain size retarded the DIFT potential. This was in accordance with the findings of Hong et al. [39]. In contrast, Hurley et al. reported increased DIFT potential for increased prior austenite

grain size [30]. This contradiction may be due to the fact that changing the austenite grain size also changes the A_{r3} temperature, which in turn affects the deformation temperature in the DIFT schedule. In particular for the Nb containing steels, bainite rather than ferrite was formed at A_{r3} when d_{γ} is increased. The higher reheating temperature employed to obtain larger d_{γ} was expected to dissolve a significant amount of Nb into solution. The combined effects of larger d_{γ} and more Nb in solution resulted in a pronounced delay of ferrite formation. Thus, austenite grain size cannot be considered as an independent parameter in the DIFT process.

The Mo steel has a typical DP600 chemistry that was developed for cold rolled and annealed DP steels [102]. An extensive data base is available for the microstructure evolution in this steel that is applicable to the currently employed commercial processing routes, i.e. hot rolling and intercritical annealing, respectively, to produce DP steels [96, 103, 104]. Thus, this steel was selected to evaluate the improvement of the final microstructure by DIFT as compared to the conventional techniques. A typical microstructure obtained by the intercritical annealing route consists of 82% ferrite with a grain size of 6 μm [103]. On the other hand, a typical microstructure obtained by hot rolling simulation of the Mo steel (prior austenite grain size of 13 μm) consisted of 81% ferrite with a grain size of 8.6 μm [96]. In the case of thermo-mechanically controlled processing (TMCP) prior austenite grain size, amount of deformation, and subsequent cooling rate affected the final microstructure. An optimum combination of the finest prior austenite grain size of 13 μm , a strain of 0.5 at 850°C, and a subsequent cooling rate of 60°C/s resulted in a ferrite grain size of 3.5 μm with a ferrite fraction of 84%, which was

the finest ferritic microstructure obtained in the set of simulations reported in the literature [104]. Clearly, DIFT can produce a predominantly ferrite microstructure with a considerably finer final ferrite grain size as compared to the conventional techniques. To evaluate the strength increase by grain refinement, hardness data can be used. A hardness value of 167 HV was obtained for the conventional DP microstructure obtained by simulation of cold rolling and annealing. In contrast, in the DIFT sample, a hardness of 204 HV has been recorded. This projects a tensile strength increase of 20% from the observed grain refinement of 6 to 1 μm .

The simulation of industrial DIFT processing with hot torsion tests for the plain C steel gave promising results to realize ultra fine ferrite microstructures in as-hot rolled plain carbon steels, i.e. without the addition of costly alloying elements. The applied strain in the DIFT pass may appear excessive but this is just an artefact of the torsion deformation mode that appears to be less efficient at introducing viable ferrite nucleation sites at micro-shear bands. For rolling, a reduction of approximately 35% (true strain 0.5) can be expected to be sufficient for this purpose. Even so, the proposed schedule is beyond the capabilities of conventional hot strip mills. In addition, the low deformation temperature ($\sim 650^\circ\text{C}$) may be more of a problem. An additional mill stand would have to be added in the run-out table area. This could be considered in designing new mills but will first require a detailed assessment of the robustness of the proposed processing path. Alternatively, recent work by Morimoto et al. [34] suggested that DIFT can be initiated in the final stands of the 7 stand finish mill by proper interstand cooling in conjunction with asymmetric rolling that produces significant shear strain to reach the critical strain levels

for ultra fine ferrite formation. In any event, a distinct advantage of the DIFT route would be the rapid formation of ferrite (within less than 1 s), thereby eliminating the need for a slow cooling period of 10 s through the ferrite formation stage in current production of hot-rolled dual phase steels.

6. Modelling of DIFT

6.1 Introduction

To get insight into the DIFT mechanisms, a first generation model was developed that describes nucleation and growth of ferrite during and after deformation. The model takes into account the principles of the underlying phenomena during DIFT (for example, introduction of ferrite nucleation sites inside the prior austenite grain, ferrite nucleation during the deformation step, etc.). One of the challenges faced in this modelling study was the austenite grain structure. During deformation the austenite grains were being pancaked, while nucleation occurred in parallel. To take this into account a representative austenite domain was selected for modelling. In that representative austenite domain the ferrite nuclei were introduced with systematic spatial and time distribution. Due to the complexity of the process, a number of additional simplifications were made:

(i) In this study it was assumed that most of the stored energy of deformed austenite was in the deformed structure that promoted ferrite nucleation (i.e. deformation bands which acted as ferrite nucleation sites). After nucleation ferrite was assumed to grow into a rather dislocation free zone. In this model the driving force of austenite to ferrite transformation was the chemical driving force only and a potential increase of the driving force due to the deformed-austenite structure was neglected.

(ii) Solute-drag on the moving interface was not considered in this study, which implies that the austenite-ferrite interface mobility should be seen as an effective mobility.

Thus, the model may have limitations in its predictive capabilities, i.e it attempts to address the principles and trends of DIFT, without necessarily providing a detailed quantitative analysis.

To implement the spatial distribution of ferrite nuclei, a meso-scale modelling approach was selected using the phase field approach. Austenite to ferrite transformation for the present low carbon steel was described by mixed-mode modelling, i.e. the phase field model was combined with that of carbon diffusion. This provided a growth model that was coupled with the nucleation assumptions, which served as an input to the phase field model.

The two adjustable parameters for the modelling strategy were, the nucleation detail (nucleation time and spatial distribution of nuclei), and the interface mobility. They were adjusted to match the experimental ferrite fraction and the ferrite grain size spread.

6.2 Model approach

6.2.1 Experimental condition selected for modelling

Modelling was performed for the processing conditions that led to the optimized UFF dual phase microstructure in the Mo steel. For this steel a wealth of data is available for

continuous cooling transformation [9,105]. This set the following frame for the simulations: a prior austenite grain size of 13 μm , a deformation temperature of 695°C, a deformation time of 0.6 s, and a post deformation cooling rate of 70°C/s (from 695°C to 600°C). Even though there was a change in the cooling rate with decreasing temperature, an average cooling rate between 695°C to 600°C could be adopted for the temperature zone of the ferrite formation that is relevant for the present study. The experimental ferrite grain size distribution is shown in **Figure 5.11**. Different spatial and time distribution of ferrite nuclei was examined to match the grain size spread obtained in the simulations, with the experimental one. Each nucleation scenario requires its own value for the interface mobility, $\mu_{\alpha/\gamma}$, to match the overall ferrite fraction between simulation and experiment.

On reviewing the experimental data it was found that the samples were air cooled for about 0.14 s for He quench and 0.42 s for water quench after deformation. The flow of He or water required these times to reach the sample. For the sake of simplicity in the simulations, it was assumed that during these rather small times of air cooling, the samples retain the deformation temperature. The input temperature-time profiles for the calculations are shown in **Figure 6.1**. From **Figure 6.1** it can be observed that deformation and cooling times were quite comparable and hence, calculations were performed until 600°C is reached. Based on the continuous cooling transformation (CCT) data for pancaked austenite 600°C was a reasonable assumption as ferrite transformation stop temperature [9].

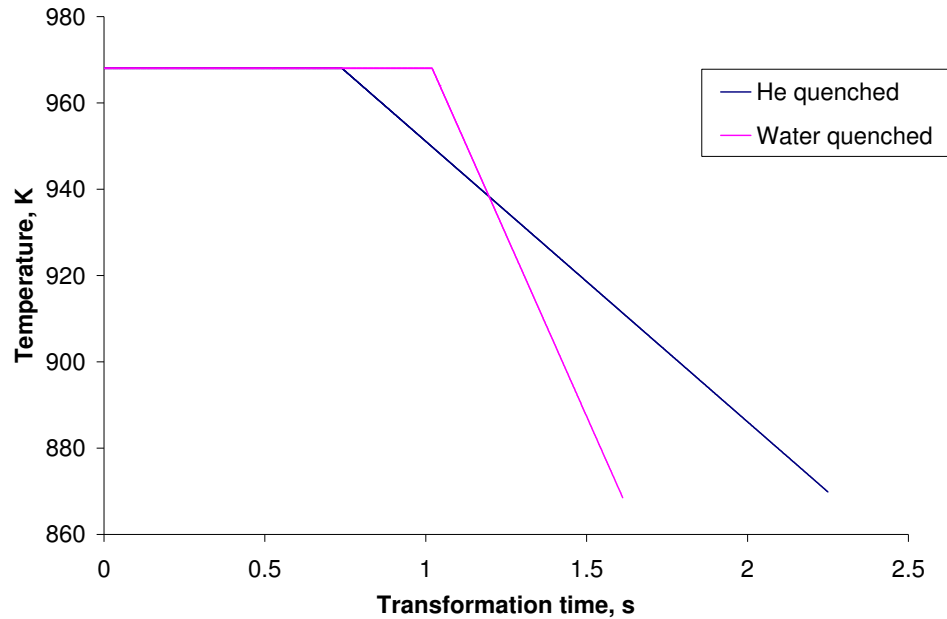


Figure 6.1: Temperature vs. transformation time for Mo steel He and water quenched after DIFT.

In the present model it was assumed that, during deformation below the Ae_3 temperature (which is 1093 K for the Mo steel), ferrite nucleation and growth occur rather than austenite recrystallization [9].

6.2.2 Domain selection

In order to choose an appropriate austenite domain for modelling pancaking of austenite had to be taken into consideration. This pancaking of austenite occurred during the DIFT deformation step. Unemoto et al. quantified the effect of strain on the size and geometry of austenite grains [106]. They assumed the initial austenite grain to be spherical in

shape. Further, for simplicity they also assumed a normalized radius of one for the initial austenite grain. By applying a deformation with reduction p (true strain $\varepsilon = -\ln(1-p)$), the shape of the austenite grain became ellipsoidal (**Figure 6.2**).

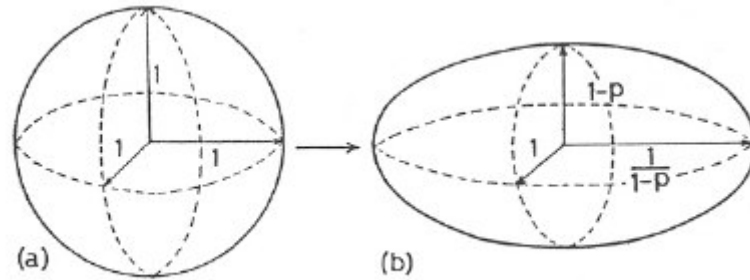


Figure 6.2: Shape and size change of austenite grain by reduction p . [106]

Lacroix et al. [107] suggested that a combined effect of austenite grain size and retained strain on austenite to ferrite transformation could be expressed by introducing an effective austenite grain size. It was postulated that the ferrite instantaneously covered all austenite grain boundaries as thin layer. The growth of the ferrite layer occurred in the direction of the minor axis of the ellipsoidal austenite. Thus, the ferrite growth rate was determined by growth along the small axis. The length of the minor axis of the ellipsoidal austenite in **Figure 6.2** is $1 - p$. Further,

$$1 - p = e^{-\varepsilon} \quad (6.1)$$

Considering the initial austenite grain to be a sphere of diameter d_γ , a deformation with reduction p , would give an ellipsoidal austenite grain with a minor axis of length $d_\gamma(1-p) = d_\gamma e^{-\varepsilon}$. The length of the minor axis was considered to be the effective grain size for the deformed austenite. In the present study the initial austenite grain size for the simulation

case is 13 μm (i.e. when strain is zero). After a strain of 0.6, an effective austenite grain size of $13 \times e^{-0.6} = 7 \mu\text{m}$ could be expected by considering the approach of Unemoto et al. Thus, an austenite grain size of 10 μm was selected as a reasonable approximation for the average pancaking degree during the entire deformation step.

In addition to prior austenite grain boundaries, intragranular deformation structures (e.g. microbands, microshearbands, deformation bands, etc.) provided sites for ferrite nucleation during DIFT. The distribution of DIFT ferrite nuclei should inherit the structure of the deformation bands. (This is similar to the argument that was used for decorating prior austenite grain boundaries by ferrite nuclei to determine the prior austenite grain size.) Beladi et al. used the nomenclature “nucleation band” for ferrite nuclei formed at the deformation surfaces inside the austenite grain [37].

The pancaking of austenite and the band structure of ferrite nuclei were considered in the present study to select the representation domain for modelling. This is schematically shown in **Figure 6.3**. In the present study two spatial parameters were used to describe the nucleation bands. The first parameter was the internucleus distance in a nuclei band (or nuclei density of a band). The second parameter was the distance between the nuclei bands. These distances are schematically described in **Figure 6.3**. This figure also shows the representation domain selected for modelling. But, due to symmetry, the actual calculation domain is just a quarter of the representation domain (shown in **Figure 6.3**). The width of the actual calculation domain was half of the maximum internucleus distance at a nucleation band. Two-dimensional calculations were done in the present first generation model.

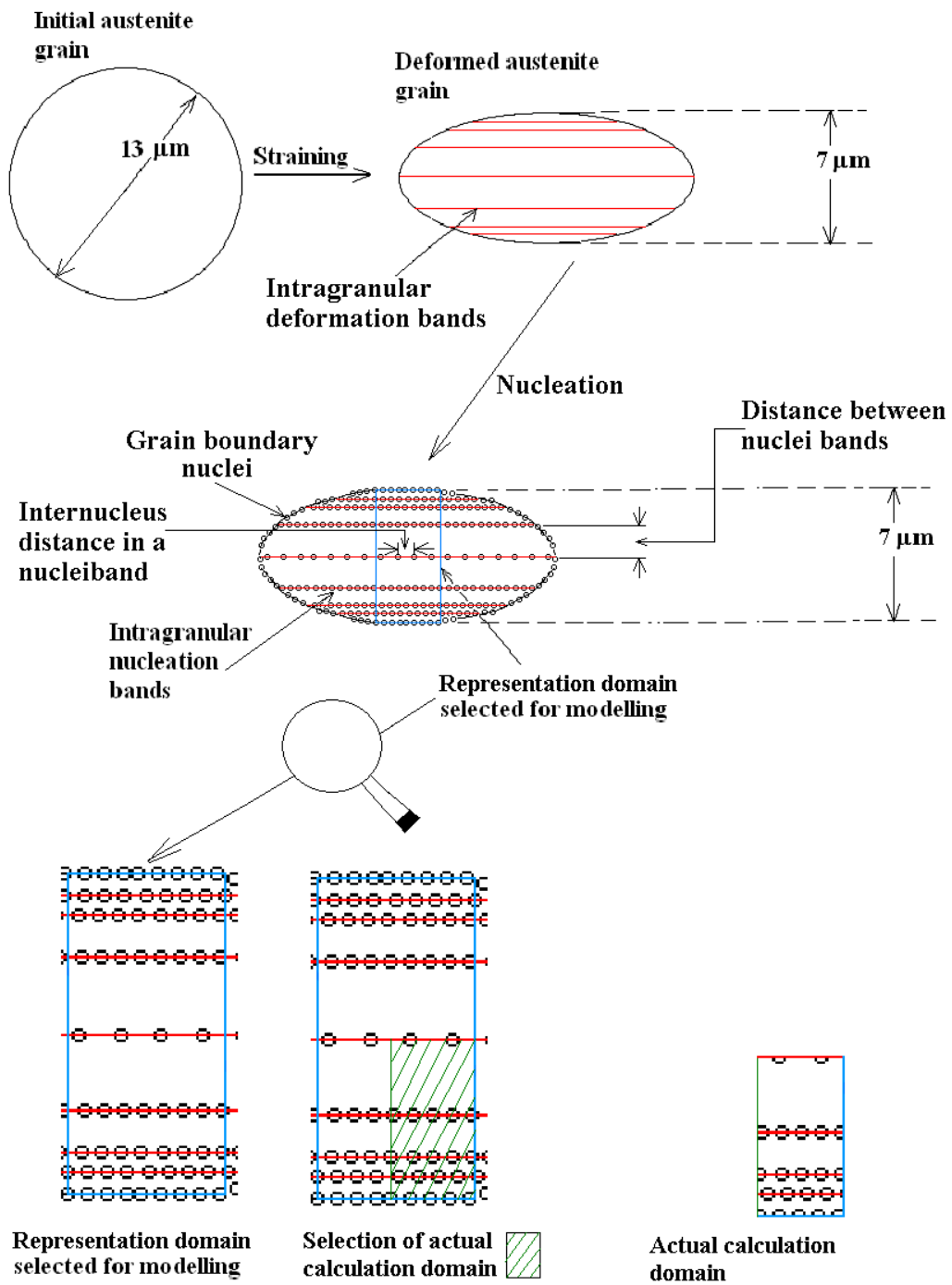


Figure 6.3: Schematic diagram of the selection of representation domain and actual calculation domain for modeling.

6.2.3 Growth model formulation and assumptions

A multi-phase field model was employed with separate phase field parameters for each grain to track the grain size distribution during transformation. The formulation of the multi-phase field model is given below.

The phase field parameters $\phi_i(x,y,t)$ are defined as follows:

$\phi_i(x,y,t)=1$ if in the location x,y at time t the i^{th} grain is present.

$\phi_i(x,y,t)=0$ if in the location x,y at time t the i^{th} grain is absent

(in the present study $i=1$ for austenite, and $i=2,3,\dots$ for different ferrite grains)

$\phi_i(x,y,t)$ changes continuously from 0 to 1 ($0 < \phi_i(x,y,t) < 1$), within a transition region or interface of width η_{ij} (i.e. diffuse interface).

The total free energy of the system (F) is a functional of the ϕ_i 's and $\nabla\phi_i$'s. It can be expressed by the sum of the interfacial energy, the bulk energy of the phases, and the gradient energy at the interface, i.e.,

$$F(\phi_1, \dots, \phi_N, \nabla\phi_1, \dots, \nabla\phi_N) = \int_V \sum_{i,j,i \neq j}^N [f_{ij}^{\text{interfacial energy}}(\phi_i) + f_{ij}^{\text{bulk energy}} + (\phi_i) f_{ij}^{\text{gradient energy}}(\phi_i, \nabla\phi_i)] dV \quad (6.2)$$

where N is the total number of grains. Steinbach et al. [88] proposed a double-obstacle form of the summation of interfacial energy and bulk energy of the phases, i.e., $f_{ij}^{\text{interfacial energy}} + f_{ij}^{\text{bulk energy}}$, in calculating the total free energy of the system:

$$f_{ij}^{\text{interfacial energy}} + f_{ij}^{\text{bulk energy}} = \sigma_{ij}\eta_{ij} \left[\frac{(\phi_i \nabla \phi_j - \phi_j \nabla \phi_i)^2}{2} + \frac{\pi^2 \phi_i \phi_j}{2\eta_{ij}^2} \right] + \Delta G_{ij} h(\phi_i, \phi_j) \quad (6.3)$$

$$\text{with } h(\phi_i, \phi_j) = \frac{2}{\pi} \left[(\phi_i - \phi_j) \sqrt{\phi_i \phi_j} + \frac{1}{2} \arcsin(\phi_i - \phi_j) \right] \quad (6.4)$$

where σ_{ij} , and ΔG_{ij} are the physical material parameters, i.e. the interface energy, and the driving pressure, respectively.

The phase field evolution equation in terms of physical materials parameters is then given by [88]:

$$\begin{aligned} \frac{\partial \phi_i}{\partial t} &= \sum_{j \neq i} \mu_{ij} \left(\nabla \frac{\partial}{\partial \nabla \phi_i} - \frac{\partial}{\partial \phi_i} \right) F_{ij} \\ &= \sum_{j \neq i} \mu_{ij} \left[\sigma_{ij} (\phi_j \nabla^2 \phi_i - \phi_i \nabla^2 \phi_j + \frac{\pi^2}{2\eta_{ij}^2} (\phi_i - \phi_j)) + \frac{\pi}{\eta_{ij}} \sqrt{\phi_i \phi_j} \Delta G_{ij} \right] \end{aligned} \quad (6.5)$$

where, μ_{ij} is the interface mobility.

In the present model this equation was applied at the interface only, i.e., when both $\nabla^2 \phi_i$ and $\nabla^2 \phi_j$ were non-zero.

Equation 6.5 gives the rate of change of each phase field parameter (ϕ_i), by the pair-wise interaction between neighbouring grains. When neighbouring grains had different phases, the interfacial mobility (μ_{ij}), and the interfacial energy (σ_{ij}) in **Equation 6.5**, were given by the ferrite-austenite interface mobility ($\mu_{\alpha\gamma}$), and ferrite-austenite interfacial energy ($\sigma_{\gamma\alpha}$), respectively. For neighbouring grains having different phases, ΔG_{ij} in **Equation 6.5**, was given by the driving force for austenite to ferrite transformation. Before giving further details of the calculation procedure for ΔG_{ij} some other formulations and assumptions need to be described. The phase field equation, i.e. **Equation 6.5**, was

coupled with the carbon diffusion equation. In this study it was assumed that only interstitial atoms (i.e. carbon atoms) could redistribute by long-range diffusion. The substitutional alloying elements (e.g. Mn, Mo) had diffusion coefficients that were orders of magnitude smaller than that for carbon. Thus, they were considered to be immobile in their sublattice. This is the paraequilibrium condition that was used in the ΔG_{ij} calculation. ΔG_{ij} is given by the local concentration of carbon C , and the temperature.

When neighbouring grains had the same phase, ΔG_{ij} was set to zero and the interfacial mobility (μ_{ij}), and the interfacial energy (σ_{ij}) in **Equation 6.5**, were given by the ferrite-ferrite interface mobility ($\mu_{\alpha\alpha}$) and the ferrite-ferrite interfacial energy ($\sigma_{\alpha\alpha}$). In the present calculation, there was just one austenite grain such that austenite grain boundaries had not to be considered explicitly in the simulations.

The local concentration of carbon C at any node depended on the carbon concentration of the austenite portion of that node C_γ , the carbon concentration of the ferrite portion of that node C_α , and the value of the phase field parameters at that point:

$$C = \phi_\alpha C_\alpha + \phi_\gamma C_\gamma \quad (6.6)$$

$$\text{where, } \phi_\alpha = \sum_{\text{for all ferrite grains}} \phi_i \quad (6.7)$$

$$\text{with } \phi_\alpha + \phi_\gamma = 1 \quad (6.8)$$

There were three types of interfaces in this study. They are shown in **Figure 6.4**. For the ferrite-ferrite interface:

$$\phi_\alpha = \phi_2 + \phi_3 = 1 \quad (6.9)$$

$$\phi_\gamma = \phi_1 = 0 \quad (6.10)$$

For the ferrite-austenite interface:

$$\phi_\alpha = \phi_2 + \phi_3 = 0 + \phi_3 = \phi_3 \quad (6.11)$$

$$\phi_\gamma = \phi_1 \quad (6.12)$$

And for the ferrite-austenite-ferrite triple point:

$$\phi_\alpha = \phi_2 + \phi_3 \quad (6.13)$$

$$\phi_\gamma = \phi_1 \quad (6.14)$$

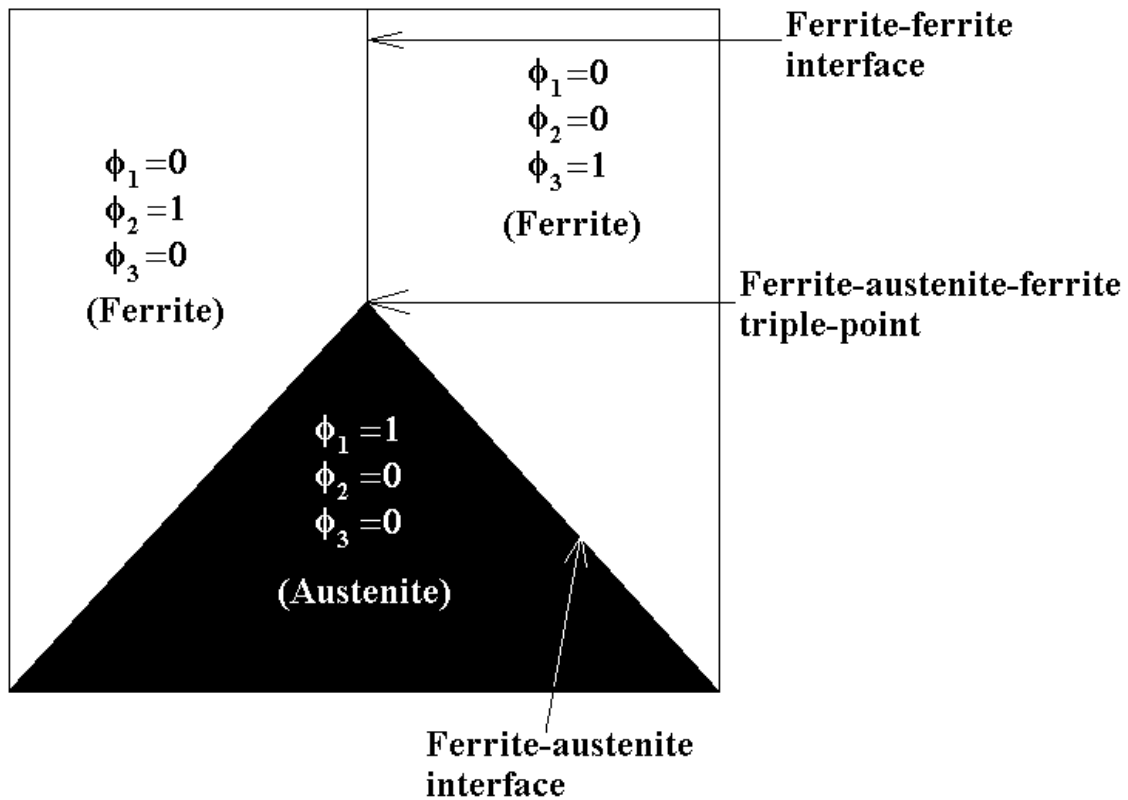


Figure 6.4: Three types of interfaces.

The evolution of C in a particular node is described as [82]:

$$\frac{\partial C}{\partial t} = \nabla \left[\phi_\alpha D_\alpha^c \nabla C_\alpha + \phi_\gamma D_\gamma^c \nabla C_\gamma \right] \quad (6.15)$$

In order to calculate C_α and C_γ it was assumed that at the interface the ratio of $C_\alpha:C_\gamma$ was equal to the equilibrium ratio of $C_\alpha^{eq}:C_\gamma^{eq}=k_{eq}$ at the given temperature [82].

Thus,

$$C_\gamma = \frac{C}{1 + \left(\frac{C_\alpha^{eq}}{C_\gamma^{eq}} - 1 \right) \phi_\alpha} \text{ and} \quad (6.16)$$

and

$$C_\alpha = \frac{C \frac{C_\alpha^{eq}}{C_\gamma^{eq}}}{1 + \left(\frac{C_\alpha^{eq}}{C_\gamma^{eq}} - 1 \right) \phi_\alpha} \quad (6.17)$$

such that,

$$\frac{\partial C}{\partial t} = \nabla \left\{ \frac{D_\gamma^C + \phi_\alpha \left(\frac{C_\alpha^{eq}}{C_\gamma^{eq}} D_\alpha^C - D_\gamma^C \right)}{1 + \phi_\alpha \left(\frac{C_\alpha^{eq}}{C_\gamma^{eq}} - 1 \right)} \left[\nabla C - \frac{C \left(\frac{C_\alpha^{eq}}{C_\gamma^{eq}} - 1 \right)}{1 + \phi_\alpha \left(\frac{C_\alpha^{eq}}{C_\gamma^{eq}} - 1 \right)} \nabla \phi_\alpha \right] \right\} \quad (6.18)$$

Equations 6.5 and **6.18** were numerically solved using the finite forward difference technique. The code was written in FORTRAN.

For the paraequilibrium condition, the driving pressure for austenite to ferrite transformation was quantified from a quasi-binary Fe-C phase diagram for the Mo and Mn levels of the investigated steel. This phase diagram was calculated with THERMOCALC using the Fe 2000 database (**Figure 6.5**). As a deformation temperature of 968K was considered in this modelling exercise, this temperature was used to linearize

the phase diagram to obtain relationships between temperature and equilibrium carbon content in ferrite and austenite, respectively, i.e.

$$T_{\alpha}^{eq} = -10947.0C_{\alpha}^{eq} + 1102.4 \quad (6.19)$$

$$T_{\gamma}^{eq} = -135.22C_{\gamma}^{eq} + 1052.0 \quad (6.20)$$

The temperatures T_i^{eq} (in K) describe the phase boundaries for phases $i(\alpha, \gamma)$ with carbon concentrations C_i^{eq} (in wt%).

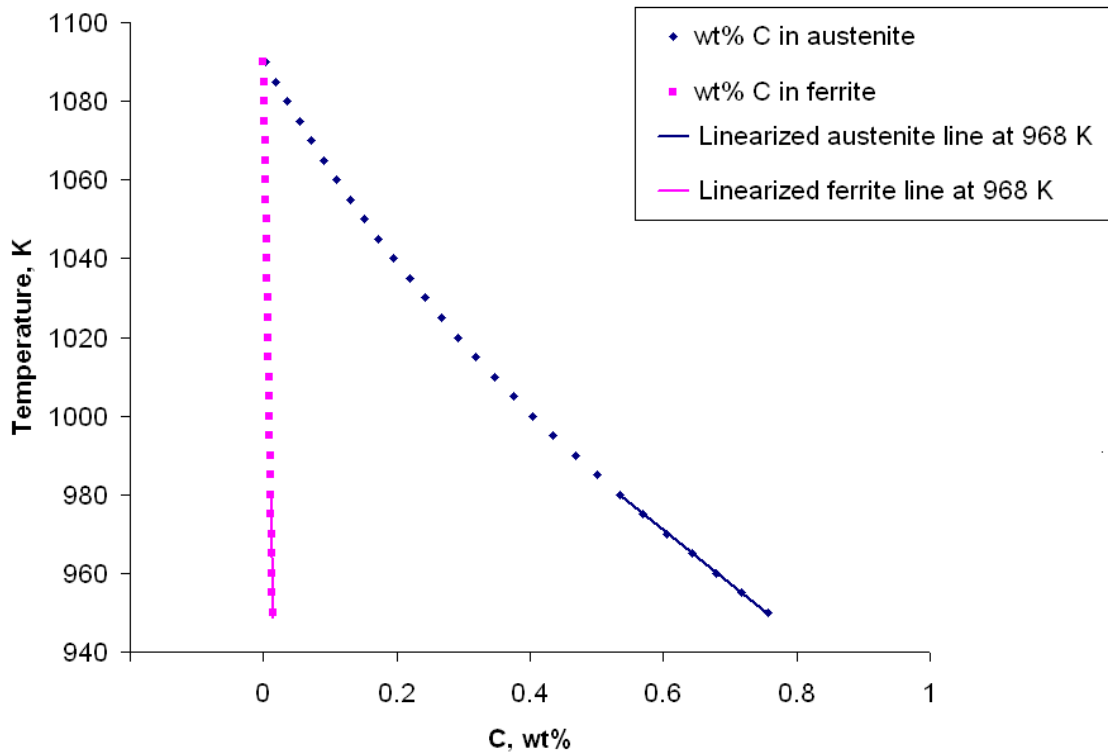


Figure 6.5: Paraequilibrium phase diagram for the Mo steel as calculated by THERMOCALC.

According to this linearized phase diagram, the partition co-efficient of carbon between ferrite and austenite, k , could be determined for each temperature i.e.

$$k = \frac{\frac{T - 1102.4}{-10947}}{\frac{T - 1052}{-135.22}} \quad (6.21)$$

The driving pressure for austenite to ferrite transformation could be quantified by using the undercooling, ΔT^* , which was calculated as:

$$\Delta T^* = (T_{\gamma}^{eq}(C_{\gamma})) + (T_{\alpha}^{eq}(kC_{\gamma})) / 2 - T \quad (6.22)$$

where T is the actual temperature and C_{γ} is the carbon concentration of the austenite phase of the cell (C_{γ} was calculated from **Equation 6.16**). The driving force could then be expressed as:

$$\Delta G = \Delta S \Delta T^* \quad (6.23)$$

This formulation is equivalent to:

$$\Delta G = \Delta H - T \Delta S = \Delta H - T \frac{\Delta H}{T_{eq}} = \frac{\Delta H}{T_{eq}} (T_{eq} - T) = \Delta S (T_{eq} - T) = \Delta S \Delta T^* \quad (6.24)$$

The proportionality factor ΔS was estimated to be $0.318 \times 10^6 \text{ Jm}^{-3}\text{K}^{-1}$ as described in detail in **Appendix 3**.

In the present study, isotropic properties were assumed for interfacial mobilities ($\mu_{\alpha\gamma}$ and $\mu_{\alpha\alpha}$) and energies ($\sigma_{\alpha\gamma}$ and $\sigma_{\alpha\alpha}$). The interfacial mobility $\mu_{\alpha\gamma}$ was employed as an adjustable parameter in this model. It is necessary to mention here again, that solute-drag effects were not considered in this study, and this implies that the austenite-ferrite

mobility should be seen as an effective mobility. Fazeli [105] calculated the effective $\mu_{\alpha\gamma}$ for the Mo steel to be $54 \times 10^{-7} e^{(-168560/8.314T)} \text{ m}^4 \text{ J}^{-1} \text{ s}^{-1}$, in the temperature range of 720 to 650°C based on continuous cooling transformation data for a prior austenite grain size of 24 μm and a cooling rate of 1°C/s. In this study this effective mobility is called “CCT mobility”. However, the growth-rate of ferrite in deformed austenite during DIFT may be different than that in undeformed austenite. Nevertheless, the temperature dependence of mobility in the present work was taken from the calculations of Fazeli. The pre-exponential factor $\mu_{\alpha\gamma}^0$ was taken as an adjustable parameter. The remaining interface properties, i.e. the interfacial energies $\sigma_{\alpha\alpha}$ and $\sigma_{\gamma\alpha}$ and the mobility $\mu_{\alpha\alpha}$ are given together with the diffusivities of carbon in austenite and ferrite in **Table 6.1**.

Table 6.1: Summary of physical parameters

Physical Parameters	Value used	References
$\mu_{\alpha\alpha}$	$5 \times 10^{-13} \text{ m}^4 \text{ J}^{-1} \text{ s}^{-1}$	108
$\sigma_{\alpha\alpha}$	0.1 J m^{-2}	108
$\sigma_{\gamma\alpha}$	0.5 J m^{-2}	108
D_{α}^C	$2.2 \times 10^{-4} e^{(-122500/8.314T)} \text{ m}^2 \text{ s}^{-1}$	109
D_{γ}^C	$1.5 \times 10^{-5} e^{(-142100/8.314T)} \text{ m}^2 \text{ s}^{-1}$	109

6.2.4 Numerical details

The boundary condition used in the simulations is discussed through the example shown in **Figure 6.6**.

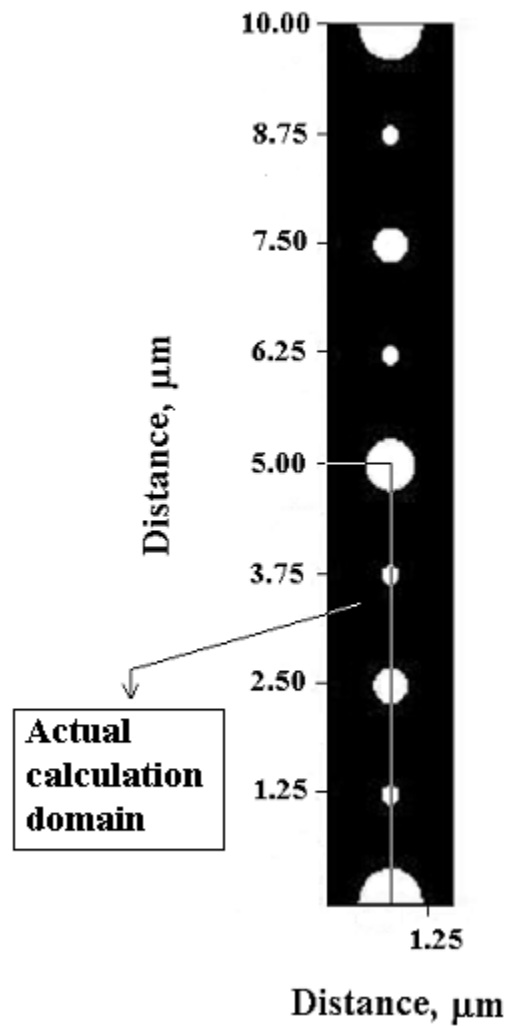


Figure 6.6: An example of selection of actual calculation domain.

The black and the white regions in the figure, indicate austenite and ferrite, respectively. This “representation domain” could have been modelled assuming periodic boundary

condition. However, as the domain was symmetric, only a quarter of it was modelled (as discussed in **Section 6.2.2**). This is shown as “actual calculation domain” in **Figure 6.6**. Symmetric boundary conditions were assumed for the “actual calculation domain”. The “representation domain” shown here was constructed by stitching the four quarters of “actual calculation domain”.

To calculate the evolution of C and the ϕ_i 's at the domain-boundary, ghost nodes were introduced. **Figure 6.7** schematically shows the introduction of ghost nodes at a domain-boundary.

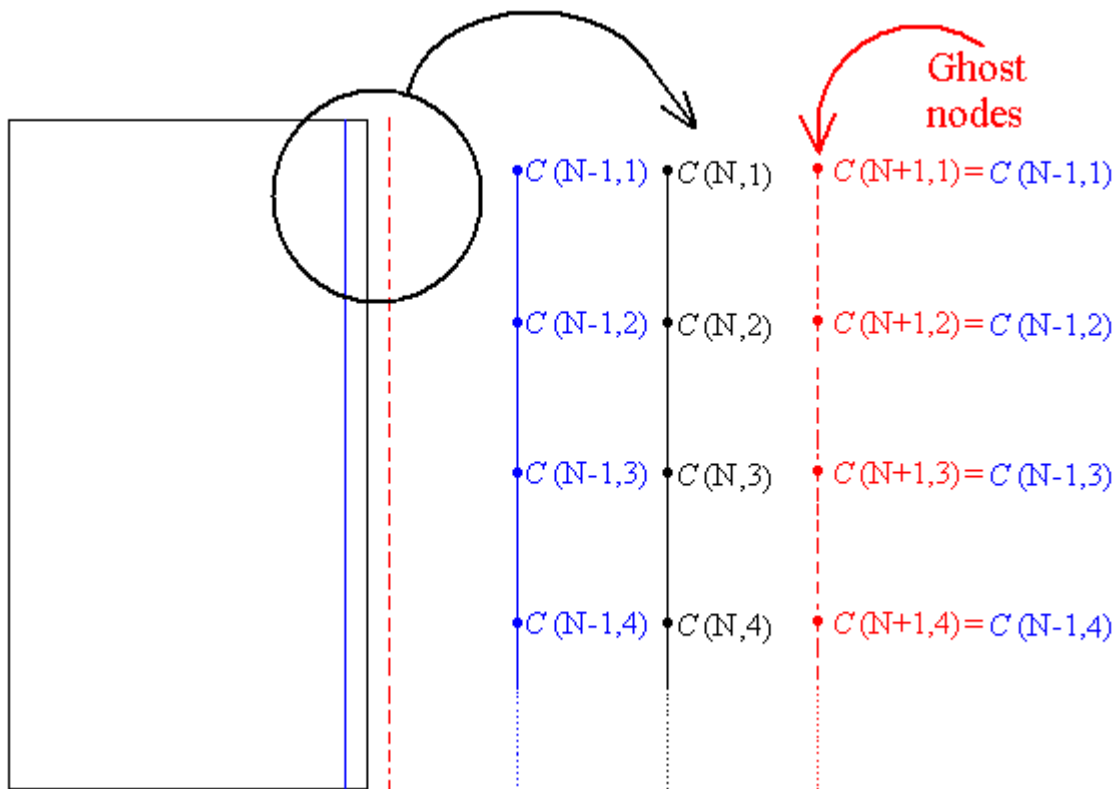


Figure 6.7: Boundary conditions and ghost nodes.

In **Figure 6.7**, the description is given for C only. A similar procedure was followed to determine the ϕ_i 's for the ghost nodes. This symmetric boundary condition ensured carbon balance.

The numerical parameters of this study were node size, interface thickness and time stepping. In general a node size of $0.0125 \mu\text{m}$ was used in the calculations. There were 8 nodes in the interface, which gave an interface thickness of $0.1 \mu\text{m}$. The time stepping was adaptive and depended on node size a (refer to **Appendix 4**), $\mu_{\alpha\gamma}$, and D_α^C . It is the minimum of the following two quantities:

$$\frac{0.2a^2}{\mu_{\alpha\gamma}\sigma_{\gamma\alpha}}, \frac{0.2a^2}{D_\alpha^C}$$

A convergence analysis for the selection of these numerical parameters is given in **Appendix 4**.

In the present study ferrite nuclei were introduced by hand in the austenite matrix at a particular time and position. As an example the introduction of a nucleus (at time= t) is shown in **Figure 6.8**. The phase field parameters along the line AA (as shown in **Figure 6.8**), for the austenite matrix ϕ_1 , and for the ferrite nuclei ϕ_4 , are shown in **Figure 6.9** for both times $t-\Delta t$ and t . The other phase field parameters ϕ_2 , and ϕ_3 are reserved for the other two ferrite grains shown in **Figure 6.8**, and their values are zero along the line AA.

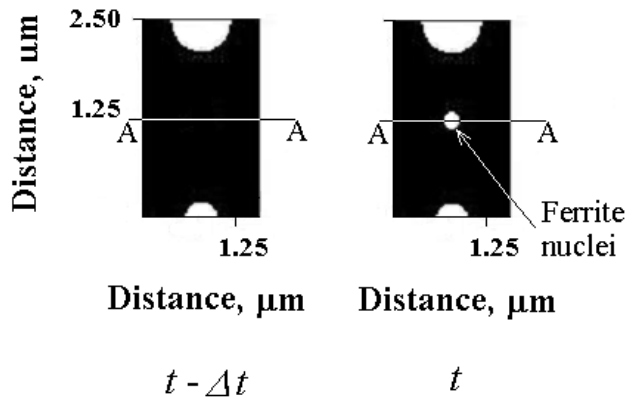


Figure 6.8: Introduction of ferrite nuclei in austenite matrix.

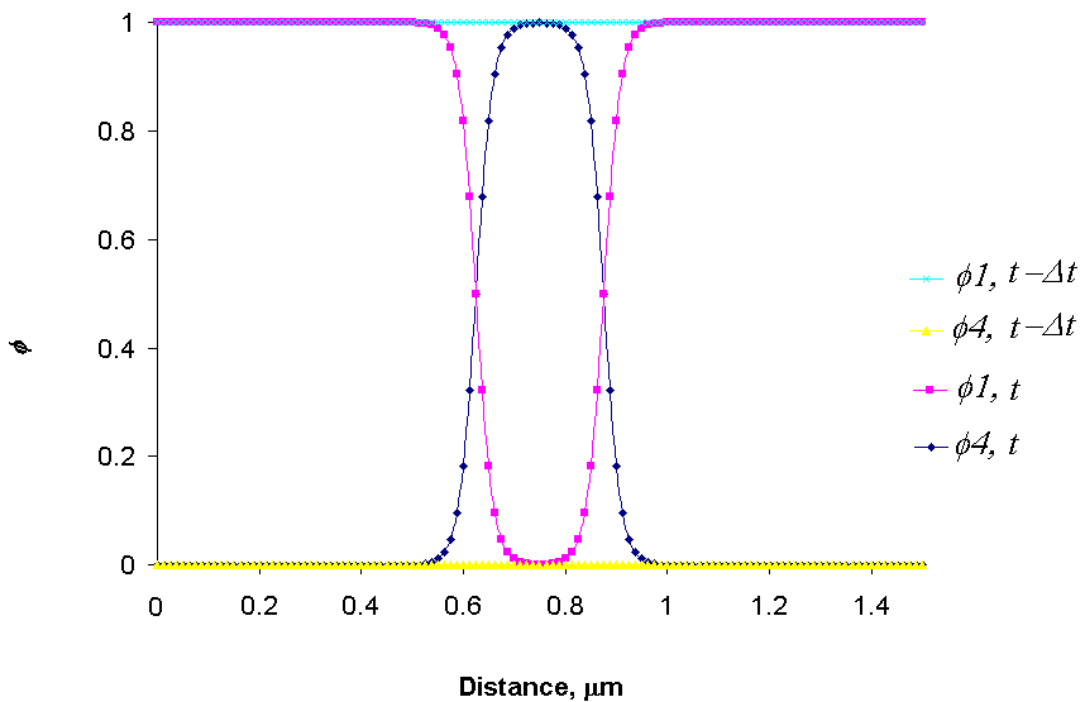


Figure 6.9: Phase field parameters ϕ_1 , and ϕ_4 at the line AA (as shown in **Figure 6.8**) at two times.

The profile of the phase field parameter for the ferrite grain, ϕ_4 , at the ferrite-austenite interface (as shown for time t in **Figure 6.9**) was initiated through [83]:

$$\phi_4(x, y) = 1 - 0.5 \left(1 + \tanh \left(\frac{3(D(x, y) - R)}{\eta} \right) \right) \quad (6.25)$$

where, η is the thickness of the diffused interface and it is set to be $8 \times a$, R is the radius of the nucleus, and $D(x, y)$ refers to the distance of the point (x, y) from the centre of the ferrite nucleus. The radius R coincides in this approach with the position where $\phi_4 = 0.5$. In the present study, R was set as $10 \times a$. After initiating the ferrite nucleus the austenite phase field parameter ϕ_l was reset as,

$$\phi_l(x, y) = 1 - \phi_4(x, y) \quad (6.26)$$

Equation 6.25 was adopted from the work of Mecozzi et al. They analytically formulated this interface-profile of phase field parameter, while deriving the single-phase field evolution equation in terms of physical parameters (interface mobility, interface energy and driving force) [83]. No modification was done to the carbon concentrations of the points where the ferrite nucleus was introduced. It was assumed that the governing equations of the model would diffuse the excess carbon from the ferrite nucleus to the interface.

The ferrite grain sizes were quantified as equivalent area diameter. Due to the lack of statistics in the calculations, a proper ferrite grain size distribution was not obtained. Instead, an approximation of the grain size spread was represented by the ratio of the maximum to the minimum ferrite grain size obtained. The ferrite formed until 0.6 s was considered as the ferrite formed during deformation. This was at par with the

experimental condition that was selected for the modelling purpose, where deformation had been applied for 0.6 s. The average nucleation time for a simulation was determined by summing the nucleation times for all nuclei and then dividing that sum by the total number of nuclei.

6.3 Results

6.3.1 Determination of nominal mobility

To determine a “nominal mobility” the base case was defined as follows: the distance between nucleation bands were 1.5 μm , each band had a nucleus density of 1 nucleus/1.5 μm , and all ferrite nuclei had appeared in the beginning of deformation. This situation was represented with an austenite domain of 1.5 μm ×1.5 μm , and a ferrite nucleus was placed in the centre of the domain. This simple situation has been referred to as “nominal nucleation”. A “nominal mobility” value was determined with this nominal nucleation such that the ferrite fractions obtained from the phase field calculations replicated the experimental values for both water and helium quenched samples. After testing different values for the pre-exponential factor of $\mu_{\alpha\gamma}$ the following value was accepted as nominal mobility: $2 \times 10^{-5} e^{(-168560\text{K}/8.314\text{T})} \text{ m}^4\text{J}^{-1}\text{s}^{-1}$. The nominal mobility is 3.75 times larger than the CCT mobility. In detail, the pre-exponential factor of the nominal mobility is 3.75 times larger than the pre-exponential factor of the CCT mobility. The exponential factor is the same for both of them. The ferrite phase fraction vs. transformation time curves as calculated with the phase field model are shown in **Figure 6.10**. The final ferrite fractions obtained from these simulations are compared with the experimentally observed fractions

in **Table 6.2**. Based on the calculated ferrite fraction from the He quench path, the model leads to a nominal ferrite grain size of 1.6 μm [**Figure 6.11**].

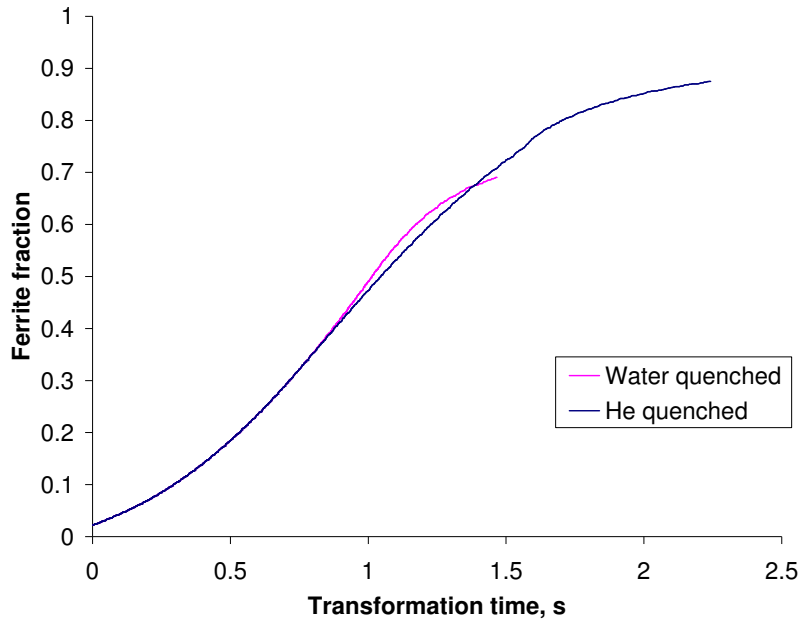


Figure 6.10: Ferrite fraction vs. transformation time for He and water quenched samples after DIFT, obtained from phase field simulations (nominal nucleation).

Table 6.2: Ferrite fractions obtained from experiments and modelling

	Ferrite fraction after helium quenching	Ferrite fraction after water quenching
Experimental	0.86	0.72
Phase field calculation with nominal mobility	0.88	0.69

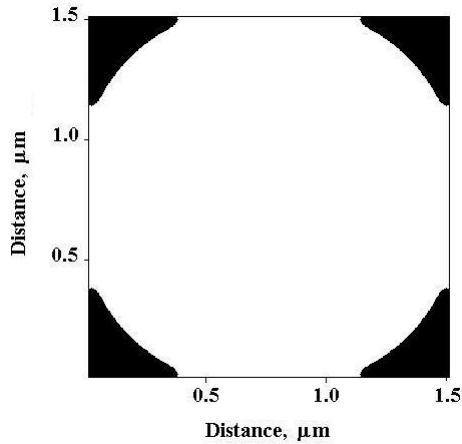


Figure 6.11: Nominal ferrite grain from “nominal nucleation” with $\mu_{\alpha\gamma}$ = nominal mobility and He quenching.

6.3.2 Time and spatial distribution of ferrite nuclei

As the “nominal nucleation” could not give any ferrite grain size spread, distributions of nucleation (both in terms of time and position) were studied to implement the ferrite grain size spread. These simulations were named as “distributed nucleation”. The calculations were done for He quench only for the “distributed nucleation” simulations. Initially five such simulations were performed using the nominal mobility value for $\mu_{\alpha\gamma}$. For “distributed nucleation 1” it was assumed that the ferrite grain size distribution in DIFT is caused by a time difference in the appearance of the nuclei. For this simulation the internucleus distance in a nucleation band and interband distance was kept constant at 1.5 μm and 1.25 μm , respectively. The ferrite internucleus distance at the prior austenite grain boundary was also selected to be 1.5 μm . The distance between the austenite grain boundary and the nearest ferrite nucleation band was selected to be 1.25 μm . A nucleus

that was placed early during DIFT had more time to grow than a nucleus placed later. Here, a domain size of $1.5 \mu\text{m} \times 10 \mu\text{m}$ was considered to represent the ferrite formation across one austenite grain and the first set of nuclei was placed at the two ends of its length that approximates the spacing of the austenite grain boundaries. After each 0.2 s, a nucleus was placed in the middle of the previous two nuclei. This process was repeated until the domain was filled with nuclei.

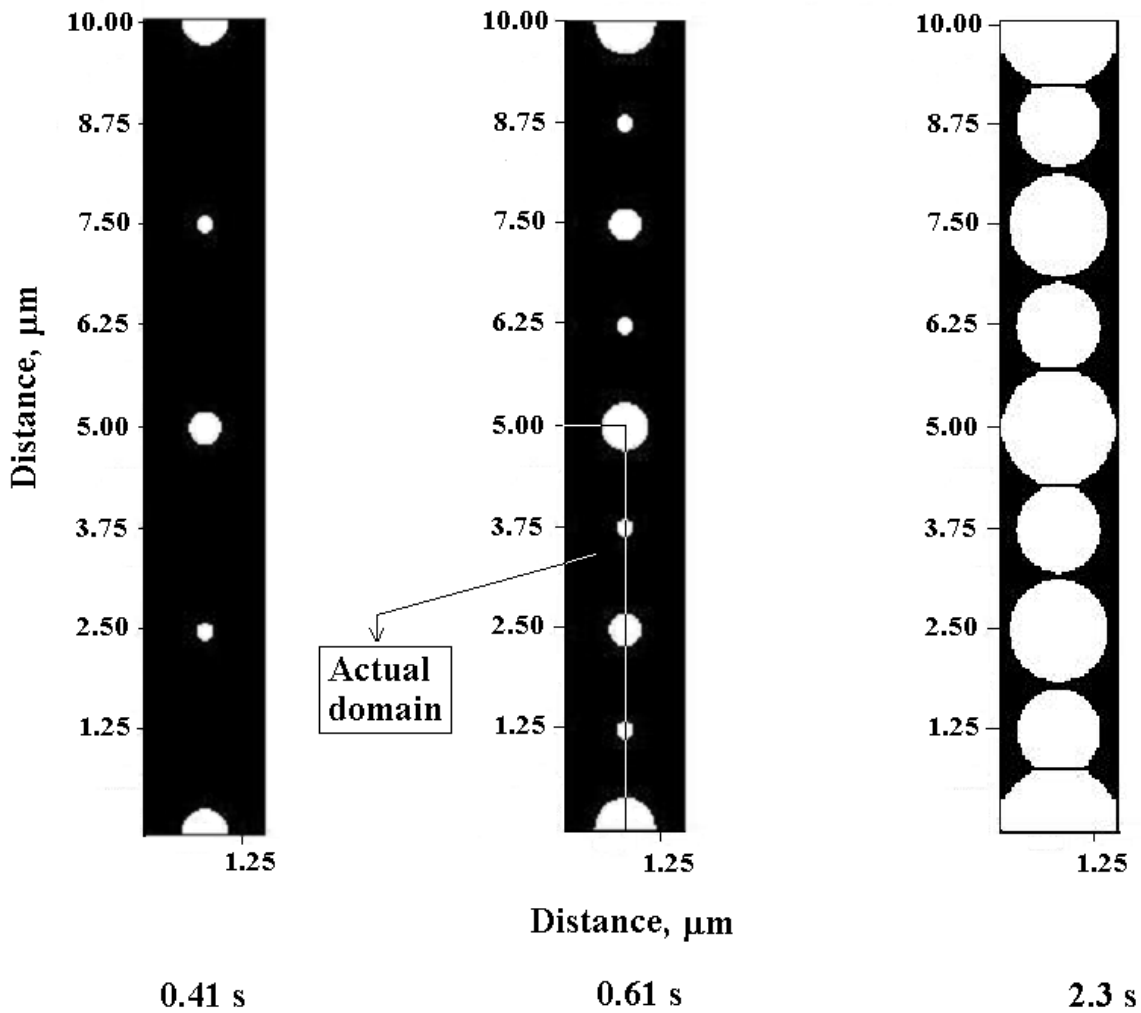


Figure 6.12: Simulated microstructure for “distributed nucleation 1” ($\mu_{\alpha\gamma}$ =nominal mobility).

The placing of the subsequent nucleus in between the previous two nuclei would enable the previous nuclei to grow for the longest time, before the nucleation of the nearest ferrite grains. Till a deformation time of 0.6 s, 4 sets of nuclei were placed. The evolution of microstructure predicted with “distributed nucleation 1” is shown in **Figure 6.12**. In **Figure 6.12** the size of the ferrite grain indicates its appearance time.

The role of distribution of internucleus distance, interband distance, and nucleation time was studied in “nucleation distributions 2-5”. From **Figure 5.11** it can be observed that there are large (~4 μm) ferrite grains in the DIFT microstructure. The presence of these large ferrite grains may indicate that the austenite domain contains region with low spatial density of ferrite nuclei. This region could not be at the prior austenite grain boundary as it was reported in the literature that during DIFT the first set of high density ferrite nuclei appear at the austenite grain boundary [37, 110]. This logically leads to the assumption that the austenite grain interior lacks the presence of a high spatial density of ferrite nuclei. The following reasons were attributed for this assumption: (i) ferrite is softer and its presence leads to less deformation of austenite regions, (ii) quality of ferrite nucleation sites in austenite grain interior is different from those at the austenite grain boundary. The lack of ferrite nucleation in the austenite grain interior was translated in the simulations “distributed nucleations 2-5”. In “distributed nucleations 2-5” both internucleus distance and interband distance were selected to be at their minimum close to the prior austenite grain boundaries. These two parameters gradually increase inside the prior austenite grain.

Keeping the internucleus distance constant at 1.5 μm (both at the austenite grain boundary and at the intragranular nucleation bands) the interband distances were varied in “distributed nucleation 2”.

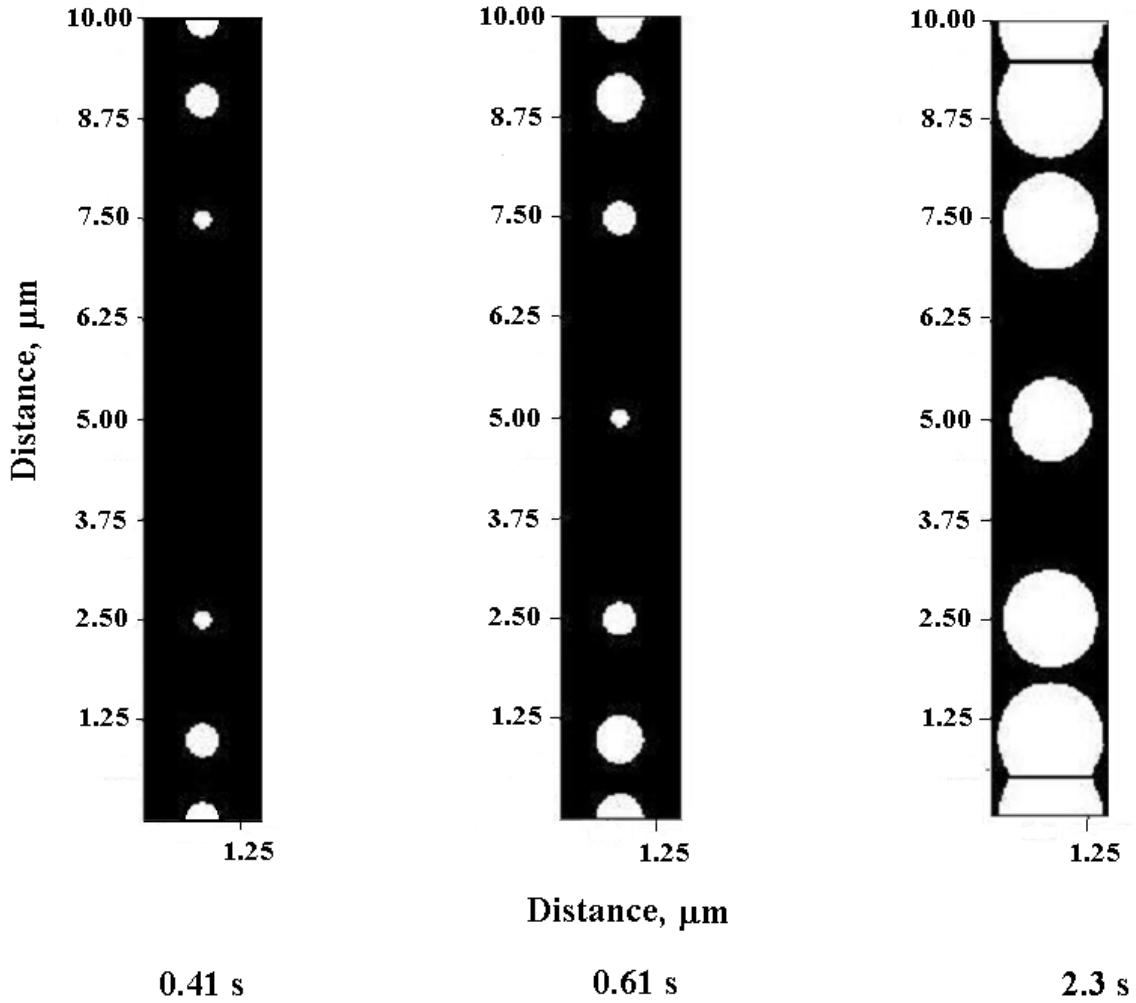


Figure 6.13: Simulated microstructure for “distributed nucleation 2” ($\mu_{\alpha\gamma}$ =nominal mobility).

At 0.2 s nuclei were introduced at the grain boundary and at the adjacent intragranular nucleation band located 1 μm away from the grain boundary. At 0.4 s another intragranular nucleation band was placed at a distance of 1.5 μm from the first intragranular nucleation band. At 0.6 s the last intragranular nucleation band was placed at a distance of 2.5 μm from the second intragranular nucleation band. The microstructure obtained with this scheme is shown in **Figure 6.13**.

In “distributed nucleation 3” both interband distance and internucleus distance in bands was varied (**Figure 6.14**). To introduce the low-density intragranular nucleation bands, the considered austenite domain was increased in the second dimension parallel to the grain boundary. At 0.2 s nuclei were introduced at the grain boundary and at the adjacent intragranular nucleation band. Both at the grain boundary and at the first intragranular nucleation band the nuclei density was selected to be 1 nucleus/ μm . The distance between the grain boundary and the first intragranular nucleation band was 1 μm . At 0.4 s another intragranular nucleation band was placed at a distance of 1.5 μm from the first intragranular nucleation band, with a density of 1 nucleus/ 2 μm . At 0.6 s the last intragranular nucleation band was placed at a distance of 2.5 μm from the second intragranular nucleation band, with a density of 1 nucleus/ 4 μm .

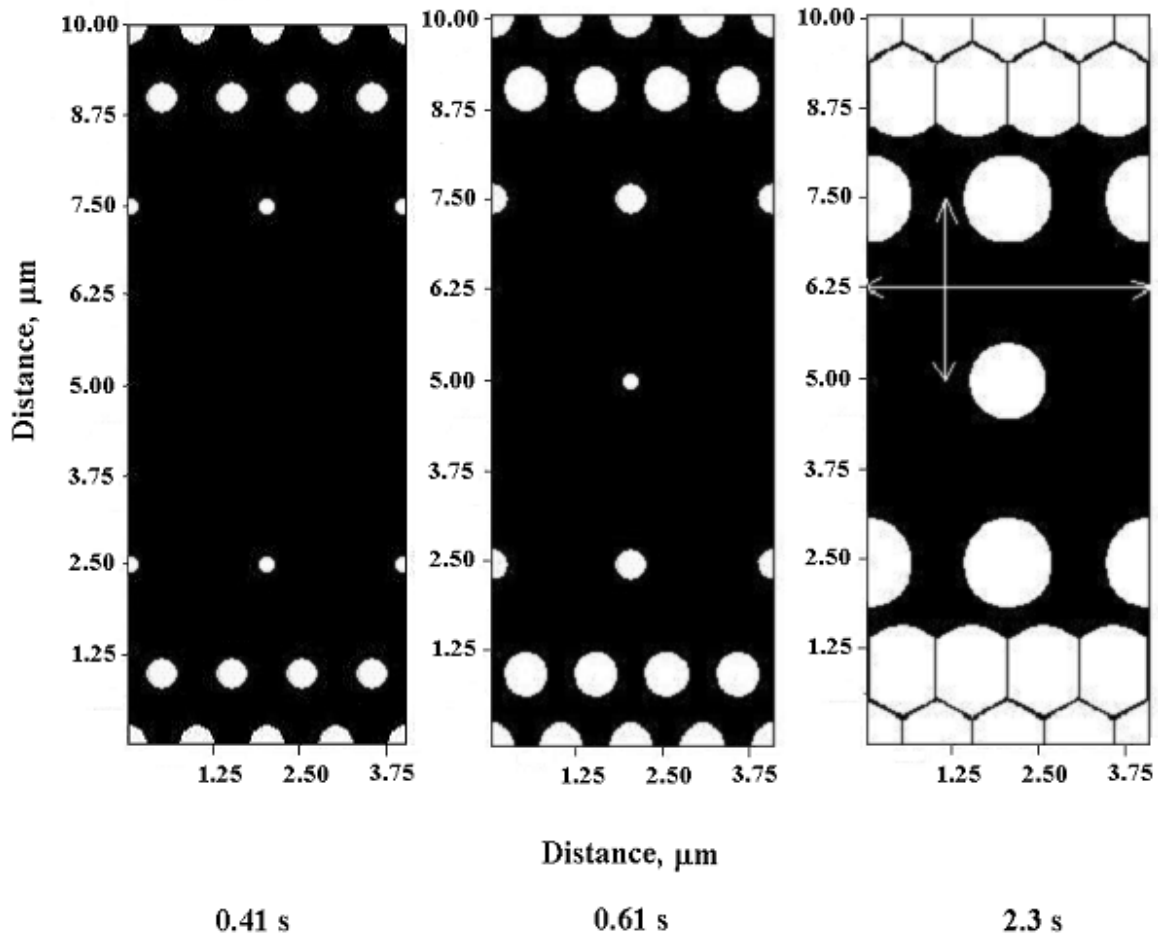


Figure 6.14: Simulated microstructure for “distributed nucleation 3” ($\mu_{\alpha\gamma}$ =nominal mobility, the arrows indicate the maximum area of austenite that has no ferrite nucleus).

In “distributed nucleation 3” there is a gradual increase of both interband distance and internucleus distance in a nuclei band from the prior austenite grain boundary to the grain centre. However, it might be possible that instead of these gradual changes there were sudden changes in these two parameters. This situation was simulated in “distributed nucleation 4” (**Figure 6.15**). Here, the grain boundary nuclei were introduced in the same fashion as was done for “distributed nucleation 3”. At 0.4 s an intragranular nucleation

band, with a nuclei density of 1 nucleus/ μm , was placed at a distance of 1 μm from the grain boundary. At 0.6 s another intragranular nucleation band was placed at a distance of 1 μm from the first intragranular nucleation band, with a density of 1 nucleus/ μm . Simultaneously (i.e. at 0.6 s) at a distance of 3 μm from the second intragranular nucleation band a third intragranular nucleation band was placed, with a density of 1 nucleus/ 4 μm .

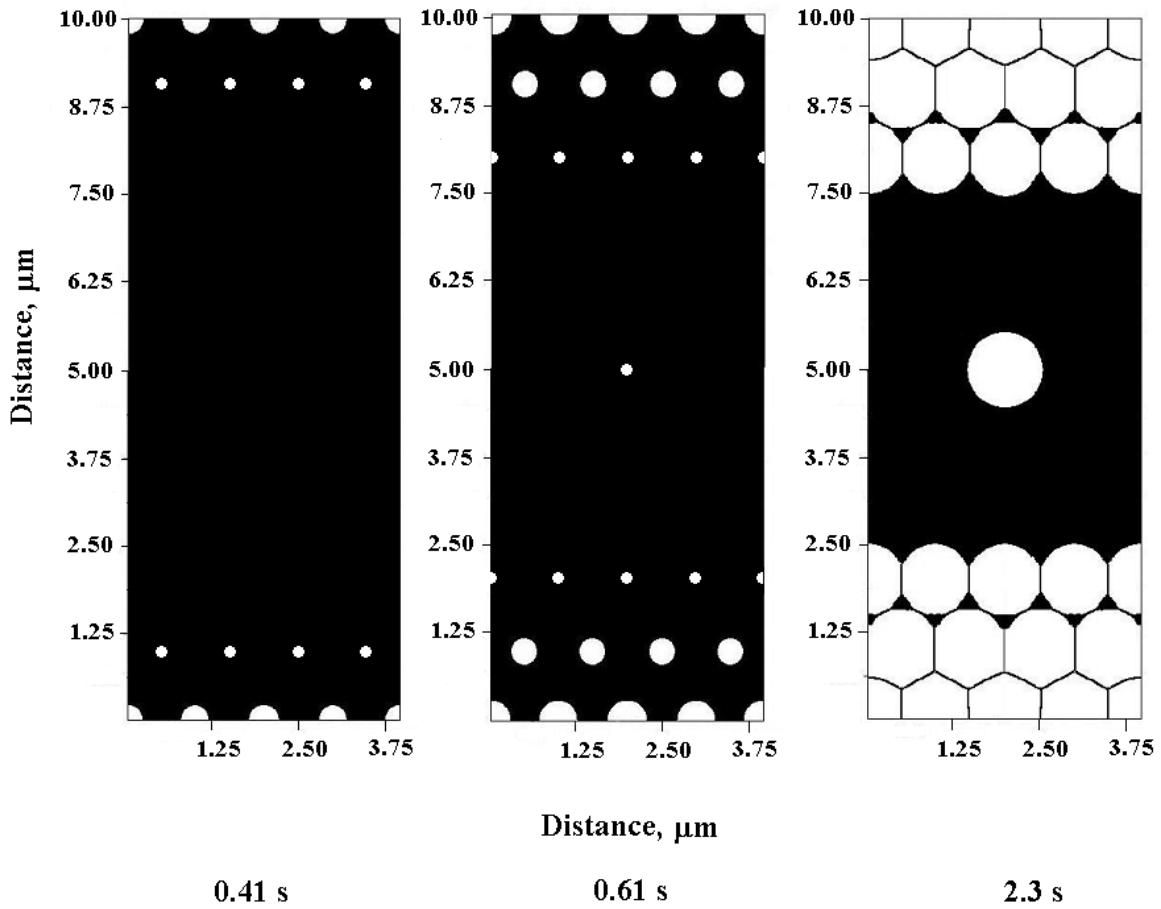


Figure 6.15: Simulated microstructure for “distributed nucleation 4” ($\mu_{\alpha\gamma}$ =nominal mobility).

“Distributed nucleation 5” was similar to “distributed nucleation 4” (**Figure 6.16**). The different assumption in this scheme was that the low-density intragranular nucleation band was placed closer to the high-density bands; the distance between the second and the third intragranular nucleation band was 1 μm .

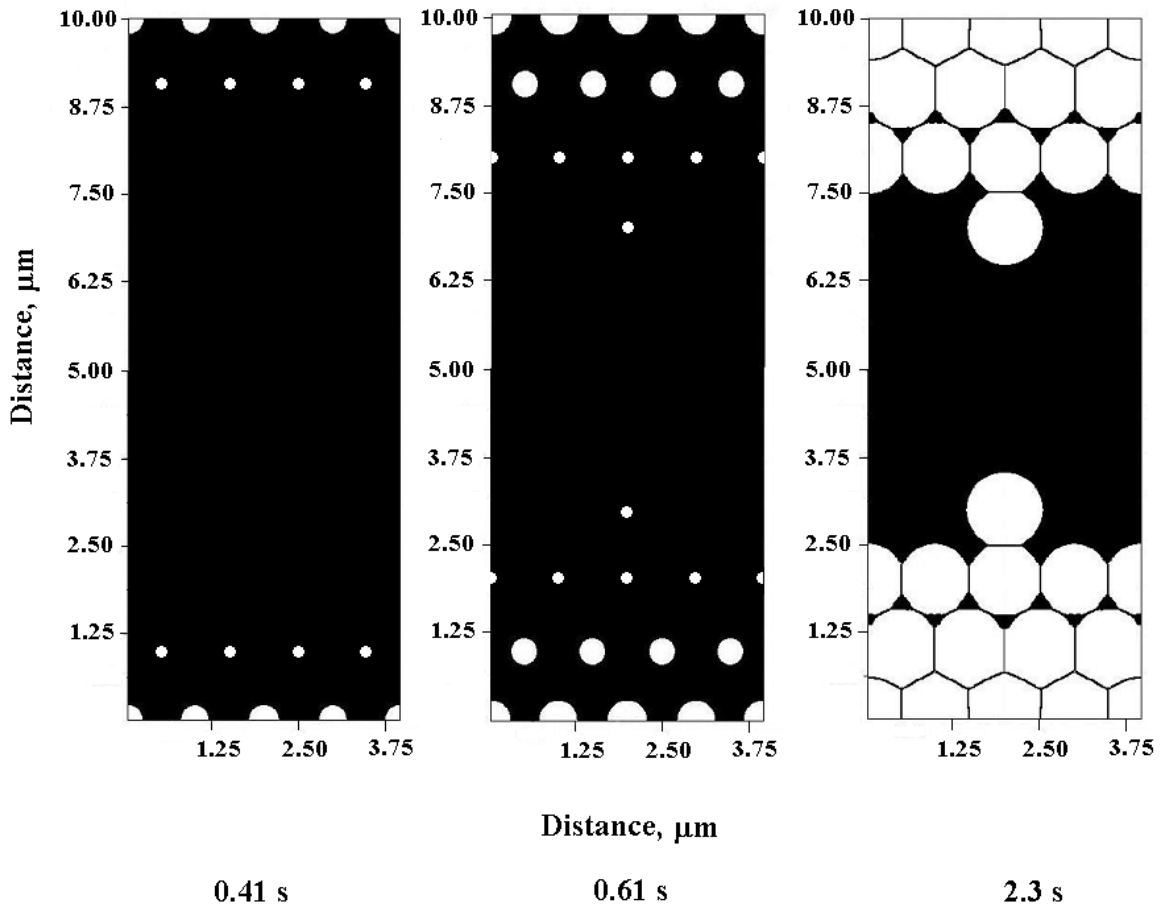


Figure 6.16: Simulated microstructure for “distributed nucleation 5” ($\mu_{\alpha\gamma}$ =nominal mobility).

Using the nominal mobility, the ferrite fractions obtained for the “distributed nucleations 1-5” were lower than that observed experimentally [**Table 6.3**]. For “distributed

nucleations 1-5”, the ferrite nuclei were gradually introduced with time such that these nuclei experienced a gradually decreased growth time. Further, the nuclei density in some areas of the “distributed nucleations 1-5” were lower than that used to determine the nominal mobility. These factors have contributed to the lower ferrite fractions obtained in the “distributed nucleations 1-5” as compared to the experimental one.

Table 6.3: Summary of results of “nominal nucleation” and “distributed nucleations” ($\mu_{\alpha\gamma}$ =nominal mobility)

Nucleation	Average nucleation time, s	Average nucleation density, μm^{-2}	Ferrite fraction	Ferrite formed during deformation	Ferrite formed after deformation	$d_{\alpha\beta}$, μm	Ratio of maximum and minimum ferrite grain size
Nominal nucleation	0	0.44	0.88	0.24	0.64	1.6	
Distributed nucleation 1	0.43	0.53	0.66	0.08	0.58	1.3	1.5
Distributed nucleation 2	0.33	0.40	0.52	0.09	0.43	1.3	1.2
Distributed nucleation 3	0.27	0.43	0.48	0.11	0.37	1.2	1.2
Distributed nucleation 4	0.45	0.53	0.5	0.06	0.44	1.1	1.2
Distributed nucleation 5	0.46	0.55	0.52	0.06	0.46	1.1	1.2

The average nucleation time for all nucleation scenarios are reported in **Table 6.3**. As the ferrite nucleus was introduced at the beginning of the deformation time, the average nucleation time for “nominal nucleation” is zero. From **Table 6.3** it is observed that the ferrite formed during deformation decreases with increase in average nucleation time. During this period there were no impingement of ferrite grains and the fraction of ferrite formed was dependent on the time of introduction of the ferrite nuclei.

The average ferrite nucleation density for all nucleation scenarios are also reported in **Table 6.3**. But no relationship was obtained between the ferrite fraction and the ferrite nucleation density. This was due to: (i) all the ferrite nuclei did not appear in the same time, (ii) there was always impingement of some of the ferrite grains.

The results in **Table 6.3** indicate a rather small spread in the grain sizes. Among them the largest spread has been obtained for “distributed nucleation 1”. In “distributed nucleation 1” the spread in ferrite grain size was only caused by the time distribution of the ferrite nuclei. This was due to the reason that the ferrite nuclei were evenly placed (with constant distance among them) in this simulation. In the rest of the nucleation scenarios, i.e., “distributed nucleations 2-5”, the effect of time distribution of the ferrite nuclei were countered by the spatial distribution of the nuclei. This could be explained by analyzing **Figure 6.15**. Although the ferrite grains at the prior austenite grain boundary were introduced at 0.2 s, due to spatial and time distribution of “distributed nucleation 4”, they could not grow larger than 1 μm in size. However, the grain in the centre had more space to grow and as a result it grew to similar size even though it was introduced at 0.6 s.

From **Table 6.3** it can be concluded that using the “nominal mobility” the “distributed nucleations 1-5” yielded ferrite fractions that were too low. In the next subsection the mobility values are adjusted to better replicate the experimental ferrite fraction.

6.3.3 “Distributed nucleations” and adjusted mobilities

For the adjusted mobilities the calculations were done for He quench only. **Table 6.4** summarizes the results for “distributed nucleations 1-5”.

Table 6.4: Summary of results of “distributed nucleations 1-5” with adjusted mobilities

Nucleation	Average nucleation time, s	Average nucleation density, μm^{-2}	Mobility (in units of CCT mobility)	Ferrite fraction	d_{α} , μm	Ratio of maximum and minimum ferrite grain size	Ferrite formed during deformation	Ferrite formed after deformation
Distributed nucleation 1	0.43	0.53	5.6	0.91	1.5	1.5	0.13	0.78
Distributed nucleation 2	0.33	0.40	9.4	0.90	1.7	1.4	0.26	0.64
Distributed nucleation 3	0.27	0.43	13.1	0.89	1.5	2.1	0.33	0.56
Distributed nucleation 4	0.45	0.53	18.8	0.89	1.4	3.3	0.26	0.63
Distributed nucleation 5	0.46	0.55	24.4	0.86	1.3	2.9	0.28	0.58

To match the observed ferrite fractions, the adjusted ferrite-austenite mobility values were 6 to 24 times larger than the CCT mobility.

In the present study the ferrite nuclei were placed in the austenite domain by hand. This was done following the underlying principles of ferrite nucleation during DIFT (for example, introduction of ferrite nucleation sites inside the prior austenite grain, ferrite nucleation during the deformation step, intragranular deformation bands acted as nucleation bands, etc.). The adjusted mobilities matched the ferrite fractions for “distributed nucleation” scenarios with the experimental one. The phase field model keeps track of hard and soft impingement of the growing ferrite grains. Some high-density nucleation bands were surrounded by other high-density nuclei bands or grain boundary nuclei in both directions (an example is the nucleation band 1 in “distributed nucleation 4”, **Figure 6.17**). While other high density nucleation bands were not surrounded like this in both directions (an example is the nucleation band 2 in “distributed nucleation 4”, **Figure 6.17**). As a result the nuclei at the nucleation band 2 grew larger than the nuclei at the nucleation band 1 (for adjusted mobility). However, the ferrite grain in the centre had grown even larger due to absence of impingement from other ferrite grains. These differences in ferrite growth created the ferrite grain size spread. The ferrite grain size spreads for the “distributed nucleations 2-5” are reported in **Table 6.4**. “Distributed nucleation 4” had the largest ferrite grain size spread (the ratio of the maximum and minimum ferrite grain size being 3.3). The average ferrite grain size was very close to the experimental one for all “distributed nucleations”.

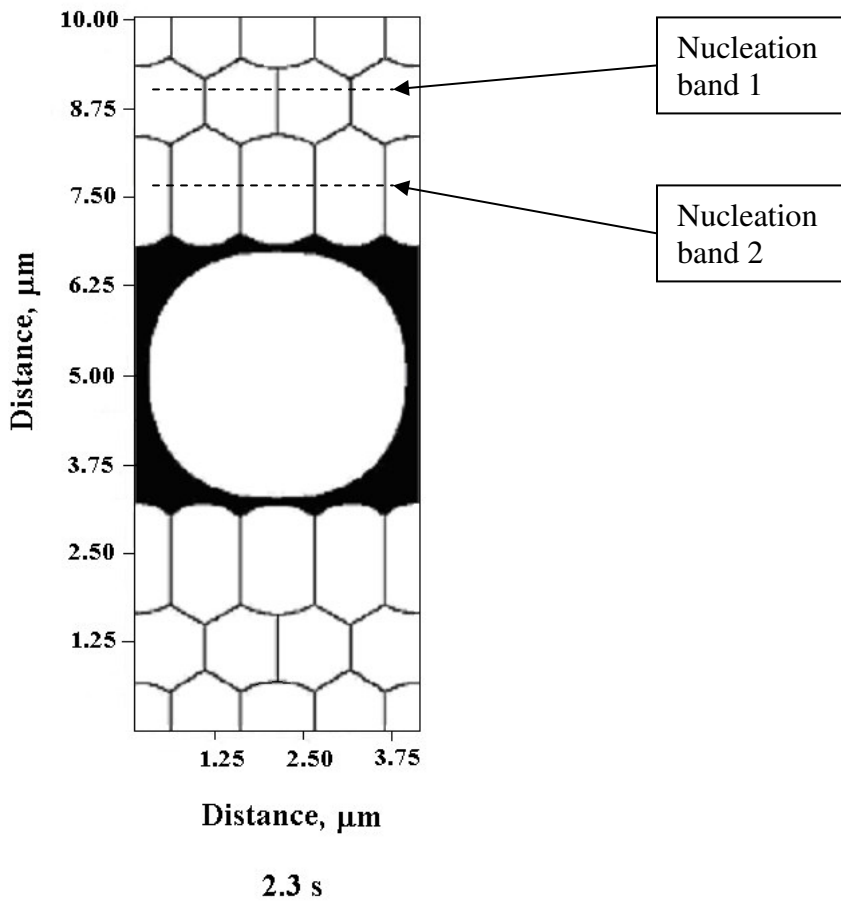


Figure 6.17: Simulated microstructure for “distributed nucleation 4” ($\mu_{\alpha\gamma}=5\times$ nominal mobility).

The ferrite formed during and after deformation is reported in **Table 6.4**. It is observed that for simulations with similar average nucleation time (“distributed nucleations 1, 4 and 5”) the ferrite formed during deformation increases with increase in the adjusted mobility value. A relationship between average nucleation density and adjusted mobility value was difficult to obtain due to the impingement of ferrite grains. A substantial

amount of ferrite was formed after deformation. For “distributed nucleations 2-5” approximately two-third of the total ferrite fraction was formed after deformation.

6.4 Discussion

For calculations with the nominal mobility value all ferrite grains reached sizes in the range of approximately 1 – 1.5 μm regardless of nucleation distribution detail. Per definition, the maximum grain size was 1.6 μm as obtained in “nominal nucleation”. In the “distributed nucleations”, ferrite grains were smaller either due to impingement in areas of high nuclei density (1 nucleus/ μm) or due to limited growth time for delayed introduction when no impingement was observed in areas of lower nuclei density. This restricted the spread of ferrite grain sizes for nominal mobility. For larger mobilities the ferrite nuclei that were low in spatial density grew to grain sizes of 3 to 4 μm . This created the larger ferrite grain size spread for larger mobilities.

A trend was obtained between the adjusted mobility value and the product of the average nucleation time and the maximum area of austenite that did not contain a ferrite nucleus [Table 6.5]. This area is defined as the product of two distances as shown by two arrows in Figure 6.14.

Table 6.5: Results of adjusted mobility values with nucleation parameters

Nucleation	Average nucleation time×maximum area of austenite that does not contain a ferrite nucleus, s μm^2	Adjusted mobility (in units of nominal mobility)
Distributed nucleation 1	0.81	1.5
Distributed nucleation 2	1.24	2.5
Distributed nucleation 3	2.7	3.5
Distributed nucleation 4	5.4	5
Distributed nucleation 5	7.36	6.5

From **Table 6.5** it is observed that the adjusted mobility value increases with the value of the product of average nucleation time and maximum area of austenite that did not contain a ferrite nucleus.

The adjusted ferrite-austenite mobility values in this study were found to be 6 to 24 times larger than the CCT mobility. This increase in the effective mobility for DIFT can be preliminarily attributed to,

- (i) the presence of fast diffusion paths,
- (ii) the formation of excess vacancies due to deformation and the associated increase in diffusion coefficients thereby reducing solute drag,

(iii) the simplified assumptions regarding the effective austenite grain size; a substantial ferrite formation occurs after deformation when the effective austenite grain size would be 7 μm rather than the 10 μm that was assumed in this model. Then, the higher effective mobility obtained in this study was partly due to larger effective austenite grain size used in the model.

In addition, it has to be considered that all these mobility values were indirectly concluded, i.e. there was no direct measurement of the interface velocity. Attempts should be made to experimentally measure the ferrite-austenite interface velocity, before making definite conclusions about the increase in interface mobility during DIFT.

From the simulated microstructures it was observed that the ferrite grains in the prior austenite grain boundary region did not have any entrapped austenite in between them. This fact was verified by changing the node size and time stepping. This could be attributed to the dissolution of very fine austenitic regions in between the fine grained ferrites at high temperature. This was explained through the example of “distributed nucleation 3” employing 3.5 \times nominal mobility. **Figure 6.18** shows the micrograph at 0.55 s. **Figure 6.19** shows the carbon profile along the line shown in **Figure 6.18**.

From **Figure 6.19** it is observed that there is a slope in the carbon profile inside the ferrite grains as indicated by the solid arrows. The reason for this is the difference in interfacial carbon concentration in different parts of the ferrite grain. The mixed mode nature of the phase field model creates this varying interfacial carbon concentration. The interfacial carbon concentration is lower in that portion of the grain, where there is more space for the carbon to diffuse away in the parent austenite. The slope in the carbon concentration

within the ferrite grain helps in diffusing away the carbon from entrapped austenite to the bigger austenitic regions via a rather short diffusion distance ($\sim 1 \mu\text{m}$). As a result, the entrapped austenite islands are depleted in carbon and eventually transform to ferrite. The carbon profile shown in **Figure 6.19** contains two humps, as indicated by the dotted arrows. These humps have been created by the carbon rejected from the nearby ferrite grains (i.e. the ferrite grains indicated by the white arrows in **Figure 6.18**).

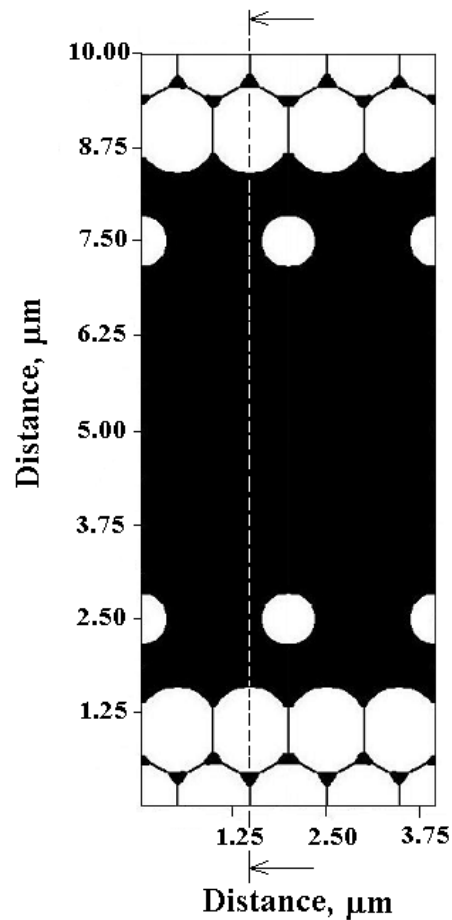


Figure 6.18: Simulated microstructure for “distributed nucleation 3” at 0.55 s, $\mu_{\alpha\gamma} = 3.5 \times \text{nominal mobility}$.

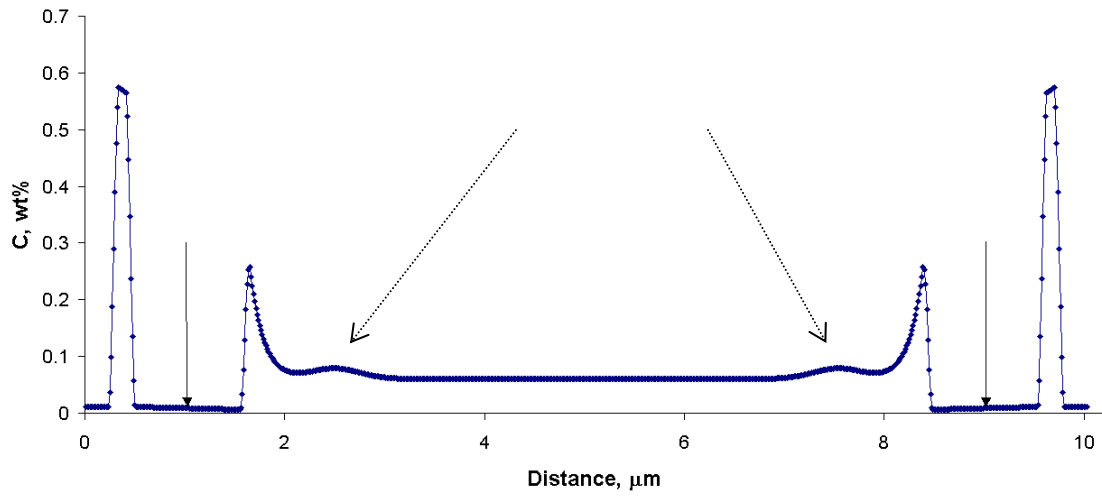


Figure 6.19: Carbon profile along the line shown in **Figure 6.18**.

7. Conclusions

1. DIFT can be successfully applied to form ultrafine ferritic structure for all investigated chemistries provided suitable processing conditions are applied.
2. DIFT produces finer ferrite grain sizes compared to conventional DP microstructures with similar martensite fraction.
3. Increasing the amount of strain increases the potential for DIFT. However, after a strain of 0.55 in axisymmetric compression there is a marginal change in the final microstructure with increase in strain.
4. For all chemistries increasing the deformation temperature from 25 to 50°C above the A_{r3} , shows insignificant effect on the final ferrite grain size. The major effect of increasing the deformation temperature is a decrease in ferrite fraction by approximately 0.1.
5. For the Mo steel a predominantly ultrafine ferrite microstructure is obtained from all prior austenitic grain sizes studied (13-27 μm).
6. Even though prior austenite grain sizes have not been quantified in detail for the plain carbon steel, the production of UFF in Gleeble and torsion simulations with different

processing in the austenite region suggests that also for this steel a range of prior austenite grain sizes can be used to obtain suitable DIFT microstructures.

7. Rapid cooling, e.g. 100°C/s, is key for the plain carbon steel after the DIFT deformation step to obtain martensite as secondary transformation product thereby attaining the desired fine-grained dual phase microstructure.

8. Both plain C and Mo steels appear to be potential candidates for industrial production, since moderate changes in deformation temperature and austenite grain size result in similar UFF fractions which will be well suited for designing a reasonably stable industrial processing window.

Austenite to ferrite transformation for DIFT processing conditions has been modelled. The adjustable parameters were time, and spatial distribution of ferrite nuclei, and the austenite-ferrite interface mobility ($\mu_{\gamma\alpha}$). Two parameters were used to describe the spatial distribution of DIFT ferrite nuclei; internucleus distance in a nuclei band, and distance between two nuclei bands. “Distributed nucleation 4” gave the largest ferrite grain size spread among all the schemes studied. A dense ferrite nucleation in the prior austenite grain boundary region and a less dense ferrite nucleation elsewhere is the most probable cause of ferrite grain size distribution. And this change in nucleation density is sharp from prior austenite grain boundary to grain centre (i.e. not a gradual change as seen in “distributed nucleation 3”).

Novelty of the work

The novel contributions of the presented work can be summarized as:

1. Extending the concept of ultra fine ferrite by DIFT to dual phase steels.
2. Systematic analysis of the effects of deformation temperature, strain, chemistry, and prior austenite grain size on DIFT.
3. Laboratory simulation of hot strip rolling schedule with DIFT pass to produce ultra fine grained dual phase steel.
4. Development of first generation model to describe DIFT.

Future work

1. It would be particularly attractive to produce an UFG DP steel using a simple plain carbon steel. Thus, further evaluation of DIFT should emphasize the plain C steel where there is still a systematic study required on the effect of the initial austenite microstructure on DIFT.
2. The proposal of applying DIFT in a separate rolling stand located in the run-out table area would require to have a substantially altered mill design. Thus, it will be useful to further evaluate in detail whether or not DIFT can be achieved in the final stands of the

finish mill by a combination of proper interstand cooling and asymmetric rolling. A promising approach appears to be a combination of experimental work employing a laboratory scale asymmetric rolling mill with modelling the through thickness distributions of strain, temperature and microstructure.

3. The proposed model for DIFT requires further critical evaluation with experimental observations thereby enabling model improvements. Austenite to ferrite transformation modelling should be conducted with a larger calculation matrix (at par to the area for the experimental analysis). This will also include the distribution of prior austenite grain size. These calculations will permit to obtain a ferrite grain size distribution with statistical relevance. Further simulations will have to be performed for a variety of steel chemistries and conditions that lead to incomplete UFF microstructures. In particular, the latter may give new insight into the ferrite formation mechanisms. Eventually, the present transformation model will have to be coupled with a deformation model to advance the understanding of DIFT.

4. Current metallographic techniques are unsuitable for determining the fraction of ferrite formed during as opposed to after deformation in a DIFT schedule. In-situ techniques can be explored to capture DIFT and laser-ultrasonics appears to be a potential choice in this regard. However, one of the challenges associated with using the laser-ultrasonic technique is to redesign sample and test set-up so that deformation and ferrite formation are uniform throughout the sample.

References

1. M. Niikura, M. Fujioka, Y. Adachi, A. Matsukura, T. Yokota, Y. Shirota and Y. Hagiwara, *Journal of Materials Processing Technology*, 2001, vol. 117, pp. 341.
2. Y. D. Huang and L. Froyen, *Journal of Materials Processing Technology*, 2002, vol. 124, pp. 216.
3. P. D. Hodgson, M. R. Hickson, and R. K. Gibbs, *Scripta Materialia*, 1999, vol. 40, No. 10, pp. 1179.
4. S. C. Hong, S. H. Lim, K. J. Lee, D. H. Shin, and K. S. Lee, *ISIJ International*, 2003, vol. 43, pp. 394
5. Z. Yang, Y. Zhao, Q. Chen, H. Gao, R. Wang, and Y. Ma, *42nd MWSP Conference Proceedings*, ISS, Warrendale, PA, 2000, vol. 38, pp. 505.
6. J. Shaw, B. Engl, C. Espina, E. C. Oren, and Y. Kawamoto, *New Steel Sheets and Steel Bar Products and Processing*, SAE-SP 1685, Ed. D. W. Anderson et al., SAE, Warrendale, PA, 2002, pp. 63.
7. Y. I. Son, Y. K. Lee, K. T. Park, C. S. Lee, and D. H. Shin, *Acta Materialia*, 2005, vol. 53, pp. 3125-3134.
8. M. R. Hickson, P. J. Hurley, R. K. Gibbs, G. L. Kelly, and P. D. Hodgson: *Metallurgical and Materials Transactions A*, 2002, vol. 33A, pp. 1019.

9. P. Petkov, M.A.Sc. Thesis, The University of British Columbia, Vancouver, Canada, 2004.
10. E. Essadiqi, M. G. Akben, and J. J. Jonas, *Phase Transformations in Ferrous Alloys*, eds. A. R. Marder, and J. I. Goldstein, The Metallurgical Society of AIME, Philadelphia, Pa, U.S.A., 1983, pp. 391.
11. L. E. Collins, J. R. Barry, and J. D. Boyd, *Phase Transformations in Ferrous Alloys*, eds. A. R. Marder, and J. I. Goldstein, The Metallurgical Society of AIME, Philadelphia, Pa, U.S.A., 1983, pp. 397.
12. D. M. Fegredo, J. D. Boyd, and M. J. Stewart, *HSLA Steels Technology and Applications*, ed. M. Korchinsky, ASM, Philadelphia, Pa, U.S.A., 1983, pp. 95.
13. F. Zhang, and J. D. Boyd, *Phase Transformation During the Thermal/Mechanical Processing of Steel*, ed. E. B. Hawbolt, and S. Yue, The Metallurgical Society of CIM, Montreal, PQ, Canada, 1995, pp. 147.
14. V. M. Khlestov, E. V. Konopleva, and H. J. McQueen, *Canadian Metallurgical Quarterly*, 1996, vol. 35, pp. 169.
15. Y. I. Son, Y. K. Lee, K. T. Park, C. S. Lee, and D. H. Shin, *Acta Materialia*, 2005, vol. 53, pp. 3125-3134.

16. P. D. Hodgson, M. R. Hickson, and R. K. Gibbs, *Materials Science Forum*, 1998, vol. 284-286, pp. 63.
17. D. K. Matlock, F. Zia-Ebrahimi, and G. Krauss, *Deformation, Processing and Structure*, ed. G. Krauss, ASM, Metals Park, Oh, U.S.A, 1984, pp. 47.
18. G. R. Speich and R. L. Miller, *Structure and Properties of Dual-Phase Steel*, R. A. Kot and J. W. Morris, (Eds.), The Metallurgical Society of AIME, Warrendale, PA, U.S.A., 1979, pp. 145.
19. M. Militzer, and W. J. Poole, *Advanced High Strength Sheet Steels for Automotive Applications Proceedings*, AIST, Warrendale, PA, U.S.A., 2004, pp. 219.
20. R. Roumina, and C. W. Sinclair, *Metallurgical and Materials Transactions A*, 2008, vol. 39, pp. 2495.
21. T. Morimoto, I. Chikushi, R. Kurahashi, and J. Yanagimoto: *Proc. of TMP 2004 : 2nd Intl. Conf. on Thermomechanical Processing of Steels*, Stahleisen Verlag GmbH, Düsseldorf, Germany, 2004, pp. 415.
22. R. Ueji, N. Tsuji, Y. Minamino, and Y. Koizumi, *Acta Materialia*, 2002, vol. 50, pp. 4177.

23. H. Azizi-Alizamini, C. W. Sinclair, M. Militzer, and J.D. Mithieux, *Materials Science Forum*, 2007, vols. 558-559, pp. 113.
24. R. Ueji, N. Tsuji, Y. Minamino, and Y. Koizumi, *Science and Technology of Advanced Materials*, 2004, vol. 5, pp. 153.
25. D. H. Shin, I. Kim, J. Kim, and K. Park, *Acta Materialia*, 2001, vol. 49, pp. 1285.
26. B. Hwang, Y. G. Kim, S. Lee, D. Y. Hwang, and D. H. Shin, *Metallurgical and Materials Transactions A*, 2007, vol. 38A, pp. 3007.
27. A. Najafi-Zadeh, J. J. Jonas, and S. Yue, *Metallurgical Transactions A*, 1992, vol. 23A, pp. 2607.
28. H. Beladi, G. L. Kelly, and P. D. Hodgson, *Metallurgical and Materials Transactions A*, 2007, vol. 38A, pp. 450.
29. H. Yada, Y. Matsumura and K. Nakazima; United States Patent No. – 4466842, August 21, 1984.
30. P. J. Hurley, and P. D. Hodgson, *Materials Science and Engineering A*, 2001, vol. A 302, pp. 206.
31. G. L. Kelly, H. Beladi, and P. D. Hodgson, *ISIJ International*, 2002, vol. 42, pp. 1585.

32. P. D. Hodgson, and H. Beladi, *Materials Science Forum*, 2004, vols. 467-470, pp. 1137.
33. M. R. Barnett, G. L. Kelly, and P. D. Hodgson, *Metallurgical and Materials Transactions A*, 2002, vol. 33A, pp. 1893.
34. T. Morimoto, F. Yoshida, I. Chikushi, and J. Yanagimoto, *ISIJ International*, 2007, vol. 47, pp. 1475.
35. H. Beladi, G. L. Kelly, A. Shokouhi, and P. D. Hodgson, *Materials Science and Engineering A*, 2004, vol. A 367, pp. 152.
36. J. Choi, D. Seo, J. Lee, K. Um, and W. Choo, *ISIJ International*, 2003, vol. 43, pp. 746.
37. H. Beladi, G.L. Kelly, A. Shokouhi, and P. D. Hodgson: *Materials Science and Engineering A*, 2004, vol. A 371, pp. 343.
38. S. C. Hong, S. H. Lim, H. S. Hong, K. J. Lee, D. H. Shin, and K. S. Lee, *Materials Science and Engineering A*, 2003, vol. A 355, pp. 241.
39. S. C. Hong, and K. S. Lee, *Materials Science and Engineering A*, 2002, vol. A 323, pp. 148.

40. J. Cho, D. Suh, J. Kang, and H. Lee, *Ultrafine Grained Materials II*, Y. T. Zhu, T. G. Langdon, R. S. Mishra, S. L. Semiatin, M. J. Saran, and T. C. Lowe, (Eds.), TMS, 2002, pp. 259.
41. D. A. Porter, and K. E. Easterling, *Phase Transformations in Metals and Alloys*, Chapman and Hall, 1992.
42. R. Bengochea, B. Lopez, and I. Gutierrez, *Metallurgical and Materials Transactions A*, 1998, vol. 29A, pp. 417.
43. T. Kvackaj, and I. Mamuzic, *ISIJ International*, 1998, vol. 38, pp. 1270.
44. P. J. Hurley, B. C. Muddle, and P. D. Hodgson, *Metallurgical and Materials Transactions A*, 2001, vol. 32A, pp. 1507.
45. D. Suh, C. Oh, and S. Kim, *Metallurgical and Materials Transactions A*, 2005, vol. 36A, pp. 1057.
46. S. Genda, H. Takahashi, Y. Kogo, S. Torizuka, and K. Nagai, *CAMP-ISIJ*, 2000, vol. 13, pp. 1187.
47. S. Torizuka, and K. Nagai, *CAMP-ISIJ*, 2003, vol. 16, pp. 604.
48. D. Suh, J. Cho, and K. Nagai, *Metallurgical and Materials Transactions A*, 2004, vol. 35A, pp. 3399.

49. Y. Matsumura, and H. Yada: *Transactions ISIJ*, 1987, vol. 27, pp. 492.
50. H. Yada, Y. Matsumura, and T. Senuma: *Thermec '88-International Conference on Physical Metallurgy of Thermomechanical Processing of Steels and Other Metals*, I. Tamura, ed., The Iron and Steel Institute of Japan, Tokyo, Japan, 1988, pp.200.
51. C. M. Li, H. Yada, and H. Yamagata: *Scripta Materialia*, 1998, vol. 39, pp. 963.
52. H. Dong, and X. Sun, *Current Opinion in Solid State and Materials Science*, 2005, vol. 9, pp. 269.
53. C. Zheng, D. Li, S. Lu, and Y. Li, *Scripta Materialia*, 2008, vol. 58, pp. 838.
54. E. I. Poliak, and J. J. Jonas, *Acta Materialia*, 1996, vol. 44, pp. 127.
55. C. R. Hutchinson, H. S. Zurob, C. W. Sinclair, and Y. J. M. Brechet, *Scripta Materialia*, 2008, vol. 59, pp. 635
56. M. R. Hickson, R. K. Gibbs, and P. D. Hodgson, *ISIJ International*, 1999, vol. 39, pp. 1176.
57. A. N. Kolmogorov, *Izv. Akademii nauk USSR ser. matemat*, 1937, vol. 1, pp. 355.

58. W. A. Johnson, and R. F. Mehl, *Transactions AIME*, 1939, vol. 135, pp. 416.
59. M. Avrami, *Journal of Chemical Physics*, 1939, vol. 7, pp. 1103.
60. M. Avrami, *Journal of Chemical Physics*, 1940, vol. 8, pp. 212.
61. M. Avrami, *Journal of Chemical Physics*, 1941, vol. 9, pp. 177.
62. M. Unemoto, N. Komatsubara, I. Tamura, *Journal of Heat Treating*, 1980, vol. 1, pp.
63. M. Militzer, E. B. Hawbolt, and T. R. Meadowcroft, *Metallurgical and Materials Transactions A*, 2000, vol. 31A, pp. 1247.
64. R. G. Kamat, E. B. Hawbolt, L. C. Brown, and J. K. Brimacombe, *Metallurgical Transactions A*, 1992, vol. 23A, pp. 2469.
65. E. Scheil, *Arch. Eisenhüttenwesen*, 1935, vol. 8, pp. 565.
66. J. W. Christian, *The Theory of Transformations in Metals and Alloys*, 2nd edition, Pergamon press, 1975.
67. M. Tong, J. Ni, Y. Zhang, D. Li, and Y. Li, *Metallurgical and Materials Transactions A*, 2004, vol. 35A, pp. 1565.

68. C. Atkinson, H. B. Aaron, K. R. Kinsman, and H. I. Aaronson, *Metallurgical Transactions*, 1973, vol. 4, pp. 783.
69. J. R. Bradley, J. M. Rigsbee, and H. I. Aaronson, *Metallurgical Transactions A*, 1977, vol. 8A, pp. 323.
70. F. Fazeli, and M. Mililtzer, *44th MWSP Conference Proceedings*, ISS, 2002, vol. 40, pp. 1117.
71. S. Kundu, M. Dutta, S. Ganguly, and S. Chandra, *Scripta Materialia*, 2004, vol. 50, pp. 891.
72. L. Zhang, C.B. Zhang, Y.M. Wang, X.H. Liu, and G.D. Wang, *Journal of Materials Research*, 2002, vol. 17, no. 9, pp. 2251.
73. M. Militzer, R. Pandi, and E. B. Hawbolt, *Metallurgical and Materials Transactions A*, 1996, vol. 27A, pp. 1547.
74. T. A. Kop, Y. van Leeuwen, J. Siestma, and S. van der Zwaag, *ISIJ International*, 2000, vol. 40, pp. 713.
75. J. Svoboda, F. D. Fischer, and E. Gamsjager, *Acta Materialia*, 2002, vol. 50, pp. 967.
76. G. R. Purdy, and Y. J. M. Brechet, *Acta Metallurgica et Materialia*, 1995, vol. 43, pp. 3763.

77. M. Enomoto, *Acta Materialia*, 1999, vol. 47, pp. 3533.
78. M. Hillert, *Acta Materialia*, 1999, vol. 47, 4481.
79. G. P. Krielaart, J. Sietsma, and S. van der Zwaag, *Materials Science and Engineering A*, 1997, vol. A237, pp. 216.
80. F. Fazeli and M. Militzer, *Metallurgical and Materials Transactions A*, 2005, vol. 36A, pp. 1395.
81. J. Sietsma, and S. van der Zwaag, *Acta Materialia*, 2004, vol. 52, pp. 4143.
82. M. Militzer, M. G. Meozzi, J. Sietsma, and S. van der Zwaag, *Acta Materialia*, 2006, vol. 54, pp. 3961.
83. M. G. Meozzi, J. Sietsma, S. van der Zwaag, M. Apel, P. Schaffnit, and I. Steinbach, *Metallurgical and Materials Transactions A*, 2005, vol. 36A, pp. 2327.
84. D. H. Yeon, P. R. Cha, and J. K. Yoon, *Scripta Materialia*, 2001, vol. 45, pp. 661.
85. I. Loginova, J. Agren, and G. Amberg, *Acta Materialia*, 2004, vol. 52, pp. 4055.
86. C. J. Huang, D. J. Browne, and S. McFadden, *Acta Materialia*, 2006, vol. 54, pp. 11.

87. Y.J. Lan, D.Z. Li, and Y.Y. Li, *Journal of Materials Research*, 2004, vol. 19, pp. 2877.

88. I. Steinbach, and M. Apel, *Advances in Materials Theory and Modelling: Bridging over Multiple Length and Time Scales*. San Francisco (CA): Materials Research Society; 2001, pp. AA7.14.

89. M. Militzer, *ISIJ International*, 2007, vol. 47, pp. 1.

90. R. A. Vandermeer, *Acta Metallurgica et Materialia*, 1990, vol. 38, pp. 2461.

91. S. M. Allen, and J. W. Cahn, *Acta Metallurgica*, 1979, vol. 27, pp. 1085.

92. I. Steinbach, F. Pezzolla, B. Nestler, M. Seesselberg, R. Prieler, G. J. Schmitz, and J. L. L. Rezende, *Physica D*, 1996, vol. 94, pp. 135.

93. M. G. Meozzi, M. Militzer, J. Sietsma, and S. Van Der Zwaag, *Metallurgical and Materials Transactions A*, 2008, vol. 39A, pp. 1237.

94. H. Mecking, and U. F. Kocks, *Acta Metallurgica*, 1981, vol. 29, 1865.

95. M. Umemoto, Z. H. Guo, and I. Tamura, *Materials Science and Technology*, 1987, vol. 3, pp. 249.

96. D. Liu, F. Fazeli, and M. Militzer: *ISIJ International*, 2007, vol. 47, pp. 1789.
97. S.S. Hazra, M.A.Sc. Thesis, The University of British Columbia, Vancouver, Canada, 2005.
98. Annual Book of ASTM Standards, *ASTM International*, Pa, U.S., 2004, vol. 3.01, E 112-96, pp. 227.
99. D. Hall, and J. Worobec, *Phase transformations during the thermal/mechanical processing of steel*, Metallurgical society of CIM, Montreal, PQ, Canada, 1996, pp. 305.
100. Annual Book of ASTM Standards, *ASTM International*, Philadelphia, Pa, U.S., 2000, vol. 3.01, E 384-99, pp. 437.
101. D. Tabor, *The Hardness of Metals*, Oxford, Clarendon Press, 1951.
102. M. Mazinani, and W. J. Poole: *Metallurgical and Materials Transactions A*, 2007, vol. 38A, pp. 328.
103. K. Mukherjee, S. Hazra, and M. Militzer: *Proceedings of SAE 2006 World Congress*, SAE International, SP-2035, Detroit, MI, 2006, pp. 81.

104. K. Mukherjee, S. Hazra, P. Petkov, and M. Militzer: *Materials and Manufacturing Processes*, 2007, vol. 22, pp. 511.
105. F. Fazeli, Ph. D. Thesis, The University of British Columbia, Vancouver, Canada, 2005.
106. M. Unemoto, H. Ohtsuka, and I. Tamura, *Transactions ISIJ*, 1983, vol. 23, pp. 775.
107. S. Lacroix, Y. Brechet, M. Veron, D. Quidort, M. Kandel, and T. Iung, *Materials Science and Technology 2003 Conference Proceedings*, Section Austenite Formation and Decomposition, ISS and TMS, Warrendale, Pa, U.S.A, 2003, pp. 367.
108. M. G. Mecozzi, J. Sietsma, S. van der Zwaag, M. Apel, P. Schaffnit, and I. Steinbach, *Material Science and Technology 2003, Austenite Formation and Decomposition*, Chicago, IL, Iron and Steel Society, TMS 2003, pp. 353.
109. Handbook of Chemistry and Physics, CRC Press Inc. Boca Raton, 1989.
110. Y. H. Bae, J. S. Lee, J.-K. Choi, W.-Y. Choo, and S. H. Hong, *Materials Transactions*, 2004, vol. 45, pp. 137.

Appendix 1

Figure A1.1 shows a schematic CCT diagram for steel with low and/or medium carbon levels ($< 0.7\text{wt}\%$). The thick lines indicate the continuous cooling phase transformation. The thin lines represent the cooling curves. Ae_3 is the temperature above which austenite is the stable phase, Ae_1 is the eutectoid temperature, i.e. the equilibrium temperature for pearlite formation and M_s is the martensite start temperature.

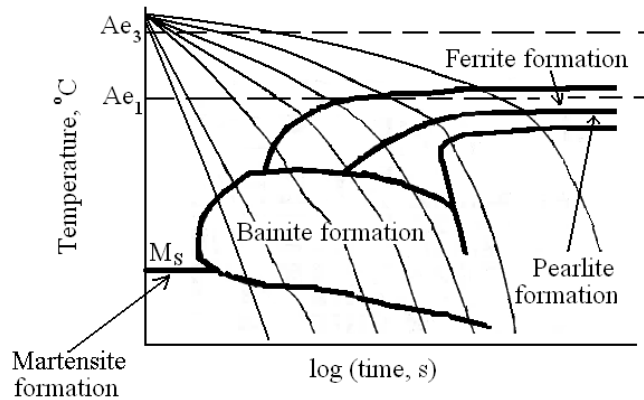


Figure A1.1: Schematic CCT diagram for low/medium carbon steel.

Appendix 2

Analysis of EBSD maps

The analysis of the EBSD maps is described using the example of the Mo steel shown in **Figure 5.12 (a)**. **Figure A2.1** shows the original EBSD map. In all of the **Appendix 2** figures the colours indicate the crystal direction parallel to the compression direction of the samples (colour coding is shown in **Figure 5.12**), unless mentioned otherwise. The unindexed white pixels indicate either a non-ferritic phase or a grain boundary region. In analyzing these as-obtained maps, unindexed points were extrapolated to indexed points by standard Channel 5 technique (**Figure A2.2**). This clean-up step involved in sequence a 8 neighbour extrapolation, a 7 neighbour extrapolation, and again another 8 neighbour extrapolation. Then objects were determined based on a selected critical misorientation, e.g. 2° (**Figure A2.3**). In **Figure A2.3** the objects are shown in random colours.

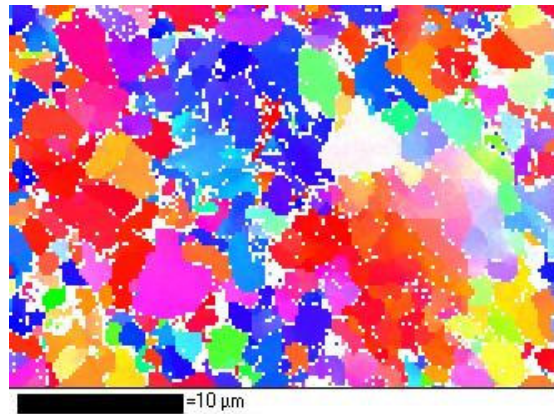


Figure A2.1: Original EBSD map for Mo steel.

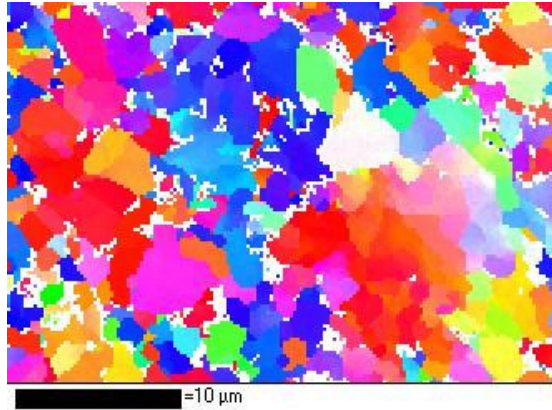


Figure A2.2: Map obtained after cleaning of map shown in **Figure A1.1**.

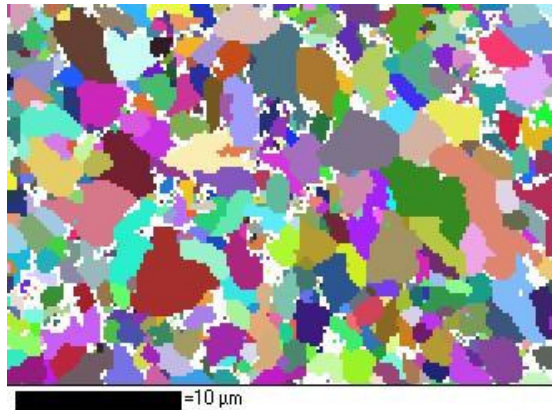


Figure A2.3: Object determined based on critical misorientation of 2° for map shown in **Figure A2.2**.

One of the challenges is that ferrite and martensite have a similar crystal structure that cannot be crystallographically distinguished based on EBSD. However, band contrast can be used to separate the two phases. Band contrast indicates the sharpness of the Kikuchi pattern obtained from the diffraction of the incident electron beam. A deviation from the perfect crystalline structure will result in diffused Kikuchi pattern with a low band

contrast value. Since martensite is inherently a more defect-containing structure as compared to ferrite, it is expected to have a lower band contrast. Hutchinson et al. [1] and Waterschoot et al. [2] utilized a similar parameter, IQ (image quality), to distinguish ferrite from other transformation products. But, Zaefferer et al. [3] argued that using high resolution FEG SEM results in similar pattern quality for ferrite and bainite. The band contrast distribution for the present EBSD map is shown in **Figure A2.4**. Clearly, a shoulder in the distribution is visible indicating that two different object types contribute to this distribution.

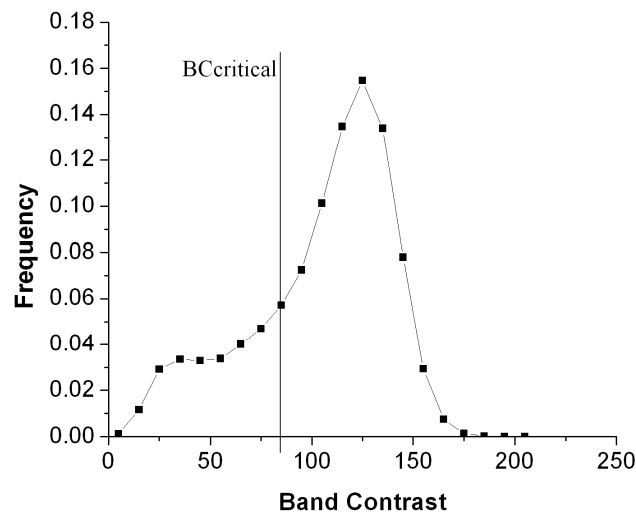


Figure A2.4: Band contrast distribution with $BC_{critical}$ for the EBSD map of Mo steel.

To classify objects, the mean band contrast of each object was determined (**Figure A2.5**). A critical mean band contrast ($BC_{critical}$) was determined such that objects having a mean band contrast above $BC_{critical}$ were considered to be ferrite and the rest could be considered as martensite. No general, independent value of $BC_{critical}$ could be established

as band contrast also depends on sample preparation. Thus, the martensite fraction determined from conventional SEM was used to quantify $BC_{critical}$ such that the total martensite fraction obtained in conventional SEM studies was equal to the sum of the fraction of non-indexed points and the fraction of objects below $BC_{critical}$.

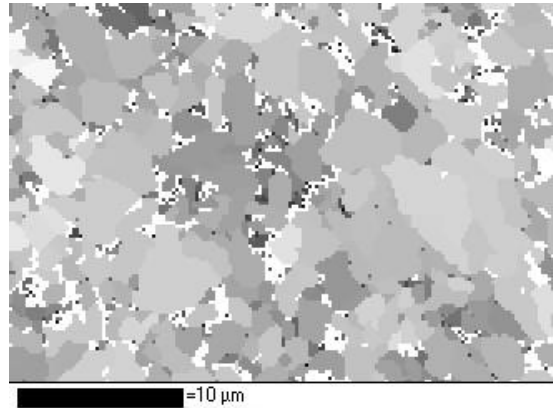


Figure A2.5: Mean band contrast map for the Mo steel.

The value of $BC_{critical}$ determined for the present EBSD map is indicated in **Figure A2.4** and corresponds reasonably well with the position of the shoulder in the distribution.

The objects having a mean band contrast greater than 85, which is the value of $BC_{critical}$ for the present EBSD map, are considered as ferrite grains. **Figure 5.12 (a)** is the final processed EBSD map where the coloured objects represent ferrite grains and white regions indicate the second phase.

The ferrite grain size distribution graph obtained from the processed EBSD map is shown in **Figure A2.6**. The region indicated by the rectangular box in the figure is due to noise (i.e. small misindexed areas) of the EBSD map. The grain size from EBSD maps can be

obtained by ignoring this noise and subsequently fitting a log-normal curve to the rest of the grain size distribution graph. As the noise occupies a significant fraction of the distribution, the frequency of grain sizes in the region without noise is underpredicted. This is adjusted in the following manner. First, a log-normal fit to the experimental grain size distribution is determined with similar width and ignoring the noise (**Figure A2.6**). Excluding the grain size region with noise the area under the experimental curve is A and the area under the fit curve is B. Then an adjusted experimental grain size distribution is constructed (**Figure A2.7**) with the frequency in each size class defined as $(B/A) \times$ frequency of the original experimental grain size distribution except for the smaller size classes affected by the noise. Subsequently, a log-normal fit to the adjusted experimental grain size distribution (as shown in **Figure A2.7**) is used to determine the ferrite grain size.

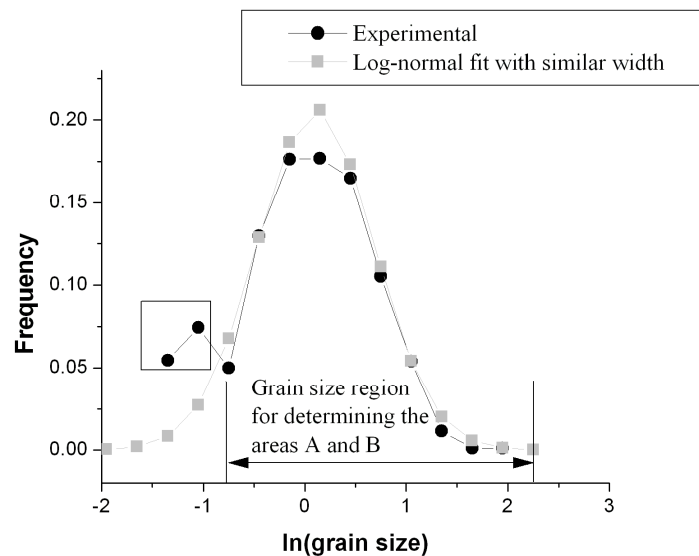


Figure A2.6: Grain size distribution obtained from the EBSD map for Mo steel (critical misorientation angle is 2° and BC_{critical} is 85) and as-fitted log-normal distribution with similar width and ignoring the noise.

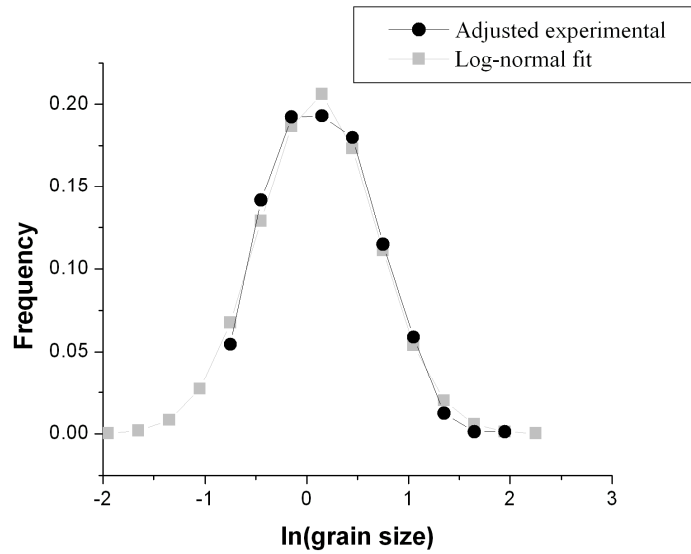


Figure A2.7: Adjusted grain size distribution and re-fitted log-normal distribution by ignoring the noise.

References:

1. B. Hutchinson, L. Ryde, E. Lindh, and K. Tagashira: *Materials Science and Engineering A*, 1998, vol. A257, pp. 9.
2. T. Waterschoot, L. Kestens, and B.C. De Cooman: *Metallurgical and Materials Transactions A*, 2002, vol. 33A, pp. 1091.
3. S. Zaefferer, J. Ohlert, and W. Bleck: *Acta Materialia*, 2004, vol. 52, pp. 2765.

Appendix 3

Estimation of ΔS

First of all the driving pressure at 968 K was calculated from THERMOCALC in terms of C_γ (wt% C in austenite) (**Figure A3.1**).

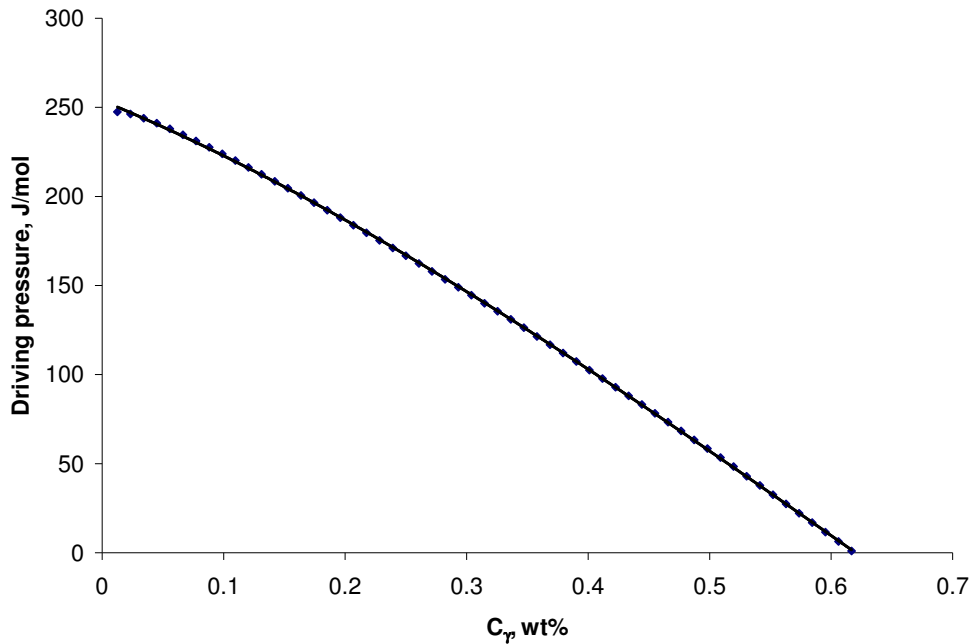


Figure A3.1: Driving pressure vs. C_γ for Mo steel at 968 K.

From **Figure A3.1**, the equation of driving pressure was obtained as a function of C_γ :

$$\Delta G = 149.58(C_\gamma)^3 - 299.62(C_\gamma)^2 - 280.93C_\gamma + 253.75 \quad (\text{A3.1})$$

Next, for the entire range of C_γ in **Figure A3.1**, ΔT_γ^* and ΔT_α^* were calculated in the following fashion:

$$\Delta T_\gamma^* = (T_\gamma^{eq} \text{ with } C_\gamma) - 968 = -135.22C_\gamma + 1052.0 - 968 \quad (\text{A3.2})$$

$$\begin{aligned} \Delta T_\alpha^* &= (T_\alpha^{eq} \text{ with } C_\alpha) - 968 = \left(T_\alpha^{eq} \text{ with } \left(C_\gamma \left(\frac{C_\alpha^{eq}}{C_\gamma^{eq}} \right)_{at T} \right) \right) - 968 \\ &= -10947.0C_\gamma \left(\frac{C_\alpha^{eq}}{C_\gamma^{eq}} \right)_{at T} + 1102.4 - 968 \end{aligned} \quad (\text{A3.3})$$

Then the undercooling was introduced such that

$$\Delta T^* = 0.5(\Delta T_\gamma^* + \Delta T_\alpha^*) \quad (\text{A3.4})$$

The driving pressures from **Figure A3.1** are replotted as a function of ΔT^* in **Figure A3.2**. In a first approximation a linear relationship of ΔG with ΔT^* is obtained. The slope of the linear fit of the data points in **Figure A3.2** which is made to pass through the origin gives the proportionality factor ΔS ($=0.318 \times 10^6 \text{ Jm}^{-3}\text{K}^{-1}$, at 968K).

In the present study the ferrite formation during the cooling path after DIFT is also considered. It is assumed that ferrite forms till a temperature of 873K (600°C). As a significant portion of the transformation occurs at 968 K (or very close to this temperature), for simplicity, the value of ΔS determined at 968 K is used in the cooling regime.

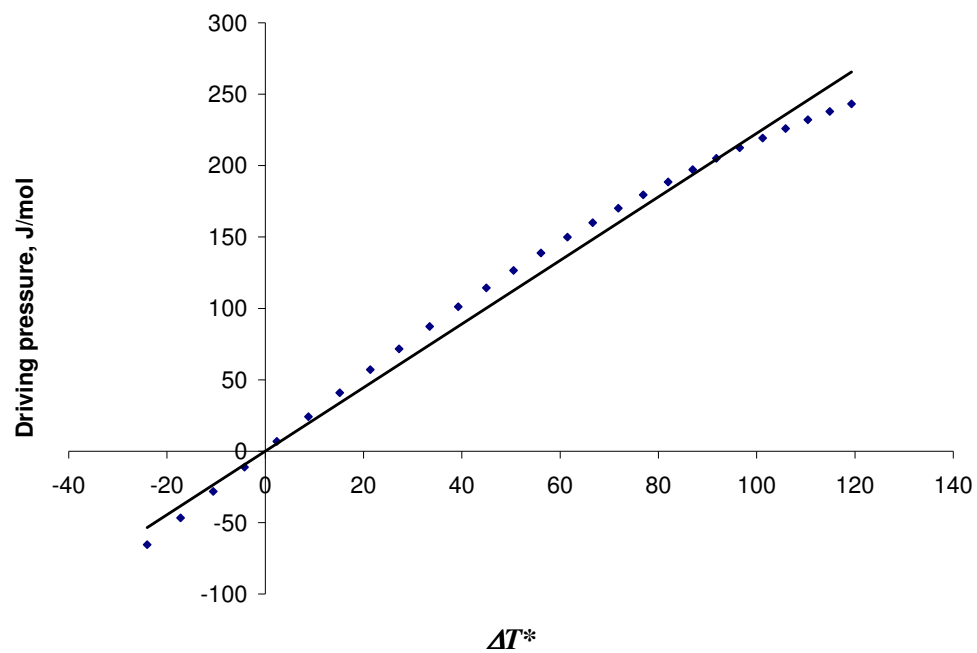


Figure A3.2: Driving pressure vs. ΔT^* .

Appendix 4

Convergence analysis: Node size, time stepping, and interface thickness

According to Rappaz [1] both phase field and solute diffusion equations are parabolic partial differential equations with source terms. He proposed finite difference schemes to solve these equations. From the theory of finite difference method solution of parabolic partial differential equations

$$\frac{\partial^2 u}{\partial x^2} = \frac{\partial u}{\partial t} \quad (\text{A4.1})$$

the convergence criterion implies a condition between node size and time stepping [2] that can be stated as

$$\frac{\Delta t}{(\Delta x)^2} \leq \frac{1}{2} \quad (\text{A4.2})$$

Rappaz modified this condition for both phase field equation and solute diffusion equation.

$$\frac{\Delta t}{(\Delta x)^2} + \frac{\Delta t}{(\Delta y)^2} < \frac{1}{2D_s} \quad (\text{A4.3})$$

where D_s is the solute diffusivity.

Considering Δx is equal to Δy ,

$$\frac{\Delta t}{(\Delta x)^2} < \frac{1}{4D_s} \quad (\text{A4.4})$$

and,

$$\frac{\Delta t}{(\Delta x)^2} + \frac{\Delta t}{(\Delta y)^2} < \frac{1}{2\mu\sigma_i} \quad (\text{A4.5})$$

where, μ and σ_i are respectively, mobility and interfacial energy.

Considering Δx is equal to Δy ,

$$\frac{\Delta t}{(\Delta x)^2} < \frac{1}{4\mu\sigma_i} \quad (\text{A4.6})$$

To satisfy these conditions in the present code the time stepping is made adaptive and taken to be the minimum of three quantities, i.e.

$$\Delta t = \min. \left(\frac{0.2 a^2}{\mu_{\gamma\alpha}\sigma_{\gamma\alpha}}, \frac{0.2 a^2}{D_\gamma^C}, \frac{0.2 a^2}{D_\alpha^C} \right) \quad (\text{A4.7})$$

where, a is the node size.

As $D_\gamma^C \ll D_\alpha^C$, the second term is ignored and the time stepping is the minimum of the remaining two terms.

The convergence criterion was verified with nominal nucleation. The ferrite transformation kinetics was studied, for isothermal holding at 968 K, for two node sizes: 0.0125 μm and 0.00625 μm . The results of the calculations are shown in **Figure A4.1**. Another set of convergence test was done for a cooling rate of $\sim -70^\circ\text{C/s}$ from 695 to 600 $^\circ\text{C}$, because this zone also falls in the ferrite formation region. The result for this calculation is shown in **Figure A4.2**. From **Figures A4.1** and **A4.2**, it is concluded that

the node size of $0.0125\ \mu\text{m}$ can be used in conjunction with the adaptive time stepping described before.

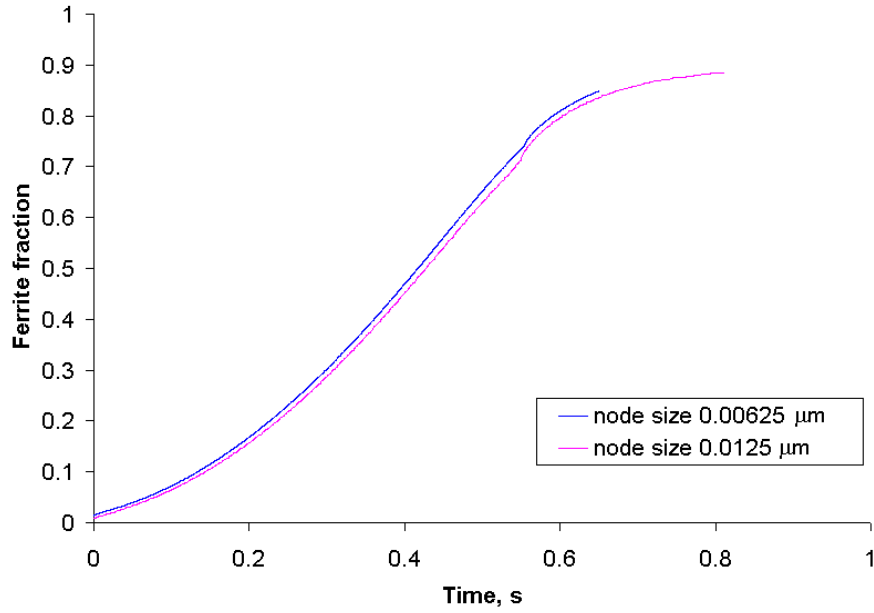


Figure A4.1: Ferrite transformation kinetics for two node sizes at 968K (nominal nucleation).

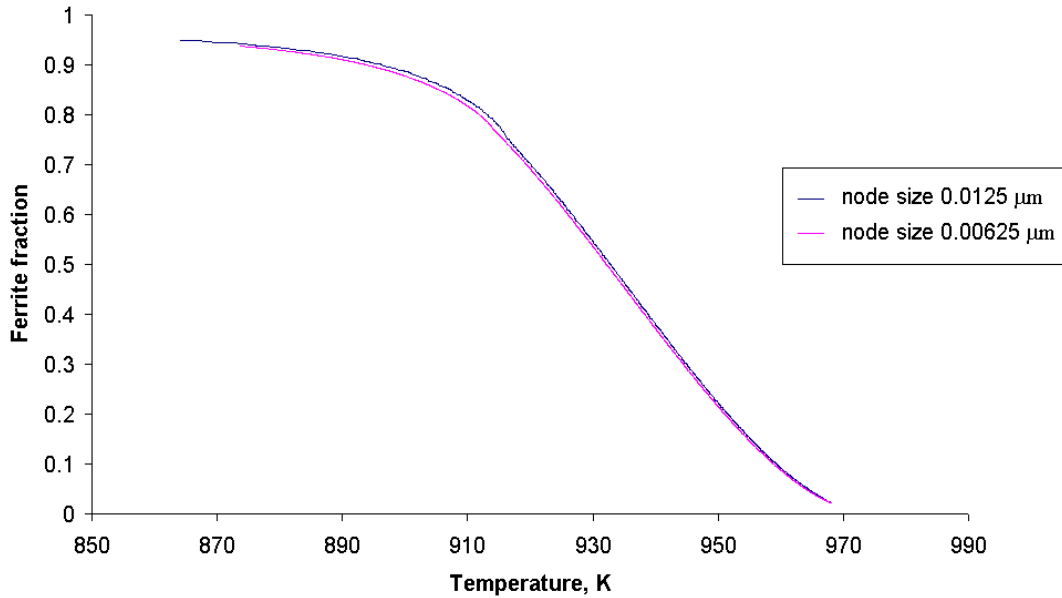


Figure A4.2: Ferrite transformation kinetics for two node sizes at cooling path from 968 K to 873 K (nominal nucleation).

Another set of simulations was done to test the convergence for time stepping. Nominal nucleation with a node size of 0.0125 μm was used for this purpose. For one simulation the time step was taken as the adaptive time step (**Equation A4.7**). The other simulation was done with a time stepping, which is half of the time stepping as determined from **Equation A4.7**. Romig et al. considers it is better to keep Δt at about 1/10 of the limit set by the stability criterion [3]. A simulation was also done applying Romig's consideration. The results of the simulations are shown in **Figure A4.3**. These simulations include isothermal holding at 968K for 0.74 s and cooling at a rate of 70°C/s to 873K. From **Figure A4.3** it can be concluded that by using **Equation A4.7** convergence has been obtained in terms of time stepping.

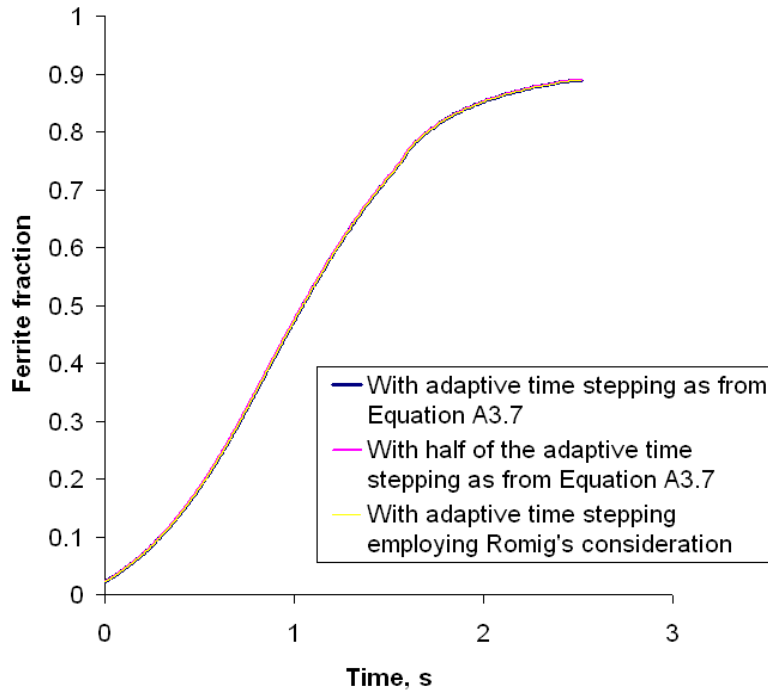


Figure A4.3: Ferrite transformation kinetics for three time steppings (nominal nucleation).

Another set of simulations was done to evaluate the convergence for the interface thickness. Nominal nucleation with a node size of $0.0125\ \mu\text{m}$ was used for this purpose. For one simulation the interface thickness was $0.1\ \mu\text{m}$ (i.e. eight nodes in the interface which was used for all other simulations). Another simulation was done with an interface thickness of $0.2\ \mu\text{m}$ (i.e. 16 nodes in the interface). The results of the simulations are shown in **Figure A4.4**. These simulations include isothermal holding at 968K for 0.74 s and cooling at a rate of 70°C/s to 873K. From **Figure A4.4** it can be concluded that by using an interface thickness of $0.1\ \mu\text{m}$ convergence has been obtained in terms of interface thickness.

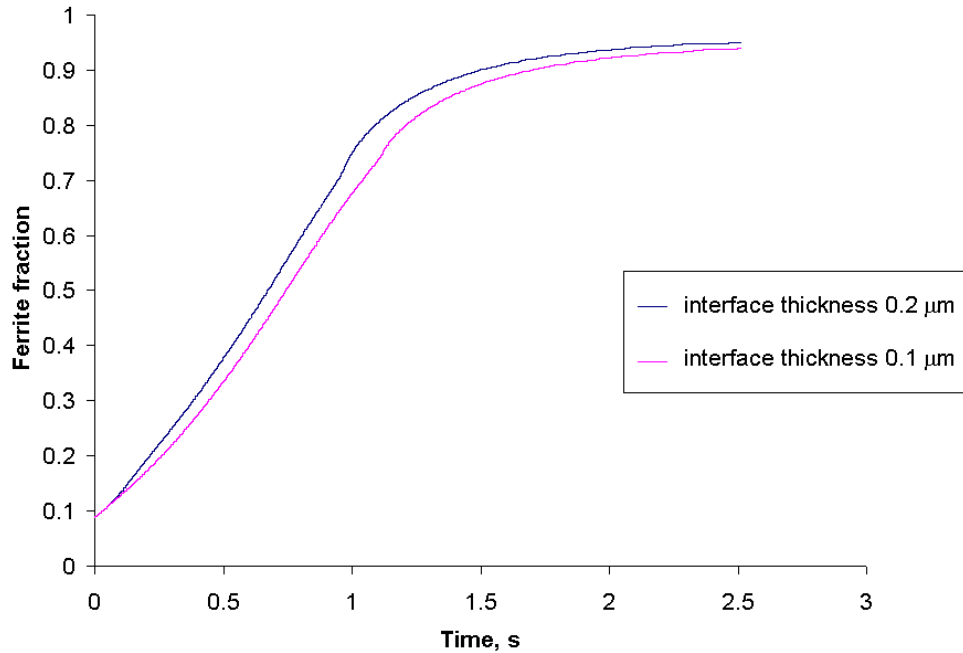


Figure A4.4: Ferrite transformation kinetics for two interfacial thickness (nominal nucleation).

References:

1. Phase field formalism, Doctoral School Course by M. Rappaz, LSMX-IMX, Ecole Polytechnique, June 2004.
2. D.V. von Rosenberg, *Methods for the Numerical Solution of Partial Differential Equations*, American Elsevier, New York, 1969, pp. 19.
3. A.D. Romig, Jr., N.Y. Pehlivanurk, and O.T. Inal, *Diffusion Analysis and Applications*, A.D. Romig, Jr., and M.A. Dayananda eds., The Minerals, Metals and Materials Society, Warrendale, PA, 1989, pp. 45.